Adapting driver behaviour for lower emissions

MODALES D3.2: Correlation of user behaviour variability with emissions

WORK PACKAGE	**WP3: Impact of user behaviours**
TASK 3.5	Correlation of user behaviour variability with emissions
AUTHORS	Haibo Chen; Jianbing Gao; Ye Liu; Zhiyuan Lin – UNIVERSITY OF LEEDS Ying Li – DYNNOTEQ Juhani Laurikko – VTT Matteo Federici; Guido Perricone – BREMBO Valerio Bortolotto; Mauro Patelli – BRIDGESTONE
DISSEMINATION LEVEL	Public (PU)
STATUS	Final, approved by the European Commission
DUE DATE	31/08/2021
DOCUMENT DATE	31/08/2021
VERSION NUMBER	1.0

This project has received funding from the European Union's Horizon 2020 research and innovation programme under grant agreement No 815189.

Quality control

	Name	Organisation	Date
Editor:	Haibo Chen	LEEDS	31/08/2021
Peer review 1:	Matteo Federici	BREMBO	27/08/2021
Peer review 2:	Andrew Winder	ERTICO	27/08/2021
Authorised by (Technical Coordinator):	Juhani Laurikko	VTT	31/08/2021
Authorised by (Project Coordinator):	Jean-Charles Pandazis	ERTICO	31/08/2021
Submitted by:	Andrew Winder	ERTICO	31/08/2021

Revision and history chart

Version	Date	Main author	Summary of changes
0.1	12/06/2021	Haibo Chen	Table of contents and responsibilities
0.2	15/07/2021	Jianbing Gao; Haibo Chen	Modelling of powertrain emissions
0.3	16/07/2021	Ye Liu; Haibo Chen;	Modelling of brake and tyre wear
0.4	19/07/2021	Jianbing Gao; Haibo Chen;	Model validation with PEMS data
0.5	02/08/2021	Ye Liu; Haibo Chen; Ying Li	Model validation with brake wear data
0.6	09/08/2021	Ye Liu; Haibo Chen; Ying Li	Model validation with tyre wear data
0.7	24/08/2021	Ying Li	In-task review comments and corrections
0.8	25/08/2021	Haibo Chen	Consolidated draft for peer-reviews
0.9	30/08/2021	Haibo Chen	Peer review comments addressed. Submitted to Quality Manager, project and technical coordinators for authorisation
1.0	31/08/2021	Andrew Winder, Juhani Laurikko, Jean-Charles Pandazis	Final check and submission

Legal disclaimer

Table of Contents

Index of figures

Index of tables

Glossary of terms

Term	Description
ABAQUS	ABAQUS is a software suite for finite element analysis and computer-aided engineering, originally released in 1978.
GT-suite	GT-SUITE is the industry-leading simulation tool with capabilities and libraries aimed at a wide variety of applications and industries, in particular automotive engineering, vehicle design and simulation.
MODALES	This EU Horizon 2020 project: "Modify Drivers' behaviour to Adapt for Lower Emissions" (2019-2022, http://modales-project.eu)
NAEI	The NAEI estimates annual pollutant emissions from 1970 to the most current publication year for the majority of pollutants. The data were collected and analysed from a wide range of sources – from national energy statistics through to data collected from individual industrial plants.

List of abbreviations and acronyms

Abbreviation/acronyms	Meaning
ALE	Arbitrary Lagrangian Eulerian
ASP	Average speed policy: an average speed of surrounding traffic is used as the desired speed
BSFC	Brake-specific fuel consumption
BWP	Brake wear particle
CPC	Condensation particle counter
CSP	Constant speed policy: a constant speed without considering surrounding traffic is used as the desired speed
DI	Direct injection
DOC	Diesel oxidation catalyst
DP	Dynamic programming: an algorithmic technique for solving an optimization problem by breaking it down into simpler subproblems and utilizing the fact that the optimal solution to the overall problem depends upon the optimal solution to its subproblems.
DPF	Diesel particulate filter
DSG	Direct shift gearbox
EFM	Exhaust flow meter
EGR	Exhaust gas recirculation
ELPI	Electric low-pressure impactor
EPA	Environmental Protection Agency
EUDC	Extra urban driving cycle
FEA	Finite element analysis
FTP-75	Federal test procedure
GPF	Gasoline particulate filter

Abbreviation/acronyms	Meaning
GPS	Global position system
HDV	Heavy duty vehicle
ICE	Internal combustion engine
InCo	International Cooperation
KPI	Key performance indictor
LACT	Los Angeles City Traffic
LDV	Light duty vehicle
mg	milli g-force, i.e. 1/1000 of 9.807 m/s^2
MOOP	Multi-objective optimisation problem: an optimisation problem where several objectives are included.
MPC	Model predictive control: an advanced method of process control that is used to control a process while satisfying a set of constraints.
NEDC	New European driving cycle
NOx	Nitrogen oxide
OBD	On-board diagnostics
PEMS	Portable emission measurement system
PM	Particulate Matter
PM1	Particulate Matter 1 Micrometre or Less in Diameter
PM10	Particulate Matter 10 Micrometres or Less in Diameter
PM2.5	Particulate Matter 2.5 Micrometres or Less in Diameter
PN	Particle Number
PN1	Particle Number 1 Micrometre or Less in Diameter
PN10	Particle Number 10 Micrometres or Less in Diameter
PN2.5	Particle Number 2.5 Micrometres or Less in Diameter
PSD	Particle size distribution
PSP	Predicted speed policy: a predicted speed of surrounding traffic is used as the desired speed
RDE	Real-world driving emission
SCR	Selective catalytic reduction
SEMS	Smart emissions measurement system
TWC	Three-way-catalyst
US06	Supplemental federal test procedure
UV	Ultraviolet
WLTC	Worldwide harmonized light vehicles test cycle
WLTP	Worldwide harmonised light vehicle test procedure
WLTP-brake	Worldwide Harmonized Light-duty Vehicles Test Procedure for brake
WP	Work Package
XGBoost	eXtreme Gradient Boosting

List of mathematical symbols

Symbols	Meaning
a	Vehicle acceleration
A_f	Vehicle front area
$a_{NOx20\%}$	Vehicle acceleration corresponding to 20% of the total NO_x emissions
$a_{NOx50\%}$	Vehicle acceleration corresponding to 50% of the total NO_x emissions
$a_{PN20\%}$	Vehicle acceleration corresponding to 20% of the total PN emissions
$a_{PN50\%}$	Vehicle acceleration corresponding to 50% of the total PN emissions
c_1 , c_2	Rolling parameters
C_d	Aerodynamic drag coefficient
C_h	Altitude
C_r	Rolling resistance factor
E_b	Braking energy
E_e	Engine energy
E_k	kinetic energy
g	Gravity acceleration
$G(t)$	Slope
L	The contact length between tyre and ground
M_e	Effective mass of vehicle (including inertia)
M_v	Vehicle mass
$NO_{x20\%}$	NO_x emission rates corresponding to 20% of the total NO_x emissions
$NO_{x50\%}$	NO_x emission rates corresponding to 50% of the total NO_x emissions
$P(t)$	Energy consumption
$PN_{20\%}$	PN emission rates corresponding to 20% of the total PN emissions
$PN_{50\%}$	PN emission rates corresponding to 50% of the total PN emissions
R_w	Tyre radius
T_e^{max}	Maximum engine torque
T_e^{min}	Minimum engine torque
v_d	Desired speed
V_{max}	Maximum vehicle speed
V_{min}	Minimum vehicle speed
$v_{NOx20\%}$	Vehicle speed corresponding to 20% of the total NO_x emissions
$v_{NOx50\%}$	Vehicle speed corresponding to 50% of the total NO_x emissions
$v_{PN20\%}$	Vehicle speed corresponding to 20% of the total PN emissions
$v_{PN50\%}$	Vehicle speed corresponding to 50% of the total PN emissions
γ_g	Gear ratio
η	Transmission efficiency

Symbols	Meaning
η_d	Driveline efficiency
θ	Road grade
λ	Rotl masses
ρ	Air density

Executive Summary

This report represents the work carried out in Task 3.5 of the MODALES project, aimed at quantifying the relationship between the user's driving behaviour and the resultant vehicle emissions from three sources (i.e. powertrain, brake, and tyre), respectively and in combination. A set of advanced mathematical and statistical models were developed to produce accurate estimates of vehicle emissions from all the three sources as a function of driving behaviour indicators which will be monitored and calculated during the user trails in eight European cities as well as the City of Nanjing (China), later in the project. Any behavioural change – as a result of training and education for low-emission driving – will be analysed and used to assess if it leads to a reduction in vehicle emissions.

The specifications of these models were derived from the state-of-the-art knowledge of low-emission factors gathered together in WP2, including recommendations and guidelines for the collection of new real driving data (both exhaust and non-exhaust) and low-emission driving requirements, as reported in MODALES D2.1. The model specifications were then finalised in line with performance criteria and indicators set up in WP6 for user trials and evaluation. In addition, these models were defined to ensure that the correlation between driving behaviour and vehicle emissions can be interpolated or extrapolated when scaling up the impact of the MODALES innovation solutions in WP6.

These models were calibrated and validated in two steps. Firstly, the results generated by these models were compared to published scientific studies to ensure that the most advanced modelling theory is taken into consideration and adopted (or improved whereas appropriate) to meet the project's objectives. Secondly, the emission measurements and corresponding driving behaviours, collected in Tasks 3.1 (powertrain emission), 3.2 (brake wear) and 3.3 (tyre wear), provide limited but valuable reference data for the models to be further calibrated and validated. This increases confidence in the models' outputs. These modelling developments are summarised as follows.

Based on the preliminary data analysis as reported in D3.1, the collected emission measurements were further analysed to determine if the real-world or in-lab data can be used to derive mathematical models. It is concluded that:

- The PEMS (Portable emission measurement system) exhaust data is accurate and adequate (second by second) for instantaneous emission modelling, with a high level of agreement with the prediction of the models.
- Brake wear measurements collected in-lab are also accurate and reliable, and can be used to directly validate the results of the mathematical models as both have the same output frequency.
- Real-world wear measurements of the **left tyres** (i.e. on the left side of the vehicle) were collected every three months or so. As the actual corresponding driving behaviour data (e.g. acceleration, speed) can not be made available for analysis due to data privacy and business interest, the behaviour data are classified into bins/categories. Analysis shows that tyre wear measurements exhibit a high degree of asymmetry with outliers far away from the average value. Simple linear regression models fail to correlate average categorical accelerations (both longitudinal and lateral) and vehicle speed to tyre wear. More advanced non-linear models (e.g. the XGBoost non-linear fitting method), seem to be able to improve the correlation considerably, with a R square value of 0.846 (compared to 0.102 for the best simply linear

regression model), due to their capability of capturing the skewness and peaked-ness of the tyre wear measurements.

To overcome the limitations on vehicle types, driver behaviours and many other factors such as road and traffic conditions in the measurement campaigns, a set of simulation tools and models were developed and are summarised as follows:

- A GT-suite vehicle model was developed to simulate exhaust emissions. This "physical" model consists of engine performance map, gear number, gear ratio, and other vehicle parameters such as body dimensions and shape. The model is also able to take into account the effect road parameters, environment conditions on vehicle emissions and energy consumption. The results show that the vehicle model produces highly accurate emission estimations, and able to be used to simulate various driving behaviours and speed profiles. This enables the development of the mathematical model for exhaust emissions to be implemented in the MODALES user trails.
- A Finite Element Analysis model was developed to simulate the brake wear resulting from the contact behaviour on a microscope size scale. Calibrated and validated by the dyno bench tests carried out by project partner Brembo, this "physical" model is able to produce brake wear for various brakes and under various driving conditions. The simulated results are then used to quantify the importance of Key Performance Indicators (KPIs) related to driving behaviour.
- Similarly, a "physical" model was also developed for the simulation of the wear on the **left tyres**. The model is built in ABAQUS which provides a rich library of tyre and road surface parameters. This model is particularly useful given that real-world tyre wear is measured over a long interval (e.g. > 3 months) and the corresponding driving behaviour data is not available.

Good driving guidelines and recommendations need to consider several criteria such as driver's safety and comfort, fuel consumption as well as now low vehicle emissions from multiple sources. These criteria often lead to different driving behaviours. How to incorporate these multiple objectives into the global optimal speed profile is an important research challenge. While this topic is out of the project's scope, preliminary work in considering multiple objectives to simultaneously optimise several factors was investigated, which shows promising results. The speed profile generated from a new multi-objective model is similar to the original fuel-only model under the free traffic condition but becomes significantly different under the heavy traffic condition.

Finally, the modelling work completed by drawing a conclusion on the importance of behaviour-related KPIs, as summarised as follows:

The top five important KPIs for ***powertrain*** emissions are:

1. The proportions of acceleration > 0.9 m/s^2 duration in the total travel time;
2. Average acceleration in the journey;
3. The proportions of speed interval of 20~50 km/h in the total travel time;
4. Average driving speed in the journey;
5. Average driving speed in the journey without the stop events.

The top five important KPIs for ***brake wear*** emissions are:

1. Deceleration rate of braking;
2. Average deceleration rate when braking;
3. Braking distance;

4. Braking time;
5. Initial speed when braking.

The top five important KPIs for ***tyre wear*** emissions are:

1. Deceleration rate when braking on curves;
2. Acceleration rate when accelerating on curves;
3. Initial speed when braking on curves;
4. Initial speed when accelerating on curves;
5. Deceleration rate when braking on straight roads.

Please note that the results reported later in this deliverable were based on the **left tyres** which take on more force than the right counterparts when the vehicle goes around right curves, especially sweeping turns. Likewise, the **right** tyres wear more than the left counterparts do when the vehicle goes around left curves. Generally speaking, tyre wear is higher when driving on curves. So, it is important to ***reduce the vehicle speed to an appropriate level before entering a curve*** as lowering the speed when the vehicle is already on a curve may cause the car to skid.

Quantitative results of the rankings can be found in Chapter 7, together with driving tips derived for the user trails in WP6.

1 Introduction

1.1 Background to MODALES

MODALES aims to substantially reduce air pollution from all types of on-road fleets by developing and testing a set of innovative solutions covering (*a*) promotion of ***low-emission driving behaviour and proper maintenance choice***, (*b*) improvement of the effectiveness of ***on-board diagnostics (OBD) devices and technical inspections*** to detect tampering, (*c*) adoption of ***retrofits*** for all vehicles to reduce exhaust emissions, and (*d*) creation of a lasting ***dissemination and awareness*** networking platform to bring more momentum to international cooperation in reduction of transport impact on air quality within the project's lifetime and beyond.

To fulfil this ambition, MODALES pursues a user-centric approach to advancing the fundamental understanding of the co-variability of user behaviour and vehicular emissions characterised by powertrain, brakes and tyres, modifying user behaviour via dedicated training and awareness campaigns, and generating guidelines and recommendations, based on scientific evidence, to support effective air quality plans and enforcement strategies to be developed by local and national authorities. The main activities of the MODALES project can be summarised as follows:

- Simultaneously ***measure real-world vehicle exhaust emissions*** and ***driving behaviours*** to produce accurate correlation between them using most advanced mathematical and statistical techniques;
- Explore ***most advanced technologies for retrofits*** designed to substantially reduce the powertrain emission from all types of vehicles including cars and other LDVs, HDVs and NRMM, and validate their effectiveness under different real-world traffic and environment conditions, and by various drivers;
- Carry out an ***in-depth analysis of OBDs, periodic inspection and legal issues on tampering in Europe*** (in particular in the member states where the legal situation of tampering is significant) to help regulatory authorities put in place effective anti-tampering legislation, and owners property maintain their vehicles;
- Conduct ***low-emission user trials*** (with both driving and maintenance practices) for several months in eight European cities plus the City of Nanjing in China, supported by concurrent ***large-scale awareness campaigns***, to enhance public engagement and help drivers better understand the impact of their driving and maintenance behaviours in all situations.

1.2 Purpose of this document

This deliverable is the second report of Work Package 3 (WP3), whose main goal is to assess the impact of user behaviour and driving style on various emissions. The work in WP3 uses the knowledge of low-emission factors identified and reviewed in WP2 to plan and conduct both on-road and in-lab experiments and tests of vehicle emissions from powertrain, brakes and tyres. These measurement campaigns are reported in detail in D3.1.

The emissions data collected are then used to create mathematical and statistical models which provide quantitative and qualitative estimations of vehicle emissions for the development of the low-emission driving (style) definition and various guidelines that will form the subject matter of the driver education activities in WP6, and the awareness campaigns in WP7. ***This deliverable describes the work on "correlation of user behaviour variability with emissions" carried out in Task 3.5***.

1.3 Scope and intended audience

The figure below shows how this deliverable fits in the project and highlights related deliverables which will take into account the content of this one.

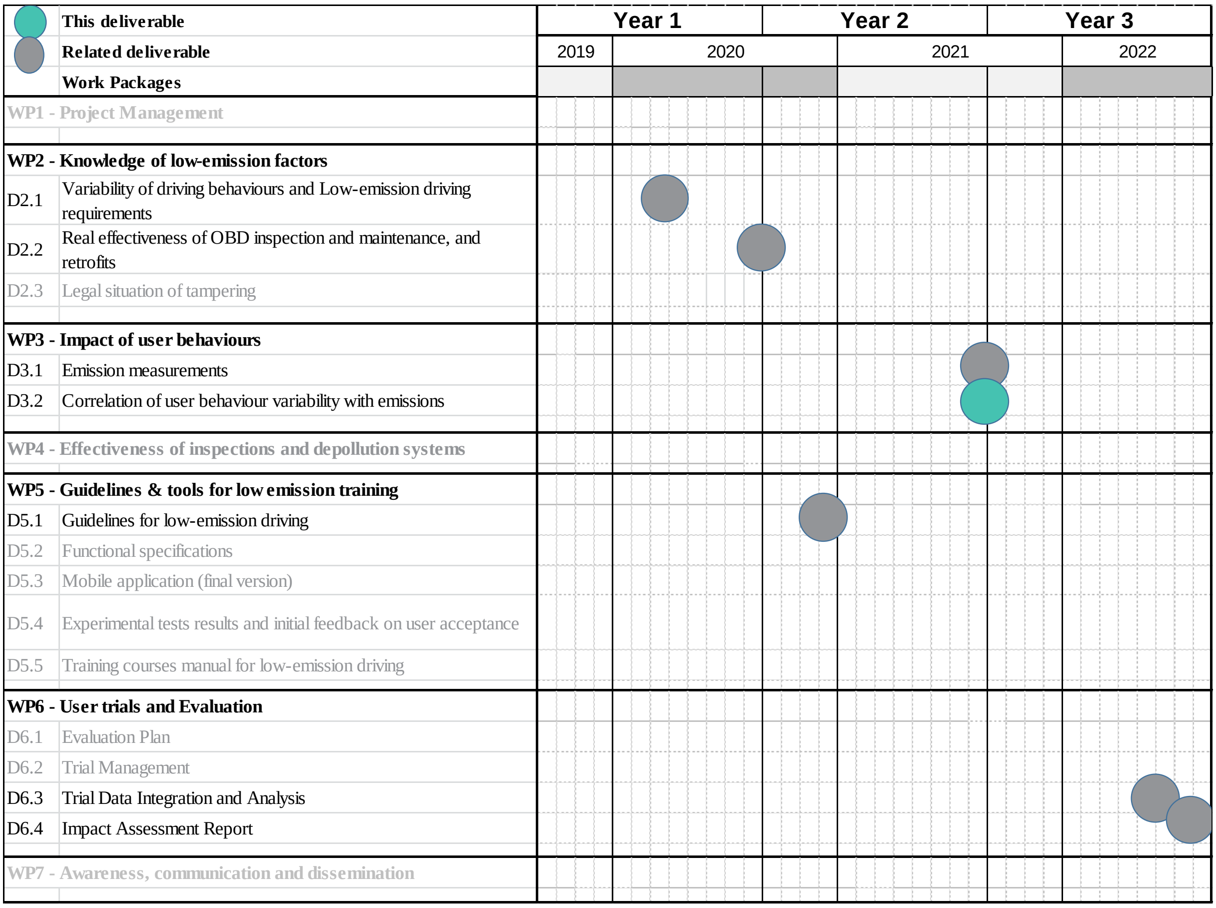

Figure 1.1: D3.2 Correlation of user behaviour variability with emissions, in the context of related MODALES deliverables

The Correlation Analysis concerns all the subsequent Work Packages in MODALES, especially WP6, because it provides an assessment tool for the technological and training solutions developed by all the project beneficiaries to be technically evaluated.

As a public deliverable, D3.2 is also of potential interest to an external audience concerned with both exhaust and non-exhaust emissions from all types of vehicles powered by not only internal combustion engines (ICE) but also batteries or alternative fuels.

1.4 Document structure

All the activities specified in Task 3.5 have been carried out and their objectives have been fulfilled. There are no deviations regarding the content or the timing.

This deliverable is structured as follows.

Chapter 2 describes further analysis of emission measurements collected in the earlier tasks of WP2, following up the preliminary data analysis reported in D3.1.

Chapter 3 reports the findings of the simulation and modelling of powertrain emissions driven by driving behaviours.

Chapter 4 is concerned with the modelling work on a brake wear emission model based on the Finite Element Analysis method.

Chapter 5 presents the results from a FEA-based physical model for tyre wear model.

Chapter 6 describes some preliminary developments of multi-objective optimisation methods, such as monetary values, dynamic programming etc.

Chapter 7 brings together all the modelling work carried out in Task 3.5 to rank the importance of behaviour-related KPIs to facilitate the development of low-emission driving training.

Chapter 8 concludes what lessons have been gained in MODALES in terms of correlation analysis of driving behaviour and vehicle emissions from powertrain, brakes and tyres.

2 Further analysis of emissions from powertrain, brake and tyre wear

2.1 Real-world emissions from powertrain

In this section, the second-by second real-world test emissions including NOx and PN emissions of different types of passenger cars are further analysed; additionally, the significant contribution regions of the NOx and PN emissions from powertrain are discussed.

Real-world driving emission (RDE) test procedures were introduced into Euro-6 emission standards to limit real-world emissions (Giechaskiel et al., 2019; Hooftman et al., 2018). Real-world emission factors are much higher than the ones over standard driving cycles, especially for NO_x and particle emissions. Euro-6 emission standard limits both PM and PN emissions from DI petrol cars (Weber et al., 2019; Yinhui et al., 2016). In order to meet the strict emission standard on particles, gasoline particulate filters (GPFs) are usually applied to DI petrol cars (Awad et al., 2020; Jang et al., 2018; McCaffery et al., 2020; Yang et al., 2018) to drop particle emissions; GPFs present excellent performance of PM and PN emission reductions, especially for solid phase particles (Baek et al., 2020; Chan et al., 2016; Jang et al., 2018). Due to the different driving behaviour over various driving cycles, the efficiency changed significantly with driving cycles (Jang et al., 2018). The filter efficiency of GPFs is approximately 86.2%, 96.1%, and 77.3% for the driving cycles of Federal Test Procedure (FTP-75), WLTC, and Supplemental Federal Test Procedure (US06) respectively. Regarding diesel passenger cars, diesel particulate filters (DPFs) are the most successful technique controlling PM and PN emissions, they are widely used, and their performances over various driving cycles have been researched (Bermúdez et al., 2014; Hays et al., 2017; Hoepfner and Roduner, 2013; Li et al., 2013). The filter efficiency of DPF was in the range of 82~95% over the driving cycle of WLTC, NEDC, and extra urban driving cycle (EUDC).

NO_x emission rates of diesel passenger cars over real-world driving were much higher than those from WLTC and NEDC conditions (Triantafyllopoulos et al., 2019), especially under cold start conditions (Gao et al., 2019b; Gao et al., 2019c). The NO_x emissions over real-world driving were approximately twice of the values over WLTC, and almost 10 times of NEDC (Triantafyllopoulos et al., 2019). It also addressed the importance of the real-world emission monitor and indicated the NO_x contributions from cold start stages; additionally, the variations of real-world NO_x emissions were significant for petrol passenger cars (Valverde et al., 2019). Cha et al. (Cha et al., 2019) showed that NO_x emission factors over real-world driving conditions were approximately seven times of the emission limits based on 17 Euro-6 compliant passenger cars. O'Driscoll et al. (O'Driscoll et al., 2018) compared NO_x emissions from diesel and petrol passenger cars under real-world driving conditions, showing that NO_x emission factors of diesel cars were much higher than petrol cars, especially on motorways, mainly due to more NO_x formations and lower efficiency of the NO_x reduction system.

In summary, there are many real-world tests being conducted for passenger cars, and the real-world emissions have been compared over various driving cycles in labs. However, the real-world emission comparisons, e.g. NO_x and PN from DI petrol cars and diesel cars which meet Euro-6 emission standards over the same routes and same driver are still under-studied. Previous published results include the impacts from driving habits which present significant effects on emissions (Böttcher and Müller, 2015; Hasan et al., 2019). In this chapter, two DI petrol cars and a diesel car are tested under real-world driving conditions. A portable emission measurement system (PEMS) is used to monitor instantaneous NO_x and PN emissions from the exhaust gases. The comparisons of the emissions from these three passenger cars are made; meantime, the distributions of the average emission rates over speed and acceleration are analysed. This research provides the foundations for reducing real-world emissions from passenger cars.

2.1.1 Descriptions of the test vehicles and procedure

The specifications of the three passenger cars are given in Table 2.1. The cars are named to indicate their fuel type and after-treatment technology, with P for petrol, D for diesel and N-GPF for no GPF. There are two petrol cars and a diesel car; they meet Euro-6 emission standards. For the two petrol cars, three-way-catalysts (TWCs) are used to control the gaseous emissions; one of them is equipped with a GPF to control the particle emissions. Regarding the diesel passenger car, a diesel oxidation catalyst (DOC), a DPF and a SCR are used to control both gaseous and particle emissions. All the passenger cars are turbocharged and direct fuel injection, and P-GPF (i.e. petrol fuel and GPF after-treatment) is equipped with the smallest engine size. Because of the direct injection applications, particle formations of petrol cars are increased significantly, resulting from the rich air/fuel zones due to short fuel diffusion process. It should be noted that the compression ratio of P-N-GPF is much higher than the other petrol passenger car. Generally, high compression ratio will lead to high in-cylinder combustion temperature, with the results of more and finer particles; additionally, P-N-GPF is free of a particle filter which may result in high PN emissions.

Table 2.1: Vehicle specifications of the test vehicles

Car label		P-GPF	P-N-GPF	D-DPF
Car maker		Opel	Skoda	Skoda
Model		Crossland-X	Octavia	Octavia
Manufacture year		2019	2017	2019
Fuel type		Petrol	Petrol	Diesel
Fuel delivery		Direct injection	Direct injection	Direct injection
Aspiration		Turbocharged	Turbocharged	Turbocharged
Engine size/ L		1.12	1.5	1.6
Max. power @ speed/ kW @RPM		81@5500	110@5000	85@3250-4000
Max. torque @ speed/ Nm @RPM		125@1500	250@1500-3000	250@1500-3000
Compression ratio		10.5	12.5	16.2
Running mass/ kg		1278	1470	1556
After-treatment	Gaseous	TWC	TWC	DOC+SCR
	Particles	GPF	--	DPF
Emission standards		Euro-6d_temp	Euro-6c	Euro-6d_temp
Gear number (type)		6 (A)	6 (M)	7 (DSG)
Type approval cycle		WLTP	NEDC	WLTP
Type approval NO_x (mg/km)		17.5	34.1	29.2
Type approval PN ($\#*10^{11}$)		4.2	1.08	0.02
Type approval CO_2 (g/km)		153	115	141
Mileage/ km		34261	73494	31204

NO_x and particle emission factors are significantly affected by cold start events in the journey

(Merkisz et al., 2019); such that the cold start events will affect the analysis of the relationships between emission factors and driving behaviours (Gao et al., 2021). Real-world NO_x and PN exhaust emissions of the three passenger cars were monitored using a state-of-the-art gas PEMS and a particle PEMS. This system included a gas module and a particle module which accurately measured the concentration of NO_x and PN emissions from both petrol and diesel cars. An ultraviolet (UV) analyser was used to measure NO_x concentration. Total particles included solid phase and liquid phase particles, and only the particles being larger than 23 nm were counted by the PEMS system. In order to avoid the effect from high-volatility substances and water vapours, the thermal denuder was heated to 300ºC. PEMS was installed at the back of the cars and an extension to the exhaust tailpipe was used to mount an exhaust flow meter (EFM) tube along with a temperature sensor used to monitor the exhaust flow rates and temperature, as well as a sampling probe at the very end.

Figure 2.1 (from MODALES D3.1) shows the real-world driving routes and test cars. The PEMS was calibrated before the test, and the cars were fully warmed up (coolant temperature being approximately 70 ºC) before the test run to avoid the cold impacts. AVL Concerto M.O.V.E post processing program was used to record the sampling data, including gaseous pollutants and PN. Longitude, latitude, and altitude were also recorded by a GPS system. All second-by second data were saved into a laptop. In this chapter, the analysis is only focused on NO_x and PN emissions which are the main concerns of modern passenger cars.

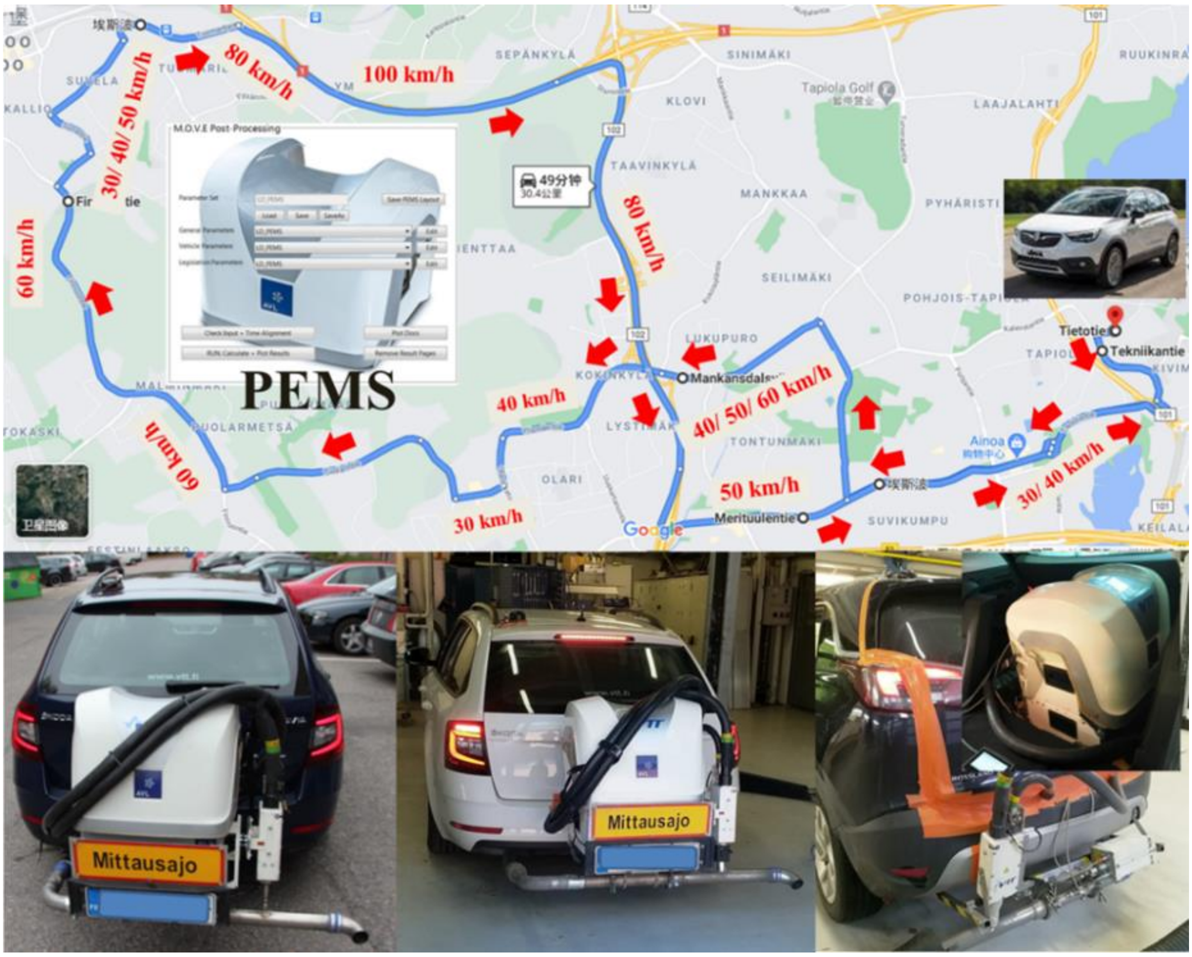

Figure 2.1: Real-world driving route near Helsinki and test cars

The three vehicles were driven by the same driver on the same routes. The route started from the VTT research centre (Espoo, in the Helsinki metropolitan area, Finland), including rural roads, urban roads, and motorways. The percentages of the urban roads, rural roads, and motorways in the total distance were around 76.8%, 16.5%, and 6.7% respectively; the speed limits of the road were marked in the map as well. The altitude along the driving distance during the journey is shown in Figure 2.2. As can be seen, the changes of the altitude over the routes were gentle.

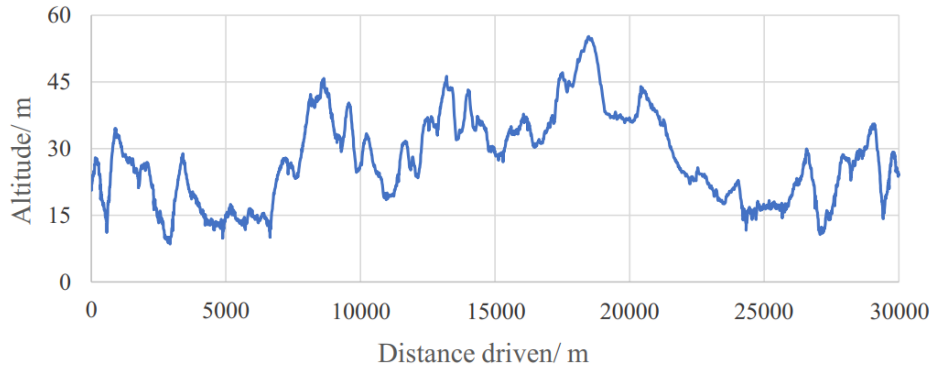

Figure 2.2: Altitude along the driving distance

2.1.2 Real-world instantaneous NOx and PN emissions

In this section, the test results are presented and the comparisons of the real-world driving emissions among the three cars are conducted; in the meantime, the relationships between powertrain emission rates (e.g. NO_x and PN) and driving behaviours (e.g. speed and acceleration) are analysed.

2.1.2.1 Emissions under real-world driving conditions

Real-world driving parameters of P-GPF including speed, acceleration, and exhaust temperature are shown in Figure 2.3. The videos during the real-world driving were also recorded to check the driving situations for data analysis.

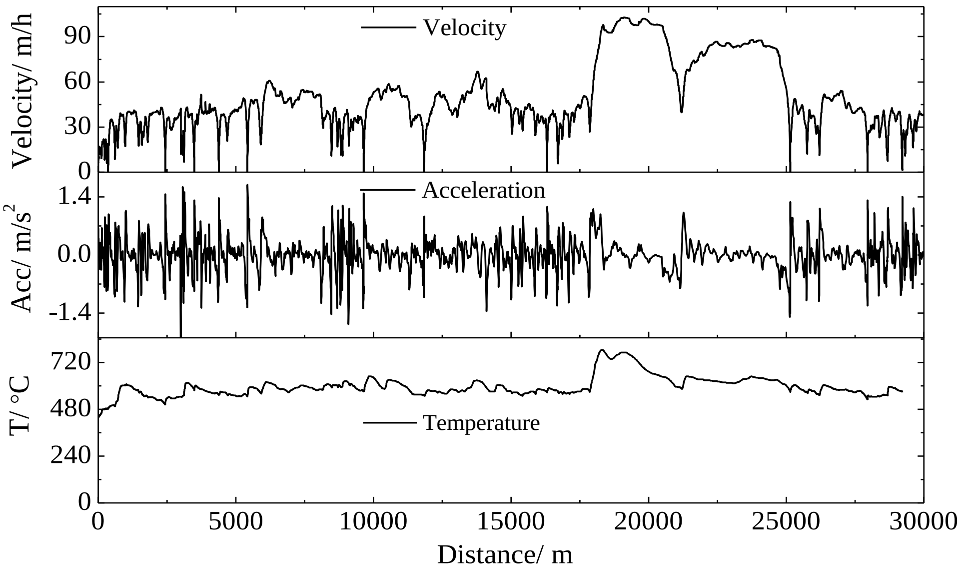

Figure 2.3: P-GPF real-world driving parameters

At the first half period of the journey, the speed was lower than 60 km/h during most of the driving time. There were several sections where the speed approached to zero due to the traffic lights. During the first half period of driving, acceleration changed significantly due to the frequent acceleration and deceleration events; additionally, the exhaust temperature was in the range of 500~650ºC. After the rural and urban driving, the car was driven on the motorways where the speed was increased to nearly 100 km/h from 40 km/h in a short time, and the exhaust temperature was increased up to 800ºC. The exhaust temperature was decreased gradually after a short period of the motorway driving due to low acceleration. During the motorway driving, the acceleration was low. Then, the car was driven on the ring roads from the motorways, followed by a sudden decrease and an increase of speed. The speed was kept at around 85 km/h. After the ring roads, the speed varied in the range of 0~55 km/h with frequent deceleration and acceleration. Huang et al. (Huang et al., 2019) monitored the exhaust temperature of a petrol passenger car, and the monitoring point was at the end of tail-pipe where the exhaust temperature was lower than 130ºC.

Figure 2.4 presents the concentration of NO_x and PN emissions in the real-world driving tests. NO_x concentration changed significantly on the rural roads and urban roads, where the exhaust temperature was higher than 500ºC which ensured high TWC efficiency. The variations of pipe-out NO_x concentration were affected by exhaust flow rates and engine-out concentration. In the motorway driving process, NO_x emission concentration was quite low, benefiting from high exhaust temperature and low variations of the vehicle acceleration (low engine-out concentration). PN concentration was low over motorway driving. Seen from the figures, frequent acceleration and deceleration led to more NO_x and PN emissions. Highest PN concentration has been previously observed under low speed and positive acceleration conditions for a DI petrol car (McCaffery et al., 2020), which agreed with the authors' work. Yang et al. (Yang et al., 2019) demonstrated the relationships between PN concentration and exhaust temperature, the peaks of PN concentration usually corresponding to low temperature events. In the authors' opinion, it was mainly resulted from the high contributions of the liquid phase particles to the total PN emissions. It has been noted that there is a delay of 5 to 10 seconds in PN and NOx emissions from the vehicle speed and acceleration. The reason is not unclear and further research is needed.

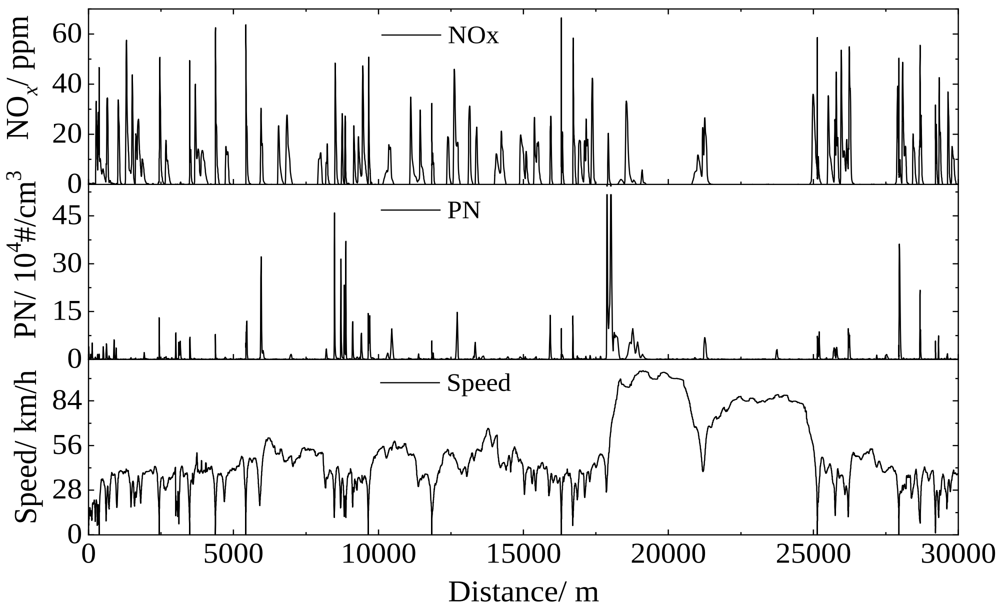

Figure 2.4: P-GPF emissions over real-world driving conditions

Operation parameters of P-N-GPF are shown in Figure 2.5. The car running conditions were similar to P-GPF; however, the maximum speed was slightly higher than P-GPF. In addition, P-N-GPF wasn't equipped with any particle removal devices. The overall exhaust temperature was lower than P-GPF, but it was still higher than TWC light-off temperature (approximately 300 ºC).

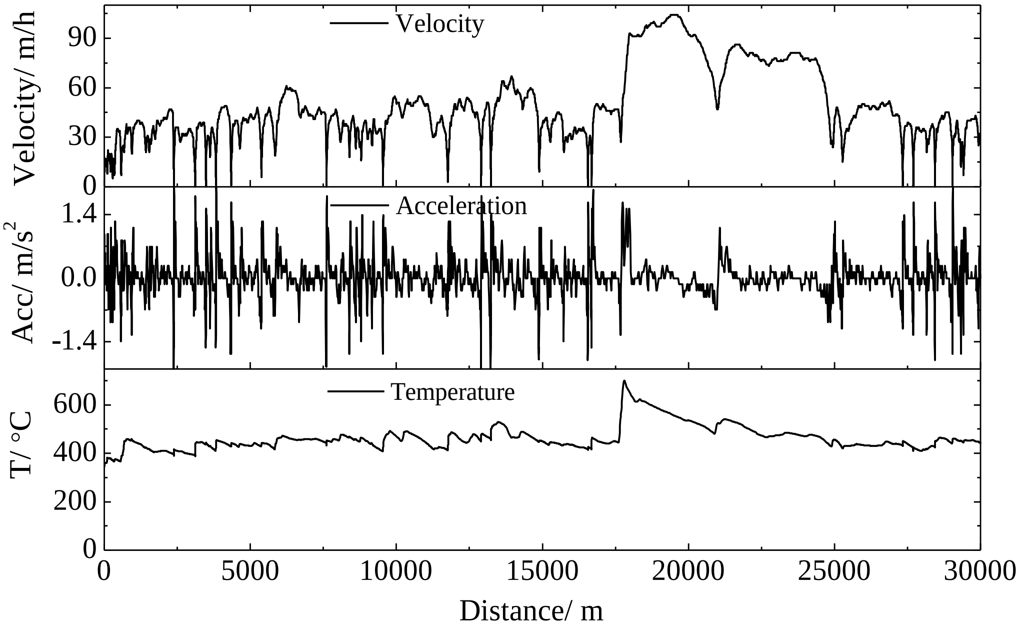

Figure 2.5: P-N-GPF real-world driving conditions

Figure 2.6 shows NO_x and PN concentration during real-world driving conditions. The trend of the emission concentration was significantly different from P-GPF. Over the rural roads and urban roads, the variations of NO_x concentration from P-N-GPF were lower than P-GPF; additionally, NO_x and PN concentration over motorway sections was even higher than other road sections. Since P-GPF was equipped with a GPF, PN concentration was at a quite low level, which was significantly different from P-N-GPF.

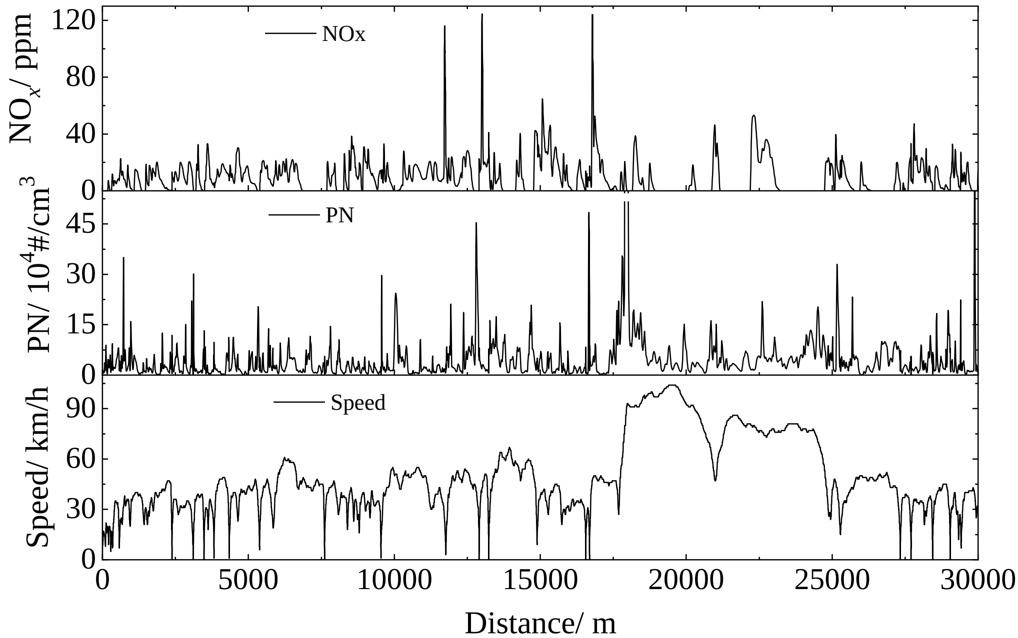

Figure 2.6: P-N-GPF emissions over real-world driving conditions

As indicated in Table 2.1, the compression ratio of P-N-GPF was much higher than P-GPF, leading to the results that the particle size from P-N-GPF was much smaller than P-GPF theoretically (It would have been interesting to study the particle size distribution if such measurements were available). It was one of the reasons leading to high NO_x emissions for P-N-GPF in the authors' opinion. PN concentration of the petrol cars (Suarez-Bertoa et al., 2019) was much higher than the authors' results that the maximum PN concentration was higher than 3×10^7#/cm^3 (Suarez-Bertoa et al., 2019).

Different from P-GPF and P-N-GPF, D-DPF was a diesel car equipped with a diesel oxidation catalyst (DOC), a DPF, and a selective catalytic reduction (SCR). The running parameters of this car are shown in Figure 2.7.

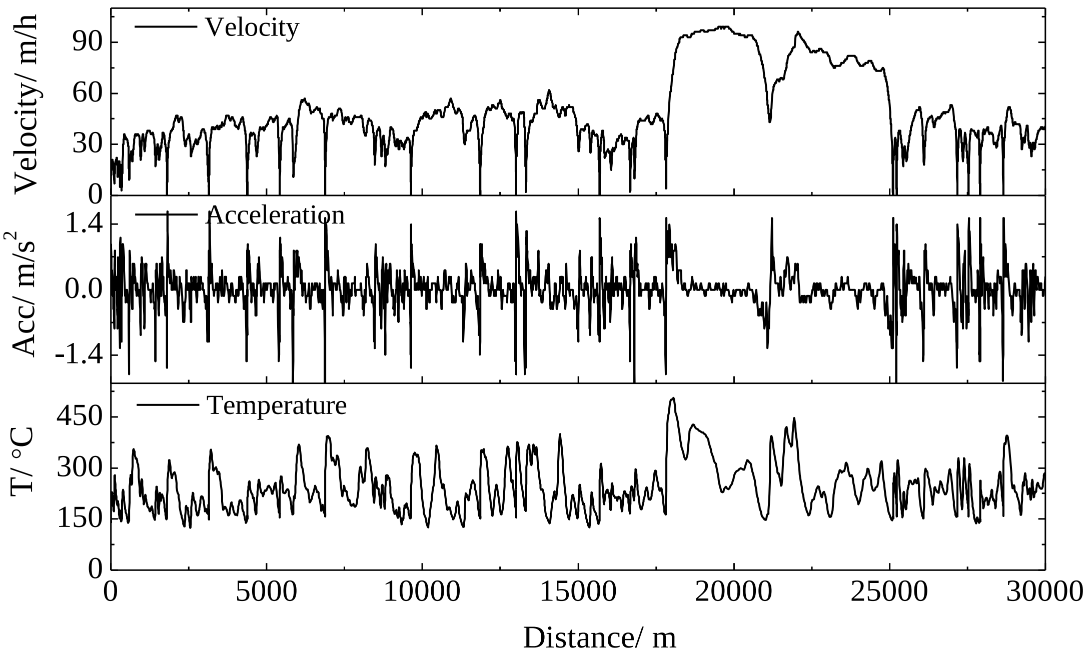

Figure 2.7: D-DPF real-world driving parameters

There were not many differences among the three cars regarding speed. Because of the low combustion temperature of diesel engines, the exhaust temperature of D-DPF was much lower than P-GPF and P-N-GPF; additionally, the exhaust temperature was dropped below the SCR light-off temperature (180 ºC) over several sections, resulting in low NO_x removal efficiency. The temperature during the driving was in the range of 140 ºC~480 ºC. It was mainly caused by the fact that the diesel engine load was mainly controlled by the air/fuel mixture equivalence ratios which had much more impacts on the exhaust temperature than engine speed. Over the sub-urban driving conditions, the exhaust temperature before after-treatment of a diesel passenger car was around 140 ºC, with the speed being lower than 40 km/h and frequent start-stop events (Wang et al., 2018). NO_x and PN concentration over the real-world driving is shown in Figure 2.8. Over most of the operation conditions, NO_x concentration was at a very low level, except for short periods of large acceleration process and low exhaust temperature sections. PN concentration of this diesel car was much lower than petrol cars with the highest PN concentration lower than 900#/cm^3.

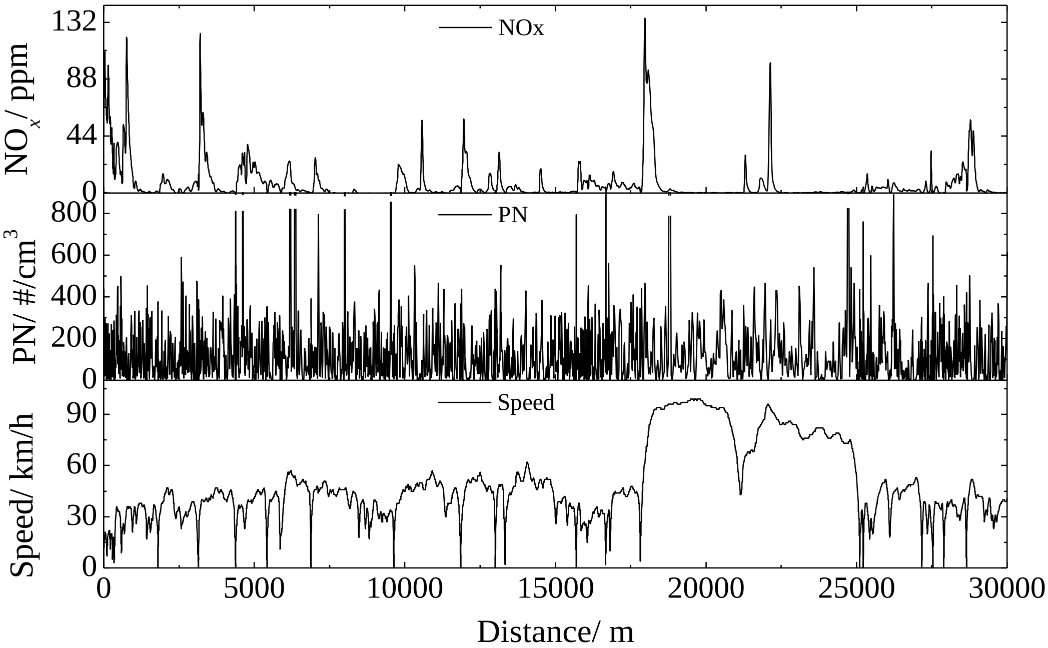

Figure 2.8: D-DPF emissions over real-world driving conditions

2.1.2.2 Relationships between emissions and driving behaviours

Based on the real-world tests, the relationships between speed, acceleration and both NOx and PN are presented in this section. Speed and acceleration are varied over intervals of width 2 km/h and 0.1 m/s^2. Figure 2.9 shows NO_x distributions over speed and acceleration. The left and right graphs are on different scales, with the left graphs on the same scale (i.e. between 0.04 and 0.36) for a direct comparison between the cars, and the right graphs on different scales to show different distributions (e.g. 0.02 – 0.18 for Car a).

As can be seen, the variations of the acceleration for P-GPF (car (a) in the figure) were smaller than the other two cars over the speed range of 25 km/h~40 km/h. It was consistent for the three cars that low NO_x emission rate regions were in the low acceleration (<0 m/s^2) and high speed (>30 km/h) regions. Low acceleration process corresponded to small engine torque which led to low in-cylinder combustion temperature theoretically, resulting in a small quantity of NO_x formations. For both petrol cars, high speed (mainly on motorways) delivered very low NO_x emission rates, which resulted from small acceleration and excellent performance of TWCs. However, it was different for the diesel car which also presented high emission rates over some sections of high speed. In the authors' opinion, it was mainly caused by (1) more NO_x formations due to acceleration; (2) high exhaust temperature which might exceed the optimal temperature (200~400 ºC) of the SCR efficiency. Additionally, it seemed that high emission rates were more dispersive for the petrol cars than the diesel car. It was indicated by Cha et al. (Cha et al., 2019), high NO_x emission rates may happen at high speed in urban area and over acceleration process on motorways for a passenger car equipped with a SCR system; however, NO_x emission rates of the one with LNT were high in the whole driving process.

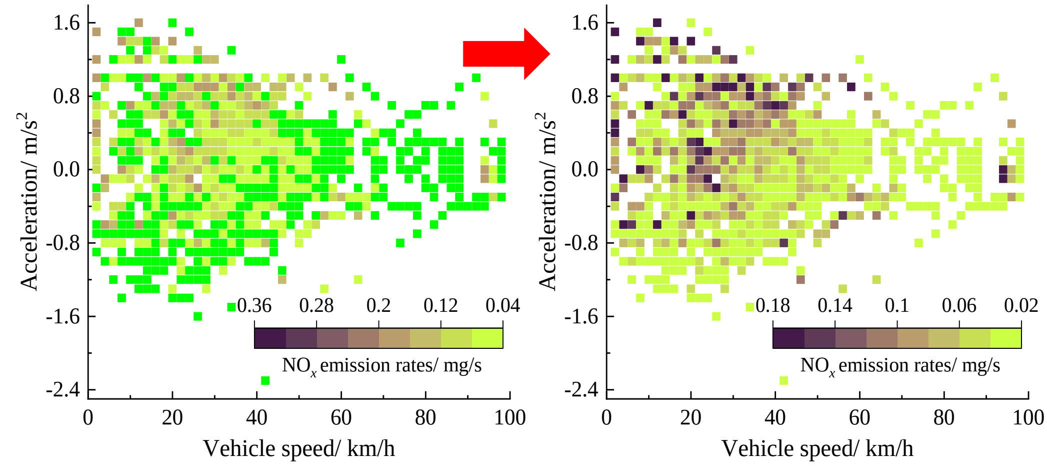

Car (a) P-GPF

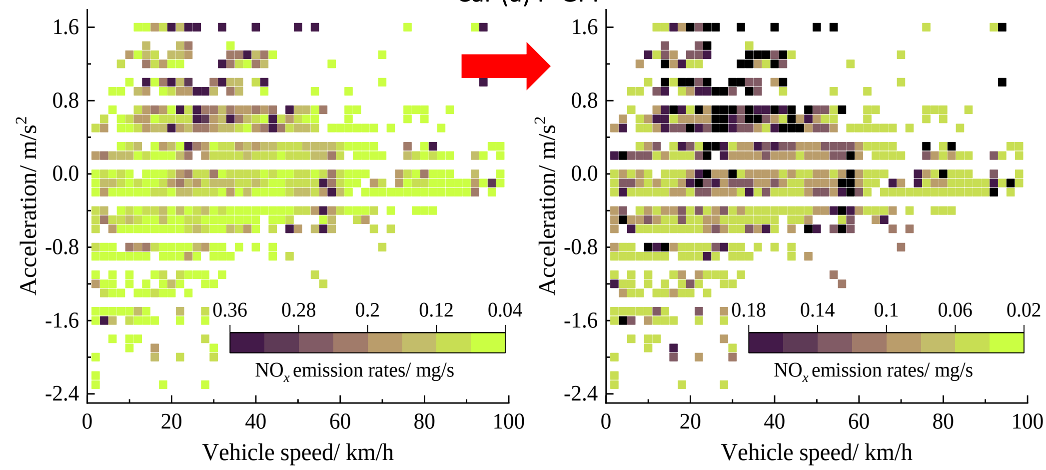

Car (b) P-N-GPF

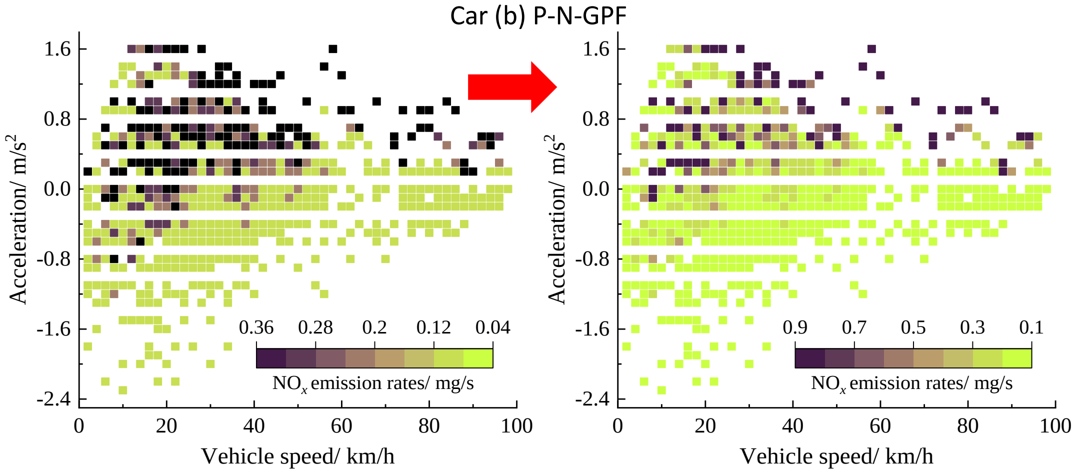

Car (c) D-DPF

Figure 2.9: NO_x distributions over driving behaviours

Figure 2.10 shows PN distributions over speed and acceleration. For the three cars, variations of PN emission rates were significant; in the meantime, high PN emission rates were mainly in the acceleration process and high speed regions. Regarding particles, they included the nucleation mode and accumulation mode. The nucleation mode particles were much smaller than accumulation mode ones, as indicated in previous work (Wang et al., 2017). For engine-out PN distributions over particle size, two peaks were usually observed with one corresponding to diameter smaller than 50 nm and the other being in the range of 100~200 nm which corresponded to the nucleation mode and accumulation mode, respectively (Lin et al., 2021). Regarding GPFs and DPFs, they were more effective in removing large particles than small ones; in the meantime, the main ingredients were also different for nucleation mode particles and accumulation mode particles (Reijnders et al., 2018).

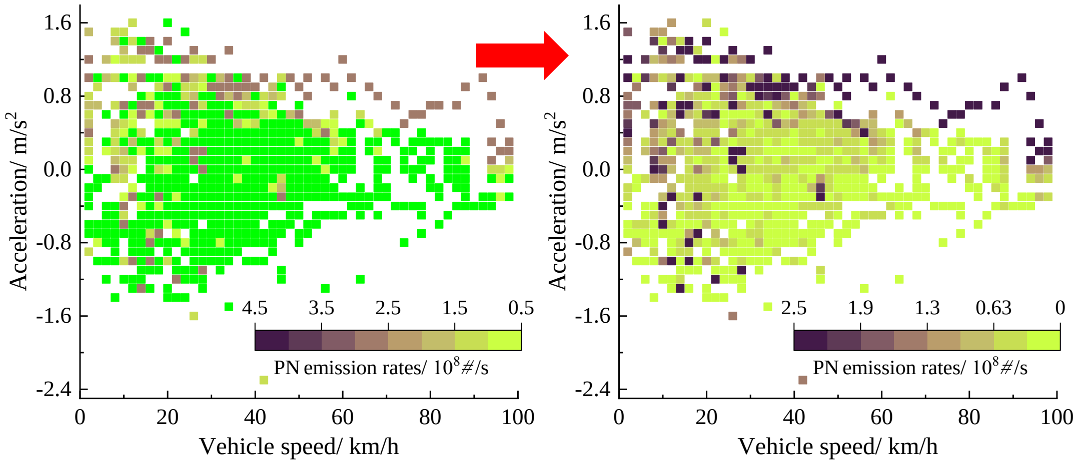

Car (a) P-GPF

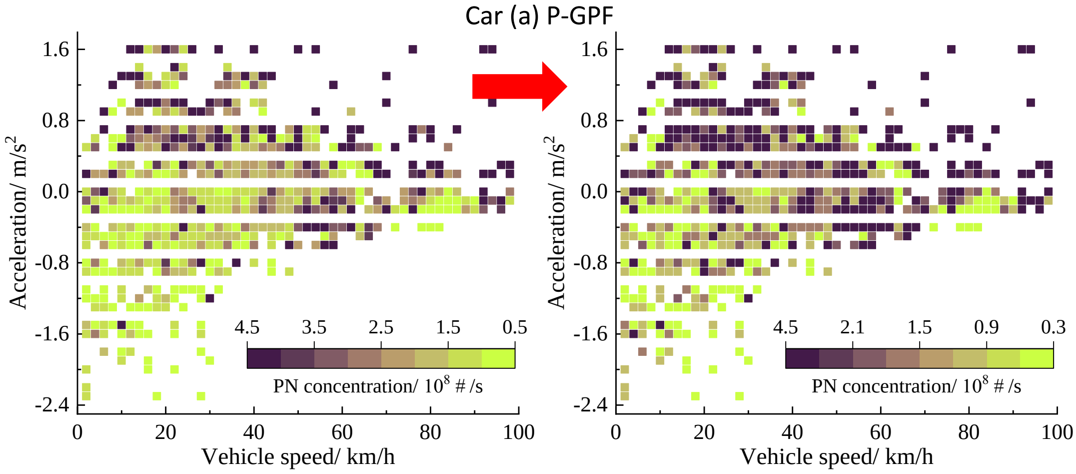

Car (b) P-N-GPF

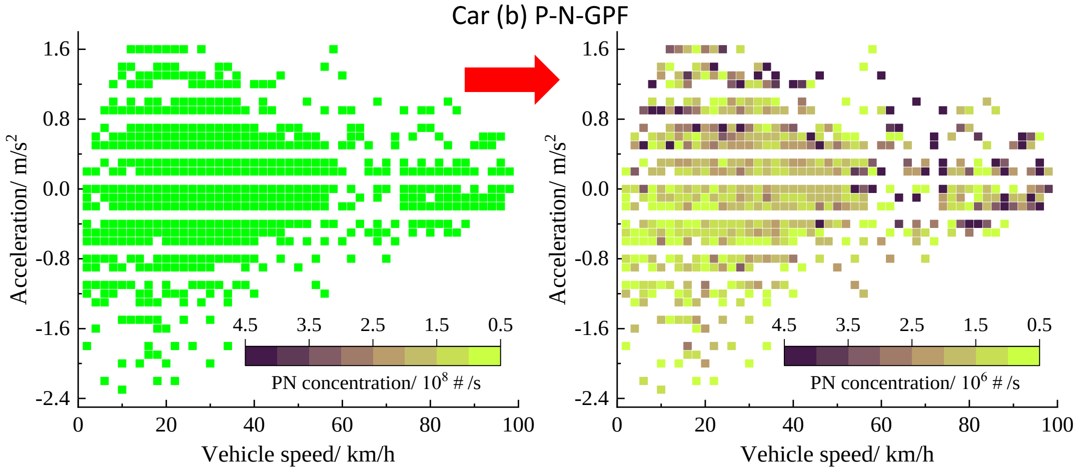

Car (c) D-DPF

Figure 2.10: PN distributions over driving behaviours

In addition, the condensations of HC contributed to the increase of nucleation mode particles (Young et al., 2012) which were hard to be captured by GPFs and DPFs. As demonstrated by (Wihersaari et al., 2020) based on a diesel passenger car under deceleration process, the particle size tended to be smaller, and PN emission rates were higher than idle conditions if without DPFs; in the meantime, the highest PN concentration corresponded to the particle size being smaller than 30nm. However, the particles size for maximum PN concentration was larger than 30 nm under normal driving conditions (Wihersaari et al., 2020). Most of the particle size was smaller than 50 nm for pipe-out particles with DPF (Wihersaari et al., 2020). In the authors' opinion, the engine-out particles and pipe-out particles for PN distributions were different primarily because of different filter efficiency of GPFs and DPFs for various size particles. PN emission rates were higher than 3×10^{11}#/s for diesel passenger car without DPF, and they dropped more than two orders of magnitude after the adoption of DPF, with the maximum PN emission rates being lower than 10^{8}#/s (Wihersaari et al., 2020).

The instantaneous NO_x and PN emission rates are monitored during the test, further the NO_x and PN emission factors can be calculated. The summary of the test results for the three passenger cars is shown in Table 2.2. The average speed of the three passenger cars was similar. P-GPF presented the lowest NO_x emission factors, and D-DPF had the highest NO_x emission factors. PN emission factors of the diesel passenger car were much lower than the other two petrol cars. P-N-GPF showed the highest PN emission factors. P-N-GPF had a high compression ratio than P-GPF, which led to smaller and more particles than P-GPF, which was demonstrated by the work (Di Blasio et al., 2017). Additionally, being without GPF (i.e. the P-N-GPF car) causes high PN emission factors. The PN emission factors of the P-N-GPF were an order of magnitude higher than P-GPF. The combustion modes of the diesel engine and petrol engine were completely different. Significant fuel rich regions exist in the diesel combustion chamber, which leads to larger particle size of diesel engines than the petrol engines. In the meantime, the PN emissions greatly depend on the HC emissions which will be condensed into liquid phase particles, leading to more PN emissions.

Table 2.2: Emission factors of the three passenger cars

	Average speed km/h	NO_x emission factors mg/km	PN emission factors #/km
(a) P-GPF	36.80	3.89	6.8×10^{9}
(b) P-N-GPF	36.75	7.96	4.2×10^{10}
(c) D-DPF	34.4	18.1	1.4×10^{8}

Regarding NO_x emissions, low emissions rates were observed under high vehicle speed conditions for all three cars due to relatively low acceleration. The NO_x emission rates were low over low vehicle speed conditions for both petrol cars during the deceleration processes; however, high NO_x emission points were observed under low speed and small deceleration conditions. Due to the limits of the Euro-6 emission regulations on PN emission, GPF is necessary for the gasoline (petrol) cars to control PN emission; in the meantime, more attention should be paid to petrol cars than diesel cars even for the petrol cars equipped with GPF.

2.1.2.3 Summary

The main conclusions based on the specific passenger cars with given engines are as follows:

(1). The driving patterns of the three cars were similar over the given routes, and the speed changed frequently on the rural and urban roads, leading to the frequent changes of car acceleration. The acceleration variations over motorways are low for the three cars.

(2). Exhaust temperature of both petrol cars was much higher than TWC light-off temperature, especially on the motorways, ensuring the high efficiency of NO_x removal for both petrol cars. Additionally, NO_x concentration was high for rural and motorway driving. Different from both petrol passenger cars, the diesel passenger car presented several high peaks of NO_x concentration, but the NO_x concentration was at a low level in other sections. Maximum PN concentration of the petrol passenger car without a GPF was much higher than the one with a GPF. On motorway, PN concentration of the passenger cars with a GPF/DPF was much lower than the one without a GPF.

(3). NO_x distributions of petrol cars by acceleration and speed were significantly different from those for the diesel car. Higher PN emission rates of the car without GPF were in a larger region than the car with DPF/GPF. PN emission factors of the petrol car without a GPF were much higher than the other two cars.

2.1.3 Significant contribution regions of NO_x and PN emissions

There are some emission peaks generated by aggressive driving situations; the emission peaks are much higher than normal emission rates. There are short durations of journey contributing a significant proportion of the total emissions. The significant contribution regions are the operation conditions where the measures can be taken to effectively decrease the emissions. However, the significant contribution regions of the total emissions have not been investigated under real-world driving conditions for passenger cars to the authors' knowledge. In this section, the key performance indicators (KPIs) evaluating the contributions of high emission peaks, high vehicle acceleration, and high vehicle speed regions to the total NO_x and PN emissions in the real-world driving are put forward. The differences among three petrol cars and a diesel car are discussed.

In this section, four different passenger cars including three petrol cars and one diesel car are used to perform the real-world emission test. The specifications of the four cars are shown in Table 2.3.

Table 2.3 Vehicle specifications of the test cars

Car label		Car-A	Car-B (P-GPF)	Car-C (P-N-GPF)	Car-D (D-DPF)
Car maker		Ford	Opel	Skoda	Skoda
Model		Fiesta	Crossland-X	Octavia	Octavia
Manufacture year		2015	2019	2017	2019
Fuel type		Gasoline (petrol)	Gasoline (petrol)	Gasoline (petrol)	Diesel
Fuel delivery		Direct injection	Direct injection	Direct injection	Direct injection
Aspiration		Turbocharged	Turbocharged	Turbocharged	Turbocharged
Engine size/ L		1.0	1.2	1.5	1.6
Max. power/ kW		73.5	81	110	85
Compression ratio		10.0	10.5	12.5	16.2
Running mass/ kg		1100	1320	1470	1556
After-treatment	Gaseous	TWC	TWC	TWC	DOC+SCR
	Particles	N.A.	GPF	N.A.	DPF
Emission standards		Euro-6a	Euro-6d	Euro-6c	Euro-6d
Gear number (type)		5 (M)	5 (A)	6 (M)	7 (DSG)
Type approval cycle		NEDC	WLTP	NEDC	WLTC
Type approval NO_x (mg/km)		40	17.5	34.1	29.2
Type approval PN (10^{11} #)		N.A.	4.2	1.08	0.02
Type approval CO_2 (g/km)		99	153	115	141

2.1.3.1 Parameter definitions

In this section, the key performance indicators evaluating the regions of the specific contributions to total emissions are defined. As demonstrated by the work (Luján et al., 2018; Mera et al., 2019; Suarez-Bertoa et al., 2019), the majorities of NO_x and PN emissions are dominated by a small part of driving events. For example, peak NO_x emission rates are more than 10 times higher than normal driving (Mera et al., 2019); peak PN emission rates caused by aggressive acceleration events are hundreds times higher than the values for gentler driving (Myung et al., 2020). These driving events are the places where the driving behaviours can be improved to reduce emissions.

Figure 2.11 shows the percentage of the journey time, NO_x emission rates, acceleration, and speed profiles against the percentage of the total NO_x emissions. Additionally, the specific definitions of the KPIs analysed in this chapter are provided in Table 2.4.

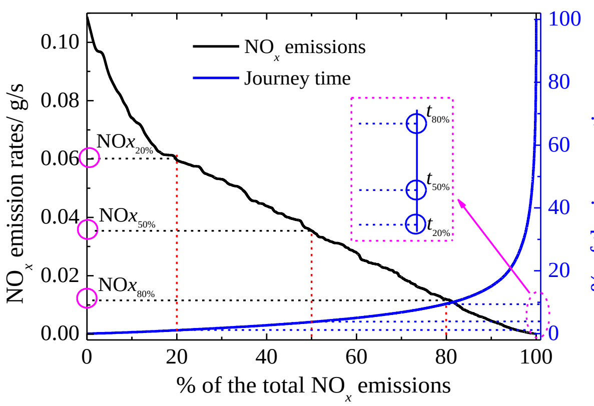

(a) NO_x emission rates, % of the journey time profiles *vs.* % of the total NO_x emissions

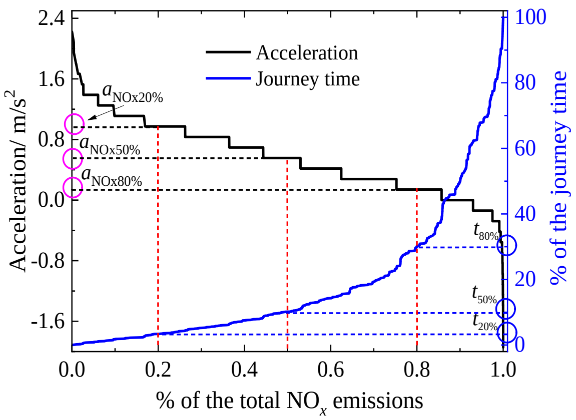

(b) Acceleration, % of the journey time profiles *vs.* % of the total NO_x emissions

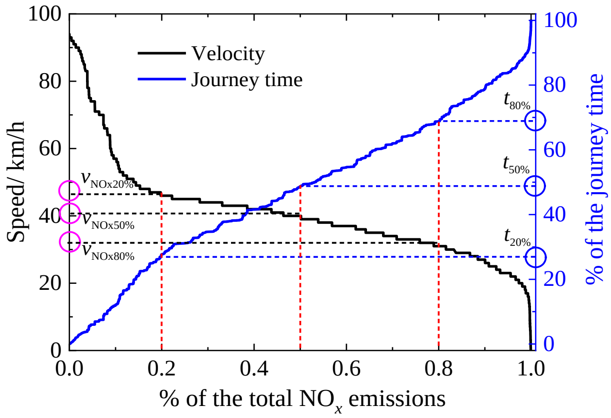

(c) Speed, % of the journey time profiles *vs.* % of the total NO_x emissions

Figure 2.11: NOx emission rates, acceleration, and speed related parameters

Table 2.4 Key performance indicator definitions

KPIs	Definitions	Durations
$NO_{x20\%}$	NO_x emission rates corresponding to 20% of the total NO_x emissions	$t_{20\%}$
$a_{NOx20\%}$	Vehicle acceleration corresponding to 20% of the total NO_x emissions	
$v_{NOx20\%}$	Vehicle speed corresponding to 20% of the total NO_x emissions	
$PN_{x20\%}$	PN emission rates corresponding to 20% of the total PN emissions	
$a_{PN20\%}$	Vehicle acceleration corresponding to 20% of the total PN emissions	
$v_{PN20\%}$	Vehicle speed corresponding to 20% of the total PN emissions	
$NO_{x50\%}$	NO_x emission rates corresponding to 50% of the total NO_x emissions	$t_{50\%}$
$a_{NOx50\%}$	Vehicle acceleration corresponding to 50% of the total NO_x emissions	
$v_{NOx50\%}$	Vehicle speed corresponding to 50% of the total NO_x emissions	
$PN_{50\%}$	PN emission rates corresponding to 50% of the total PN emissions	
$a_{PN50\%}$	Vehicle acceleration corresponding to 50% of the total PN emissions	
$v_{PN50\%}$	Vehicle speed corresponding to 50% of the total PN emissions	

2.1.3.2 Variations of the travel characteristics over different drivers

Driving behaviours vary greatly from driver to driver even on the same route and under similar traffic conditions. Figure 2.12 shows the travel characteristic variations among nineteen drivers, including travel time, average speed, NO_x emission factors, and PN emission factors. Each of the 19 drivers drives every car twice but in this study, only the first run was used. Details about the exhaust emission campaigns are described in MODALES D3.1.

The differences of average travel time and average speed were small between different types of passenger cars; however, the variations of travel time and speed of different drivers with the same car were significant. The average speed was approximately 37.4 km/h, 38.4 km/h, 38.8 km/h, and 38.4 km/h for Car-A, Car-B, Car-C, and Car-D respectively. The average NO_x and PN emission factors of Car-A were much higher than the others, with the average value being approximately 0.14 g/km and 9.9×10^{11}#/km, respectively. Because the emission standard of Car-A met Euro-6a emission regulation where the approval test procedure was based on NEDC. NEDC test procedure is less strict than WLTC, leading to high emission factors of Euro-6a compliant cars under real-world driving conditions. Car-A was a direct injection engine, and was free of GPF. Regarding PN emissions from direct injection gasoline cars, the emission level was the same or even higher than diesel cars. The test results agreed with Kontses et al.(Kontses et al., 2020), indicating that Euro-6 diesel cars with DPF showed lower PN emission factors than Euro-6 gasoline cars without GPF under real-world driving conditions. PN emission factors of the Euro-6 gasoline cars without GPF reached 1.3×10^{13}#/km (Kontses et al., 2020). Regarding the two Euro-6d passenger cars (Car-B and Car-D), the average NO_x emission factors of the diesel passenger car (Car-D) were higher than the petrol car (Car-B); however, the average PN emission factors of the diesel car were much lower than that of the petrol counterpart. Even though the direct injection gasoline passenger car (Car-B) was equipped with GPF, it was still much more difficult to control PN emission than the diesel car.

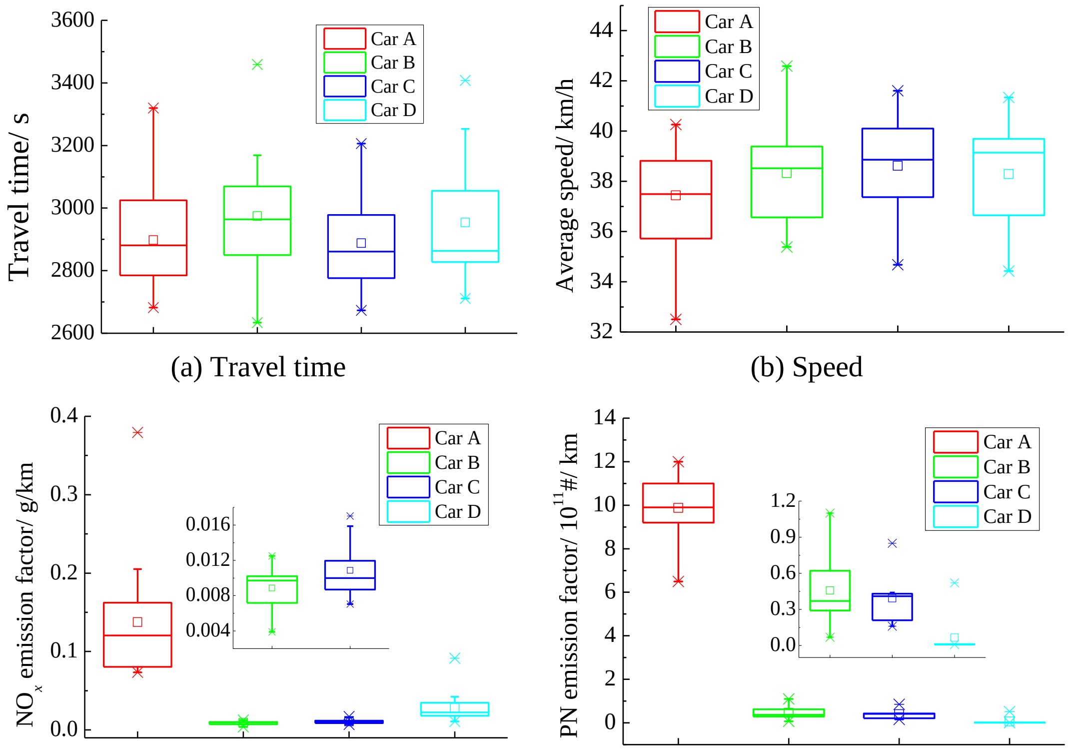

(a) Travel time (b) Speed

(c) NO_x emission factors (d) PN emission factors

Figure 2.12: Travel characteristics over the matrix of nineteen drivers and four cars

2.1.3.3 Variations of NO_x related KPIs

High emission regimes usually have a significant contribution to the total emissions and account for a small proportion of total travel time. Figure 2.13 shows the variations of NO_x emission rates and corresponding durations over 20% and 50% of the total NO_x emissions. Average $NO_{x20\%}$ was approximately 0.038 g/s for Car-A, and the corresponding $t_{20\%}$ was lower than 1%; in the meantime, the variations of NO_x emission rates from Car-A were the largest among the four cars. It implied that very short operation durations led to much higher NO_x emissions. The drivers' driving behaviours played a more important role in the real-world NO_x emissions of Car-A than the other cars. Large variations in average $NO_{x20\%}$ meant high possibilities of high emission rate points. The average $NO_{x20\%}$ of Car-B was the lowest, approximately 0.0005 g/s. The $NO_{x20\%}$ variations of Car-B were much smaller than the other cars; however, the variations of corresponding $t_{20\%}$ were the biggest. For the Euro-6d compliant cars in the test (i.e. Car-B and Car-D), the average $NO_{x20\%}$ of the diesel car (Car-D) was higher and its $t_{20\%}$ was lower than that of the gasoline car (Car-B). Average $t_{20\%}$ corresponding to $NO_{x20\%}$ was the lowest for the diesel car, indicating that high emission peaks were more important to total NO_x emissions for this diesel car than the others. The analysis also showed that $NO_{x20\%}$ had an opposite tendency with corresponding $t_{20\%}$; high emission cars tended to present small values of average $t_{20\%}$. Low NO_x emission cars had few NO_x emission peaks. Average $t_{20\%}$ corresponding to $NO_{x20\%}$ was smaller than 3.5% for all the cars in the test. It emphasized the importance of high emission regimes.

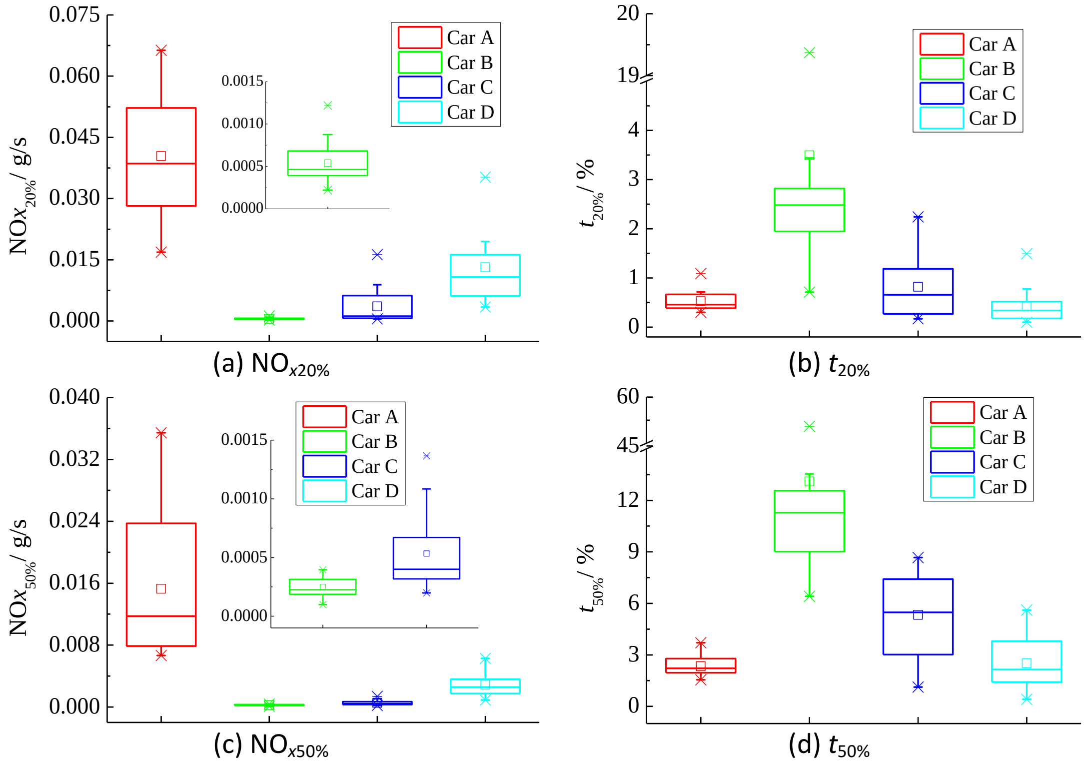

Figure 2.13: NO_x emission rates and corresponding durations over 20% and 50% of total NO_x

$NO_{x50\%}$ and corresponding $t_{50\%}$ had a similar tendency to $NO_{x20\%}$ and corresponding $t_{20\%}$ respectively. Average $NO_{x50\%}$ of Car-A was approximately 0.015 g/s, and it was lower than 0.0006 g/s for the other two gasoline cars in the test. Average $NO_{x50\%}$ of the diesel passenger car was approximately 0.0035 g/s. Average $t_{50\%}$ of the four cars corresponding to $NO_{x50\%}$ was smaller than 13%; Car-B presented the highest mean value; average $t_{50\%}$ was approximately 3% for Car-A and Car-D.

Vehicle acceleration is considered to be the most important factor leading to high NO_x emissions. Figure 2.14 shows $a_{20\%NOx}$, $a_{50\%NOx}$, and corresponding $t_{20\%}$ and $t_{50\%}$ of the four cars. $a_{20\%NOx}$ presented a reverse tendency to corresponding $t_{20\%}$ for the four cars. Average $a_{20\%NOx}$ was in the range of 0.6 m/s^2~ 1.35 m/s^2, with corresponding $t_{20\%}$ being in the range of 2%~ 11%. Average $a_{20\%NOx}$ was the highest and corresponding $t_{20\%}$ was the lowest for Car-D among the four cars. It implied that the NO_x emissions of the diesel car (Car-D) were more sensitive to acceleration than the other cars. $a_{20\%NOx}$ had the smallest value and corresponding $t_{20\%}$ was the highest for Car-B. It was noted that fewer NO_x emission peaks were observed in the aggressive driving process for Car-B; NO_x emissions of Car-B were less dependent on the acceleration than the other cars. The differences in average $a_{20\%}$ were small for the three petrol cars.

Average $a_{50\%NOx}$ of Car-B approached to zero, and the corresponding $t_{50\%}$ was approximately 44%. It indicated that the deceleration process of Car-B contributed the highest proportion to total NO_x emissions among the four cars; and the variations were low. Regarding Car-D, average $a_{50\%NOx}$ was still higher than 0.6 m/s^2 and corresponding $t_{50\%}$ was lower than 12%. The distributions of NO_x emission rates were significantly unevenly dispersed. This finding was consistent with previous studies (Ko et al., 2019; Mendoza-Villafuerte et al., 2017) where NO_x emission rates were quite low under real-world driving conditions as long as the engines were fully warmed up except for some aggressive driving conditions. Small variations of $a_{20\%}$ and $a_{50\%}$ showed high tolerances of the cars to the driving behaviour variations, contributing to dropping high emission peaks.

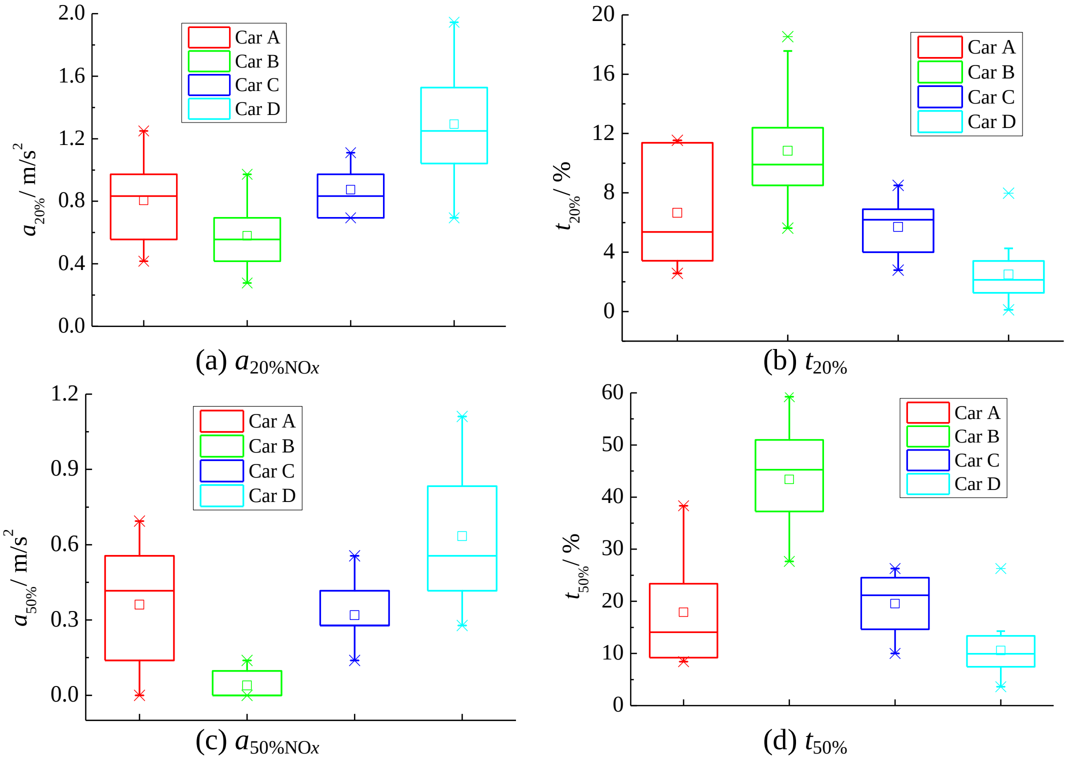

Figure 2.14: Acceleration and corresponding durations over 20% and 50% of total NO_x emissions

The average speed and corresponding durations over 20% and 50% of the total NO_x emissions are shown in Figure 2.15.

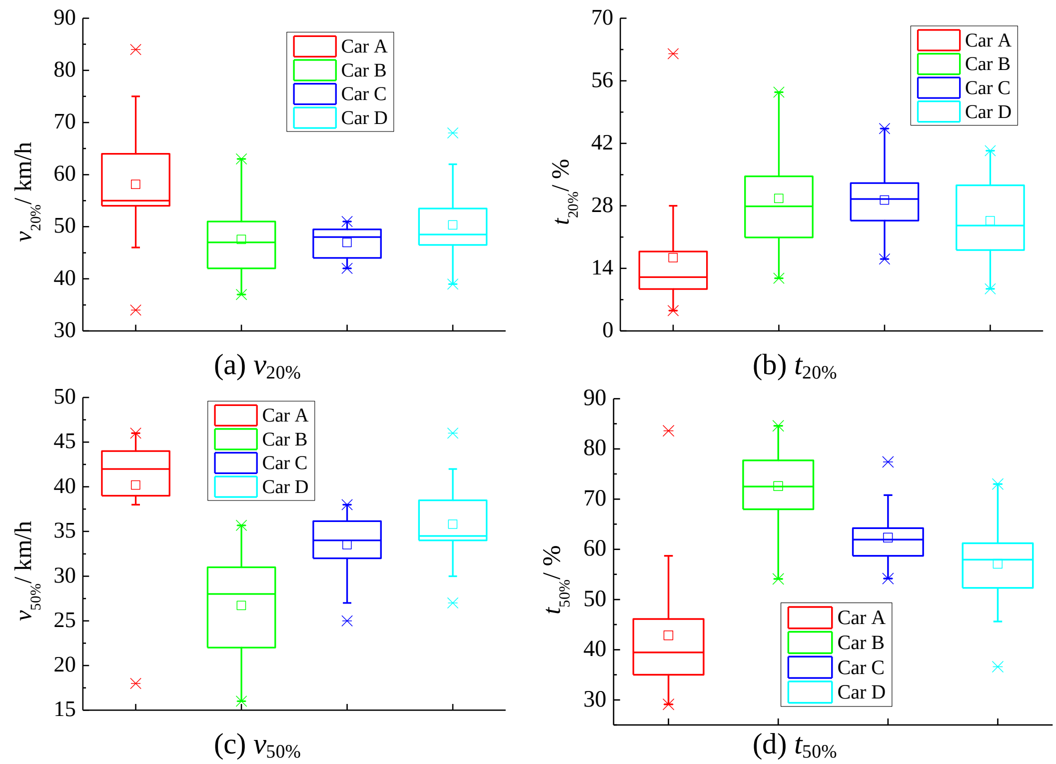

Figure 2.15: Vehicle speed and corresponding durations over 20% and 50% of total NO_x emissions

The average $v_{20\%NOx}$ was in the range of 45 km/h~58 km/h; the corresponding $t_{20\%}$ ranged from 17% to 31%. The NO_x emissions were less dependent on the speed than the acceleration, concluding from the comparisons of Figure 2.14 and Figure 2.15.

The differences of average $v_{20\%NOx}$ among Euro-6c and Euro-6d passenger cars were minor. Regarding Euro-6c and Euro-6d passenger cars, NO_x emissions under high speed conditions were lower than the average level because $t_{20\%}$ corresponding to $v_{20\%NOx}$ was higher than 20%. Average $v_{50\%NOx}$ was in the range of 27 km/h~ 41 km/h, with the corresponding $t_{50\%}$ being higher than 50% except for Car-A. It meant that much NO_x were generated under low speed conditions where the exhaust temperature was too low to ensure high NO_x removal efficiency. Average $t_{50\%}$ corresponding to $v_{50\%NOx}$ was approximately 73% for Car-B, indicating the NO_x emissions were dominated by low speed operations.

2.1.3.4 Variations of PN related KPIs

Euro-6 emission standard limits both PM and PN emissions for direct injection cars and diesel cars. DPF and GPF are effective to reduce PM emission, and PN emission is still a challenge. Figure 2.16 shows $PN_{20\%}$, $PN_{50\%}$, and corresponding durations over 20% and 50% of the total PN emission.

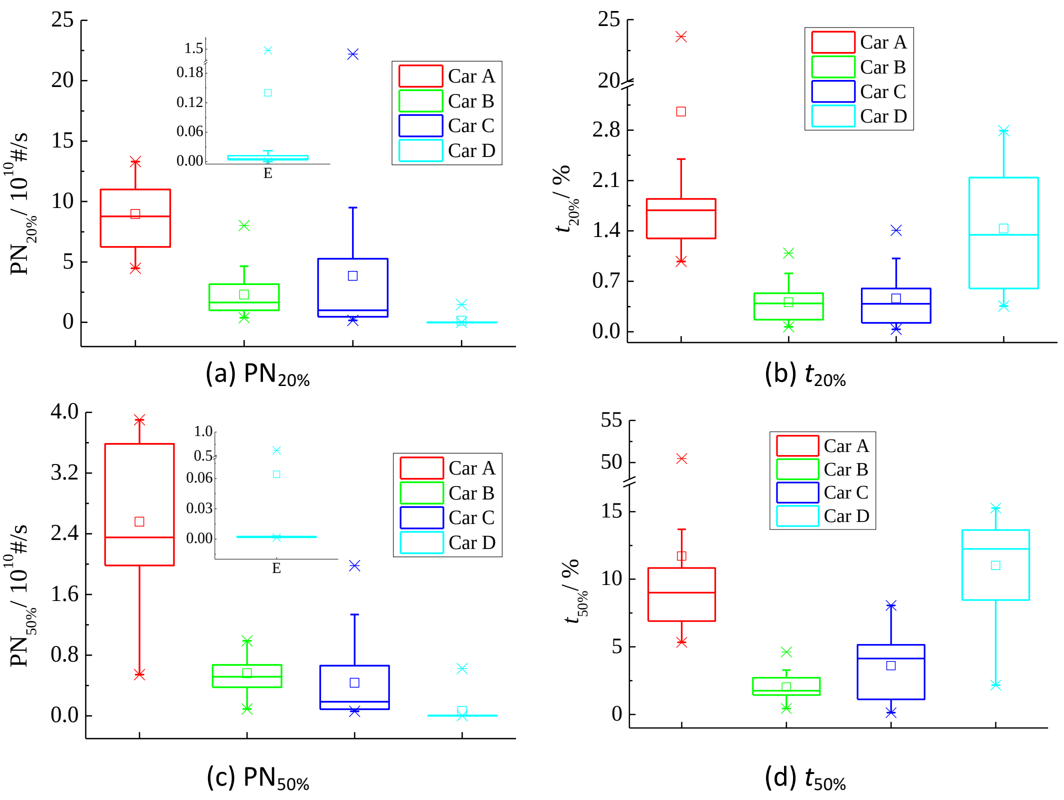

Figure 2.16: PN emission rates and corresponding durations over 20% and 50% of total PN

Average $PN_{20\%}$ was the lowest and the variations were the smallest for the diesel car (Car-D). Average $t_{20\%}$ corresponding to $PN_{20\%}$ was smaller than 3%, indicating the PN emission peaks were much higher than normal values. In the meantime, average $t_{20\%}$ corresponding to $PN_{20\%}$ for Car-B and Car-C was smaller than 0.5%, showing that a small amount of vehicle operation points contributed 20% of the total PN emissions. More focus should be paid to PN emission peaks from direct injection petrol cars even for cars with GPF systems. Variations of $t_{20\%}$ and $t_{50\%}$ for PN emission were higher than NO_x emissions. PN emission peaks were more sensitive to driving behaviours than NO_x emissions. Mendoza-Villafuerte et al. (Mendoza-Villafuerte et al., 2017) pointed that high PN emission peaks over aggressive driving were hundreds times higher than normal driving conditions. Particle emissions included both solid-phase and liquid-phase particles (Liu et al., 2010; Meloni and Palma, 2020). Solid-phase particle formations were mainly determined by in-cylinder combustion conditions; liquid-phase particles were affected by in-cylinder combustion and tailpipe temperature evolutions. Low temperature in tailpipes contributed to the formations of secondary liquid-phase particles. Part of the gaseous HC was condensed into liquid-phase particles which were also counted by PEMS.

PN emission formations were significantly dependent on in-cylinder combustion temperature which was really high in the vehicle acceleration process due to much fuel delivery. Particle emission included both solid-phase and liquid-phase particles. The acceleration process not only affected the solid-phase particle formations but also the liquid-phase particles. Additionally, liquid-phase particle size was usually smaller than solid-phase particles. Figure 2.17 shows the car acceleration and corresponding durations over 20% and 50% of the total PN emission. Average $a_{20\%PN}$ was in the range of 0.6 m/s^2~1.4 m/s^2, and the corresponding $t_{20\%}$ ranged from 1.5% to 10% for the given passenger cars. $a_{20\%PN}$ was the highest for Car-B and the lowest for Car-D. It was inconsistent with NO_x emissions. PN emission of the diesel car (Car-D) was less sensitive to the acceleration than the other three cars; it was the most sensitive for Car-B. Average $a_{50\%PN}$ tendency was consistent with $a_{20\%PN}$ for all the four passenger cars. Average $t_{50\%}$ was in the range of 6%~32%. High PN emission rates not only happened in high acceleration process but also normal driving conditions, especially for the diesel car (Car-D) whose $a_{20\%}$ was approximately 0.75 m/s^2.

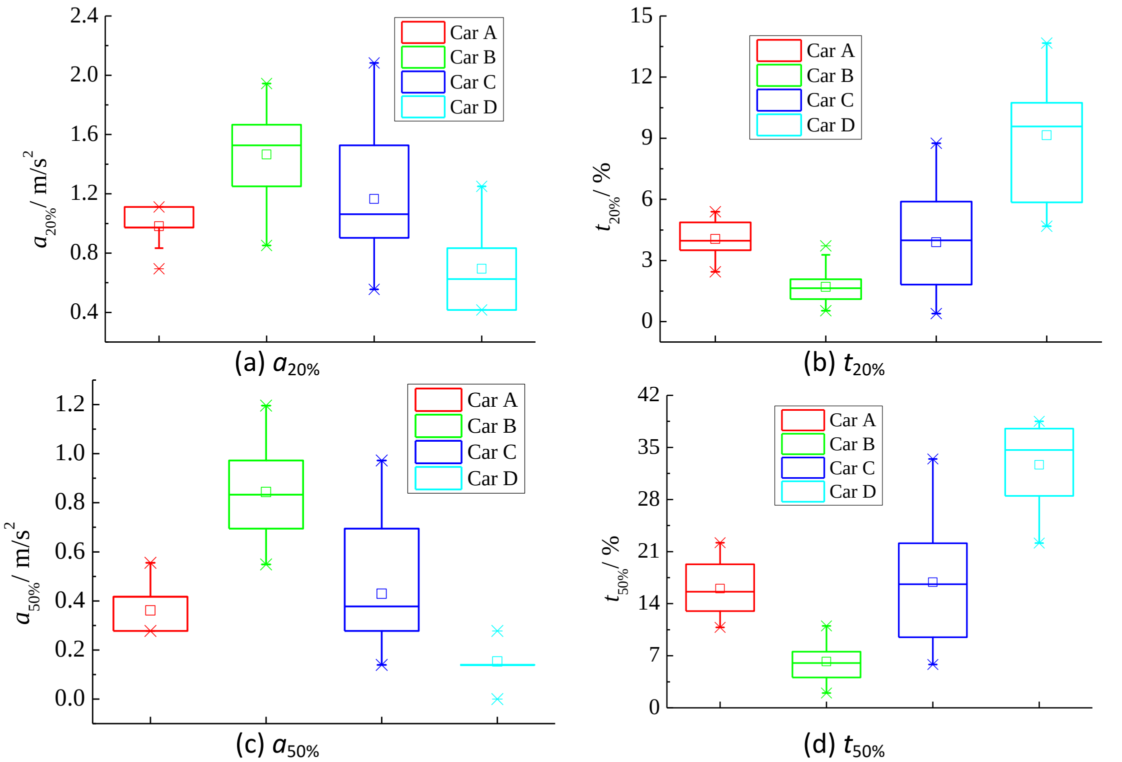

Figure 2.17: Acceleration and corresponding durations over 20% and 50% of total PN emission

Variations of $v_{20\%}$, $v_{50\%}$ and corresponding $t_{20\%}$ and $t_{50\%}$ are presented in Figure 2.18. The average $v_{20\%}$ was in the range of 53 km/h~73 km/h, and the differences among the four cars were significant. The variations of $v_{20\%}$ and corresponding $t_{20\%}$ for Car-B were much bigger than the other three cars; $t_{20\%}$ was in the range of 7%~22%. Car-C showed the highest value of average $v_{20\%}$ and the lowest value of corresponding average $t_{20\%}$. It implied that PN emission factors of Car-C were sensitive to high speed regions. $v_{50\%}$ of the four passenger cars was in the range of 33 km/h~50 km/h, and corresponding $t_{50\%}$ ranged from 30% to 62%. It meant the PN emission factors were less sensitive to the speed than acceleration for all the cars.

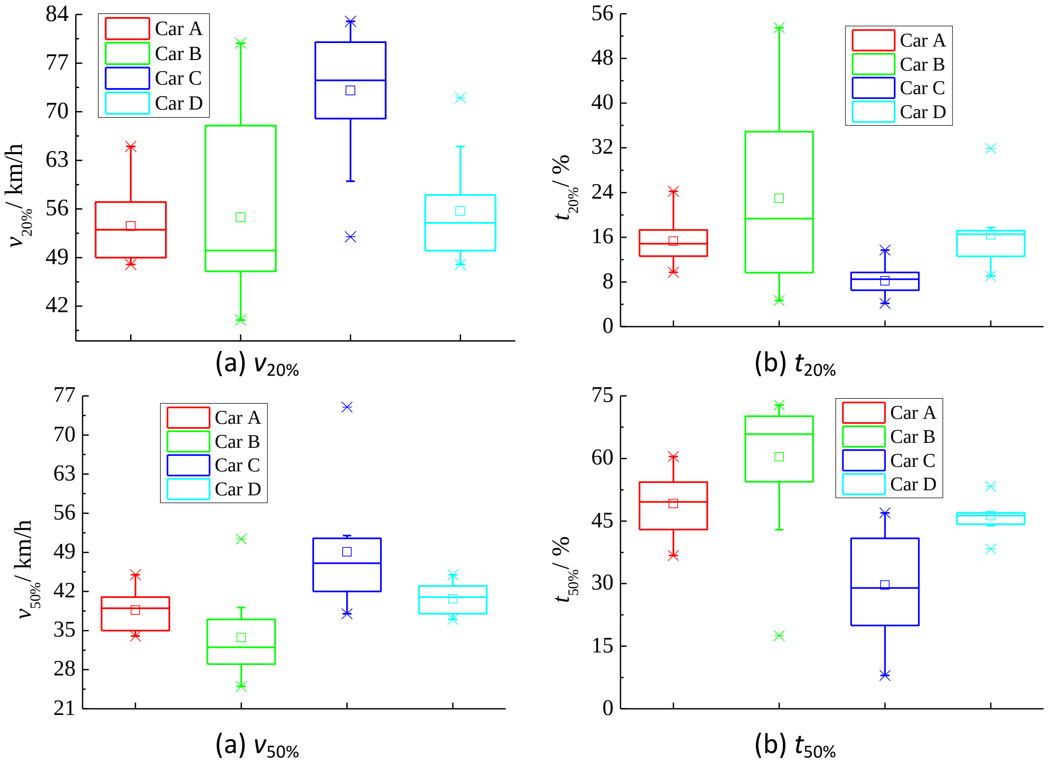

Figure 2.18: Vehicle speed and corresponding durations over 50% of the total PN emission

2.1.4 Summary

NO_x and PN exhaust emissions of three Euro-6 compliant gasoline cars and a Euro-6 diesel car are monitored using PEMS in the real-world driving. Specific contribution regions of NO_x and PN emissions to total emissions are analysed using the authors' defined KPIs. Main conclusions are as the follows:

(1). The Euro-6a gasoline (petrol) car had much higher average NO_x and PN emission factors than the other three passenger cars, partly caused by the different type approval driving cycle used in the emission regulations and being free of GPF. NO_x emission factors of the diesel car (Euro-6d) were higher than the Euro-6c and Euro-6d gasoline cars; however, PN emission factors were much lower although the Euro-6d gasoline cars had GPFs.

(2). Average $NO_{x20\%}$ and $NO_{x50\%}$ presented the same pattern for the four cars, and they were consistent with the average NO_x emission factors. Cars having lower average NO_x emission factors had lower variations of $NO_{x20\%}$ and $NO_{x50\%}$. High emission peaks in the real-world driving presented significant contribution to total emissions for the Euro-6a gasoline car and the diesel car whose $t_{20\%}$ corresponding to $NO_{x20\%}$ was lower than 1%.

(3). Average $a_{NOx20\%}$ of the diesel car was the highest, and the corresponding $t_{20\%}$ was the lowest among the four cars. NO_x emission factors of the diesel car were much more dependent on the acceleration than the gasoline cars. Average $t_{20\%}$ corresponding to $v_{NOx20\%}$ was in the range of 10%~30%. NO_x emission factors were less sensitive to vehicle speed than acceleration.

(4). The trend of average $PN_{20\%}$ and $PN_{50\%}$ by car types were consistent with PN emission factors. PN emission peaks had really high contributions to total PN emission because average $t_{20\%}$ corresponding to $PN_{20\%}$ was lower than 2% for all the four passenger cars. The average $t_{20\%}$ corresponding to $a_{PN20\%}$ was the lowest for the Euro-6d gasoline car and it was the highest for the diesel car. PN emission of the Euro-6d petrol car (Car-C) was the most sensitive to vehicle acceleration, and the diesel car (Car-D) was the least sensitive to the acceleration. PN emission of the cars depended more on the vehicle acceleration than speed.

2.2 Brake wear emissions

2.2.1 Descriptions of the brake system and sampling apparatuses

The brake system of reference vehicle (see Figure 2.19) was used in the dynamometer enclosed in a sealed chamber to measure the brake ware emissions under WLTP-brake cycle. The detailed information on the reference vehicle is summarised in Table 2.5. A novel WLTP-brake cycle was proposed by (Mathissen et al., 2018) to establish the standard test procedure for measuring brake wear particle emissions. They investigated 700,000 driving data points gathered from the US, EU, Korea, Japan, and India to develop a novel WLTP-Brake cycle. This WLTP-Brake cycle has a test time of 4 h 24 min, without soak times between trips, with 303 braking events, divided into 10 trips.

Figure 2.19: The tested brake system of reference vehicle (Ford Focus)

Table 2.5: Parameters of the car and its brake system.

	Passenger car
Manufacturer	Ford Motor Company
Model	Focus
Vehicle weight	1600 kg
Engine	1.0 L EcoBoost (92 kW, 125 PS)
Rims	6.5 x 16”
Tyres	205/55 R16
Front brake disc	278 x 25 mm
Rear brake disc	271 x 11 mm solid

Figure 2.20 shows experimental setup, including the brake dynamometer, wind tunnel, and various instruments for measuring the brake wear particles. This rotating weight simulates the momentum of inertia of 49.3 kg m^2, which is equivalent to vehicle curb weight plus 1.5 passengers and with an assumed a brake force distribution of 60% on the front axle. Moreover, the inertia was reduced of the 13% with respect its nominal value of 56.7 kg m^2 to take into account the vehicle parasitic losses.

A thermocouple was mounted in the disc to measure the disc temperature and was embedded at the side surface of the disc at a depth of 0.5 mm. The entire brake system was enclosed in an elliptical chamber with a major diameter of 1100 mm, a minor diameter of 700 mm and a depth of 900 mm. Clean air was supplied to the circular chamber through a high-efficiency particulate air filter (HEPA H13) to maintain the chamber in a zero-particle state. Brake wear particles mixed with clear air escaped from the circular chamber to a wind tunnel with a diameter of 150 mm and a length of 3.5 m. Sufficient length of the wind tunnel was designed to achieve a well-developed airflow at the sampling plane. Isokinetic sampling probes were installed at the wind tunnel and were located at 5 hydraulic diameter downstream of the last flow disturbance element and 2.5 diameters upstream of the last flow disturbance element. Sampling nozzles were designed considering the total chamber flow and the flow rate of each particle measurement instrument. A hot wire anemometer was installed upstream of the brake enclosure to measure the total flow rate. A flow rate of 65 m^3/h, which had a 3.8 km/h. The air exchange time of the circular chamber was between 1 and 5 s, so a fast response is possible for measuring brake wear particles.

Figure 2.20: The dynamometer enclosed in a sealed chamber and analysis apparatuses

The PM particles were collected using 25mm aluminium substrate placed in a stainless-steel three stage impactor from Dekati holder. The aluminium collection substrates were coated with a stable vacuum grease to prevent the particle bouncing and re-entrainment. Prior to the impactor, a cyclone (Dekati) was used to separate the particles with an aerodynamic diameter larger than 11.5 µm. Then the ultra-micro-balance with a sensitivity of 10^{-4} mg was used to measure the PM mass. Prior to measurement, the balance kept in 24 hours of conditioning at 22.0 ± 1°C and 45 ±3 % RH. To avoid any error due to the manual handling of the collection substrates, the weighing procedure is fully automated and carried out by a robotic arm. The counting of the particles (PN) with diameter in the interval 0.004-10 µm was performed with a condensation particle counter (CPC) model 3775 from TSI. The particle size distribution (PSD) was also measured with an electric low-pressure impactor (ELPI+) (Dekati) that measures particles within the range 0.006-10 µm. Both PM collection on quartz filter as well as counting of the particles with ELPI+ was done at a flow rate of 10 $L \cdot min^{-1}$ while the CPC flowrate was of 1.5 $L \cdot min^{-1}$.

2.2.2 Wear induced PM and PN emissions during WLTP-brake cycle

The WLTP brake test consists of 10 trips, totalling 192 km with 303 braking events. Figure 2.21 shows the vehicle speed profile during the WLTP brake cycle. At the beginning of WLTP brake cycle, there is relative low speed profile. The largest speed has been reached by larger than 130 km/h in the trip 10. Figure 2.22 shows the PM_{10}, $PM_{2.5}$ and PM_1 emissions emitted from brake wear during TWTP brake cycle. It can be seen that from this figure, PM_{10}, $PM_{2.5}$ and PM_1 present similar evolution trend during the WLTP brake cycle. At the same brake events, the brake wear generates more PM_{10} particles, followed by PM2.5 and PM1. Among 303 braking events, the worst brake event in terms of wear is #295, from 132.5 km/h to 34.0 km/h with a deceleration of 1.82 m/s^2 and a final rotor temperature of 150.2 ° C. In the meantime, this brake event lasts the longest sliding distance. The lightest brake event in terms of wear is #219, from 12.36 km/h to 0 km/h with a deceleration of 1.14 m/s^2 and an initial and final rotor temperature of 53.4 ° C and 54.0 ° C. The substantial particle emissions observed at #295 event is attributed to the severe shear deformation at the sliding interface due to high sliding velocity (Alemani et al., 2016).

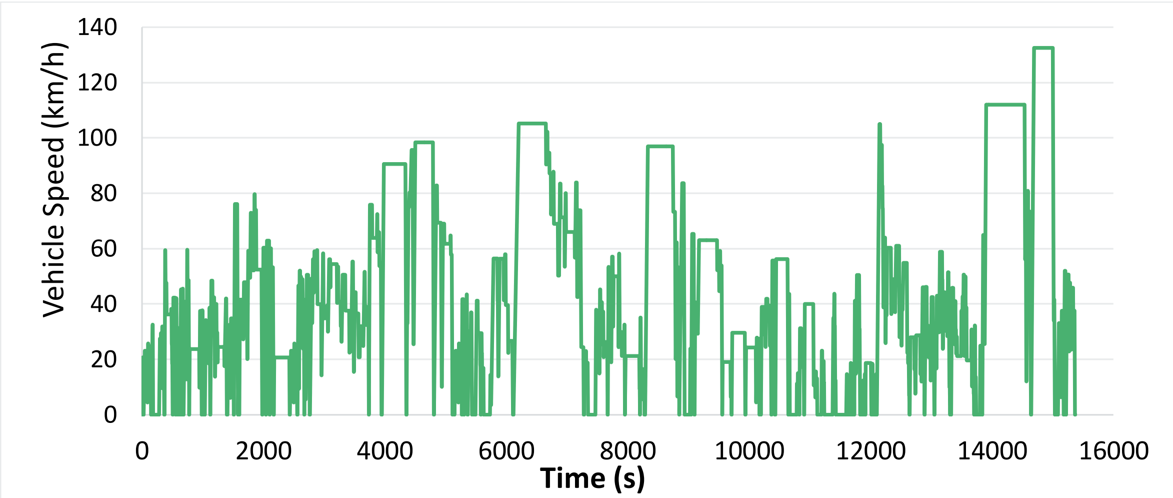

Figure 2.21: Vehicle speed profile during WLTP-brake cycle

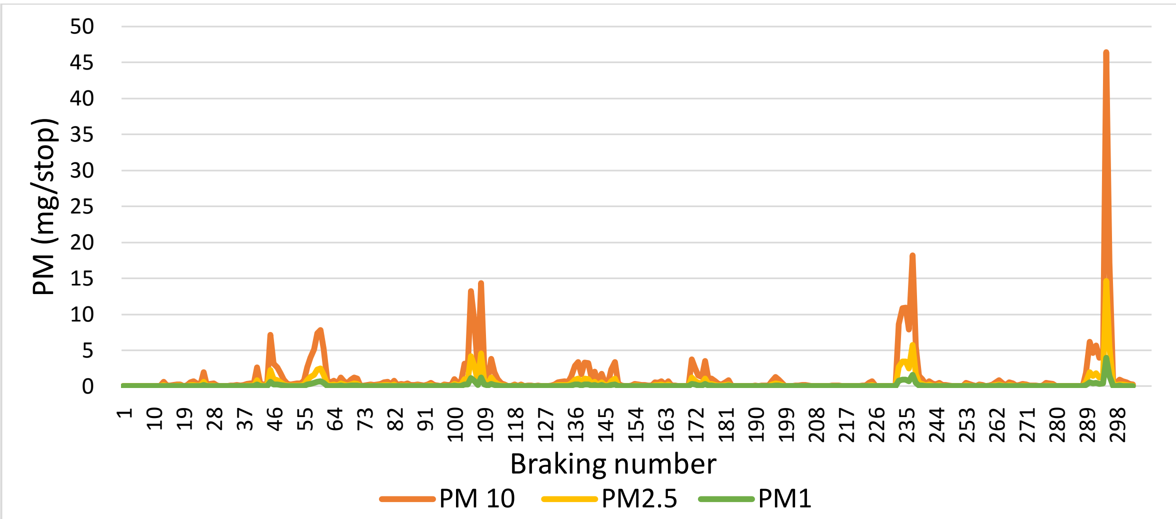

Figure 2.22: PM_{10}, $PM_{2.5}$ and PM_1 particles emitted from brake wear during WLTP-brake cycle

The average brake wear particle emissions per km, obtained by dividing the total mass of brake wear particle emissions by the length of the WLTP brake cycle, are plotted in **Error! Reference source not ound.**. The average PM_{10}, $PM_{2.5}$ and PM_1 emissions were 2.34, 0.77 and 0.20 mg/km for the left front wheel brake, respectively. Among them, the PM_{10} emission factor is three times and ten times larger than $PM_{2.5}$ and PM_1 emissions, respectively. Similar finding was reported by (Grigoratos and Martini, 2015), who evaluated several on-road tests in different environments (e.g., tunnels, street canyons, or roadside environments) to estimate brake wear emission factors for light duty vehicles (LDVs). These studies have yielded quite a range of values, from 1.0 to 8.8 mg/ km/vehicle (PM_{10}), depending on the observation site and conditions. In contrast, direct measurements using brake dynamometers with isokinetic sampling systems estimated brake wear emission factors in the range of 3.0–8.0 mg/ km/vehicle (PM_{10}) and 2.1–5.5 mg/km/vehicle ($PM_{2.5}$) (Grigoratos and Martini, 2015; Timmers and Achten, 2016). (Garg et al., 2000) pointed out that the brake wear rates correspond to vehicle emission rates of 3.4-9.0 mg/mi. On average, 86% and 63% of the airborne PM was smaller than 10 µm in diameter (PM_{10}) or 2.5 µm in diameter ($PM_{2.5}$), respectively. These results are in agreement with the current tested data.

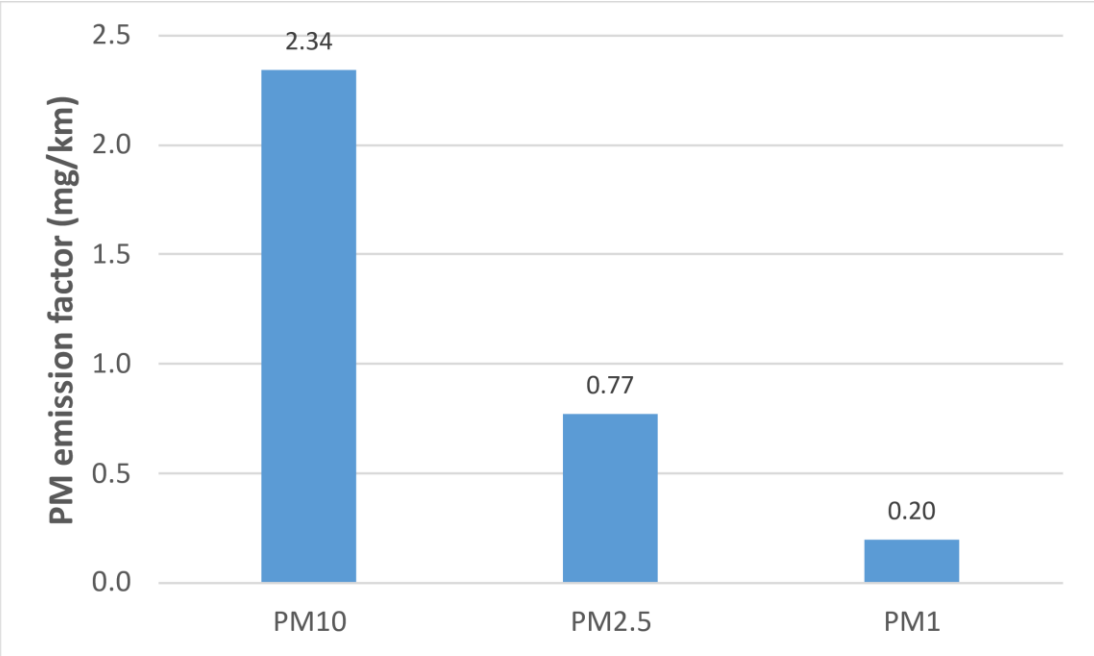

Figure 2.23: PM_{10}, $PM_{2.5}$ and PM_1 emission factors during WLTP-brake cycle

Figure 2.24 presents the PN emitted from brake wear during WLTP Brake cycle. It can be seen that PN_{10}, $PN_{2.5}$ and PN_1 present similar evolution trend during WLTP Brake cycle. Similarly, among 303 braking events, the emitted maximum PN_{10}, $PN_{2.5}$ and PN_1 appears at #295, from 132.5 km/h to 34.0 km/h with a deceleration of 1.82 and an initial and final rotor temperature of 52.3 ^oC and 150.2 ^oC. The emitted minimum PN_{10}, $PN_{2.5}$ and PN_1 appear at #219, from 12.36 km/h to 0 km/h with a deceleration of 1.14 and an initial and final rotor temperature of 53.4 ^oC and 54.0 ^oC. It is found that the maximum PM and PN emissions emit from the same brake event. In parallel, the minimum PM and PN also produce from the same brake event.

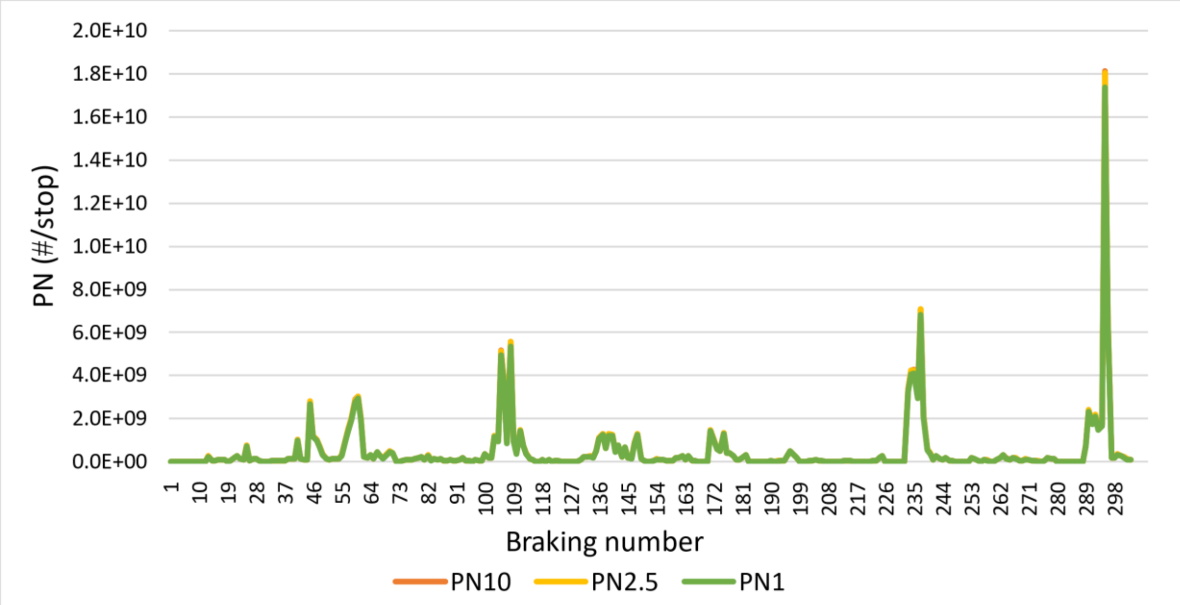

Figure 2.24: PN_{10}, $PN_{2.5}$ and PN_1 emitted from brake wear during WLTP-brake cycle

Figure 2.25 shows the average brake wear particle number per km, obtained by dividing the total particle number of brake wear by the length of the WLTP brake cycle. The average PN_{10}, $PN_{2.5}$ and PN_1 emissions were 7.42 10^8, 7.39 10^8 and 7.12 10^8 #/km for the one left front wheel brake, respectively. The PN_{10} and $PN_{2.5}$ are almost same, which are slightly larger than PN_1. Limited information is available in the literature on brake-wear PN emissions and the lack of a consistent measurement methodology makes it difficult to compare the results. (Mathissen et al., 2019) tested a mid-size passenger car on a chassis dyno by means of partly enclosing the front left wheel and sucking the generated particles through conductive tubing to a sampling plenum. The PN emissions over 3h-LACT tests were found to be 3.5 10^9 #/km/brake when thermally treated over a catalytic stripper operating at 300°C (Zum Hagen et al., 2019). (Mamakos et al., 2019) reported that the PN determined for the floating calliper and fixed calliper systems are within the range of 4.5 10^9 and 8.5 10^9 #/km/ brake, respectively. The 1.5$10^9$ #/km/brake over trip-10 was observed with a more compact brake system. These data roughly agree with the current results.

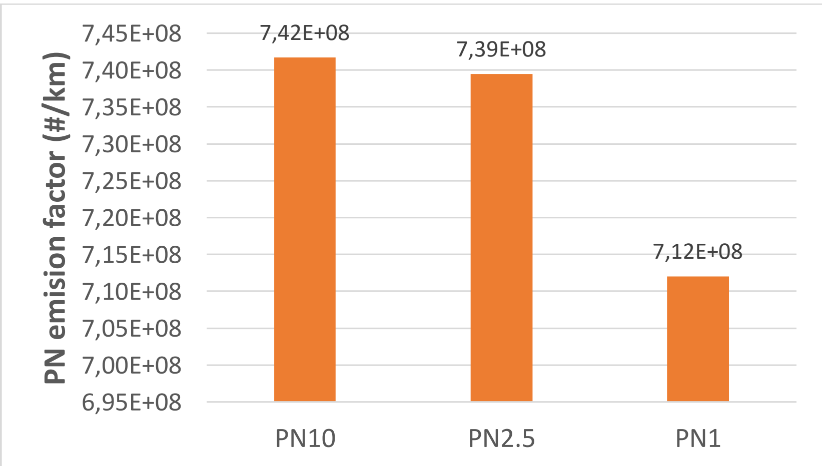

Figure 2.25: PN_{10}, $PN_{2.5}$ and PN_1 emission factors during WLTP-brake cycle

2.2.3 Comparison of PM and PN during standard and mild WLTP-brake cycles

The mild WLTP-brake cycle was developed according to the standard WLTP-brake cycle. Figure 2.26 presents the vehicle speed profiles during these two cycles. The average brake speed for reference and mild cycles are 43.7 km/h and 41 km/h, respectively. Their braking deceleration rates are in the range of 0.49−2.18 m/s^2, while the average deceleration rate is 0.82 m/s^2 for mild cycle, which is smaller than that for reference cycle of 0.97 m/s^2. Initial braking temperatures for reference and mild cycles range from 40 °C to 175 °C and from 40°C to 115 °C, respectively. However, these two cycles have the same the number of stops (303) and total distance of 192 km.

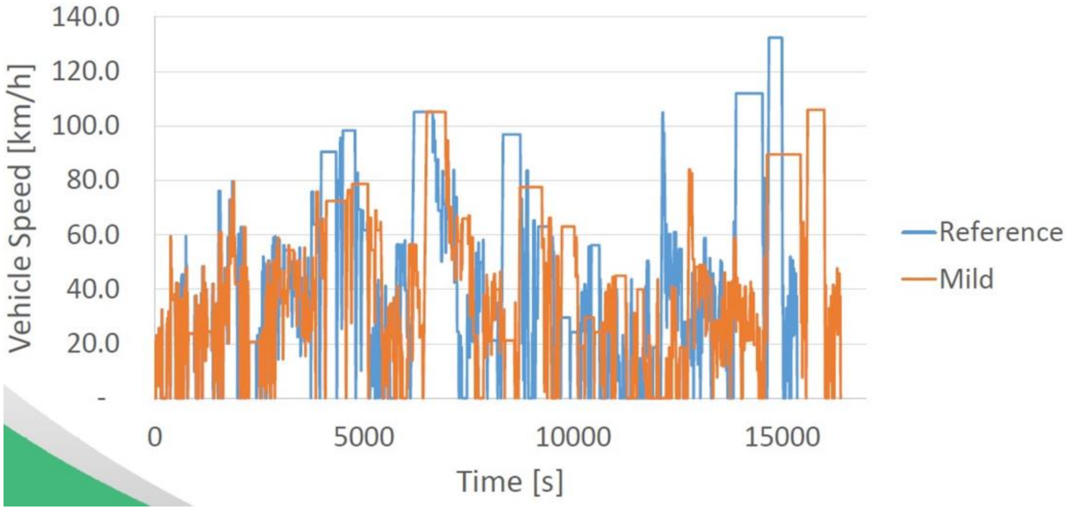

Figure 2.26: Vehicle speed profiles during standard (reference) and mild WLTP-Brake

Figure 2.27 shows PM emission factors during reference and mild WLTP-Brake. It can be seen that PM emission factors during reference WLTP-brake cycle are lower than those during mild WLTP-brake cycle. PM_{10}, $PM_{2.5}$ and PM_1 emission factors reduce 52%, 42% and 46%, respectively, thus proving that decreased average brake speed and deceleration rates can reduce significantly PM emissions.

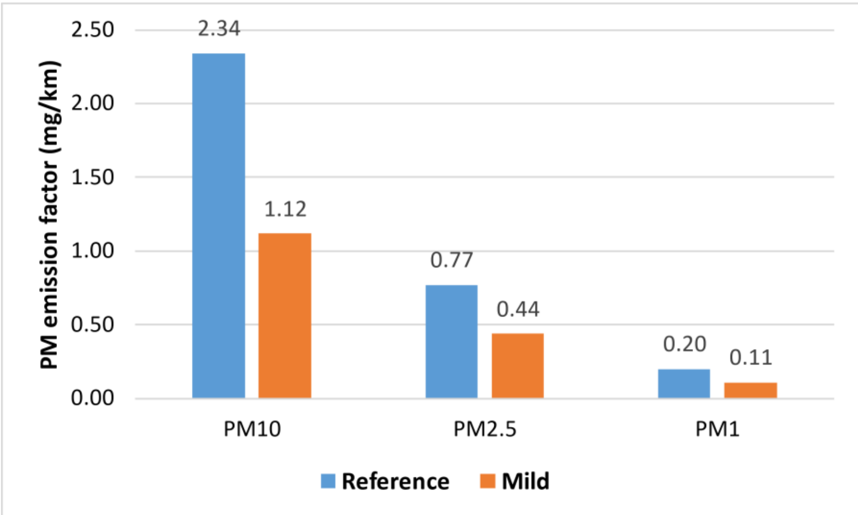

Figure 2.27: PM emission factors emitted from brake wear during reference and mild WLTP-Brake

In Figure 2.27, the PM emission factors only represent the emissions emitted from one left front brake system. Therefore, the PM emission factors emitted from all the brake systems of passenger car are approximately three times the current results. The data for reference WLTP-brake cycle are roughly consistent with the results reported in the literature. In addition, the developed mild WLTP-brake cycle is beneficial to the improvement of air quality.

Figure 2.28 depicts PN emission factors during reference and mind WLTP-Brake cycles. Similarly, the developed mild cycle can reduce significantly PN emission factors. Compared the reference cycle, the PN_{10}, $PN_{2.5}$ and PN_1 emission factors emitted from the mild WLTP-brake cycle decrease by 57%, 57% and 58 %, respectively. Such a difference in PN emission factors during these two cycle is likely to be closely related to the reduced vehicle brake temperature. Similar finding was reported by (Zum Hagen et al., 2019), who found that substantial increase in the amount of PN was associated with the increased brake temperature. (Chasapidis et al., 2018) revealed that the lower PN was generated at lower temperature. In the case of the particles with various sizes, it is observed that in Figure 2.27 and Figure 2.28, the PM emission factor is dominated by particles greater than 2.5 µm and the PN emission factor is determined together by particles smaller than 10 µm. This size-dependency of the EF values suggested that both the PN- and PM-based EFs need to be considered in order to evaluate the potential health hazards of brake emissions.

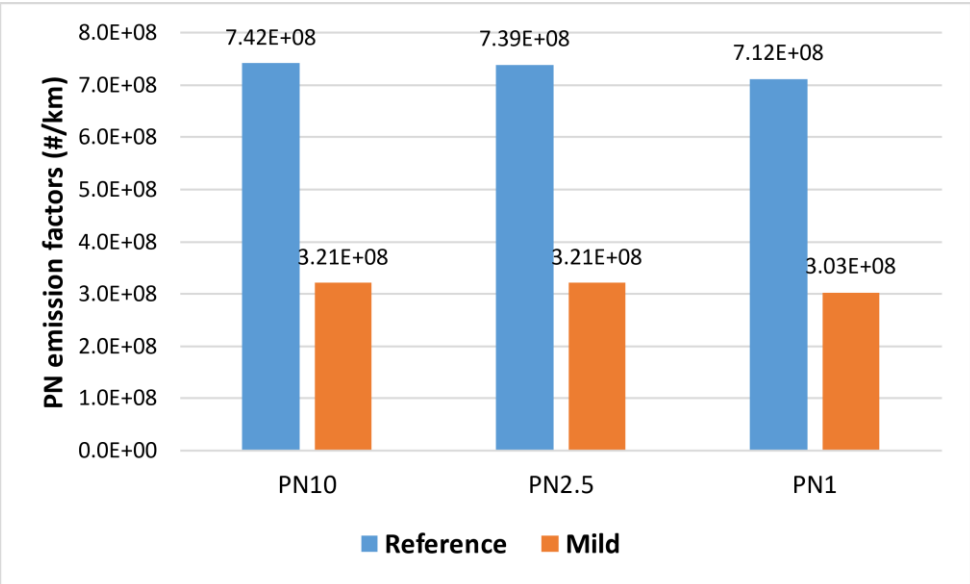

Figure 2.28: PN emission factors emitted from brake wear during reference and mild WLTP-Brake

2.3 Tyre wear emissions

This section presents the findings of a study conducted to analyse the tyre wear characteristics of a fleet of taxi cars in Italy and Greece under actual operating conditions. Tyre wear emissions, as one of important non-exhaust emissions from traffic, have been a crucial contributor to Particulate matter, with its mass contribution as high as 30% to non-exhaust emissions from traffic.

In Task 3.3, the tyre wear (in terms of mass lost in mm^3) of 76 vehicles mainly in Rome (Italy) and Athens (Greece) was measured periodically. In total, there were 553 measurements collected over several 3-month periods between September 2019 and June 2021. In addition, other parameters which may affect tyre wear were recorded as summarised in the following table.

Table 2.6: Tyre measurement parameters

Parameter	description	Example
car	car ID	E177000845
tug	tyre ID	RS607B
pos	tyre position	FL (= Front Left) RL (= Rear Left)
date_start	start date of data collection	12/05/2020
date_stop	end date of data collection	13/07/2020
vehicle_type	vehicle make and model	toyota_prius_plus
size	size of the tyre	215/50R17
comm	tyre type	T001 (= summer) LM005 (=winter) A001 (= all seasons) *etc.*
delta_km_tyre	kilo-metres done by the vehicle in the period	
mm3_lost	tyre wear in mm^3	

During each of the measurement periods, the driving behaviour parameters of the 76 vehicles were also recorded as summarised in Table 2.7.

Table 2.7: Driving behaviour parameters

Parameter	description	Example
car	car ID	E177000845
date_start	start date of data collection	12/05/2020
date_stop	end date of data collection	13/07/2020
ax_bin	longitudinal acceleration in mg-force, mg	300
ay_bin	lateral acceleration in mg-force, mg	-800
speed_bin	speed of the vehicle in km/h	120
count	frequency of a combination of ax, ay and speed	$2.13\ 10^{-6}$

2.3.1 Descriptive statistics of tyre wear measurements

In the driving behaviour dataset, there are 20 bins between -900 and 1000 mg (mg-force) for longitudinal acceleration (ax), 20 bins between -1000 and 9000 for lateral acceleration (ay), and 23 bins between 0 and 220 km/h for vehicle speed. This results in a total of 9200 bin combinations.

As tyre wear is generally proportional to the distance travelled, tyre wear per kilometre (i.e. mm^3/km) was used for comparison.

The descriptive statistics of tyre wear measurements for FL (front-left tyre) and RL (rear-left tyre) are summarised in Table 2.8 and also shown in Figure 2.29. The other tyres (i.e. front-right and rear-right) were not measured in the tyre wear campaign.

On average, front tyres worn twice as much as rear tyres for the same distance travelled. However, the maximum wear value of the rear tyres (i.e. 92.467 mm^3/km) is higher than that of the front tyres (i.e. 89.508). Both tyre positions have a number of outlier points which lie above the upper whisker line and far away from the quartiles (i.e. > Q3 + 1.5 Interquartile). It is not clear whether such outliers are genuine measurements or due to measurement errors. What is clear is that if the factors which determine these outliers are not available, many modelling methods such as regression will not perform well. This issue is addressed in the next section.

Table 2.8: Descriptive statistics of tyre wear measured on FL and RL tyres

Parameter	FL	RL
Minimum	0.766	0.000
Quartile 1	13.307	7.090
Median	22.298	11.375
Quartile 3	31.983	18.808
Maximum	89.508	92.467

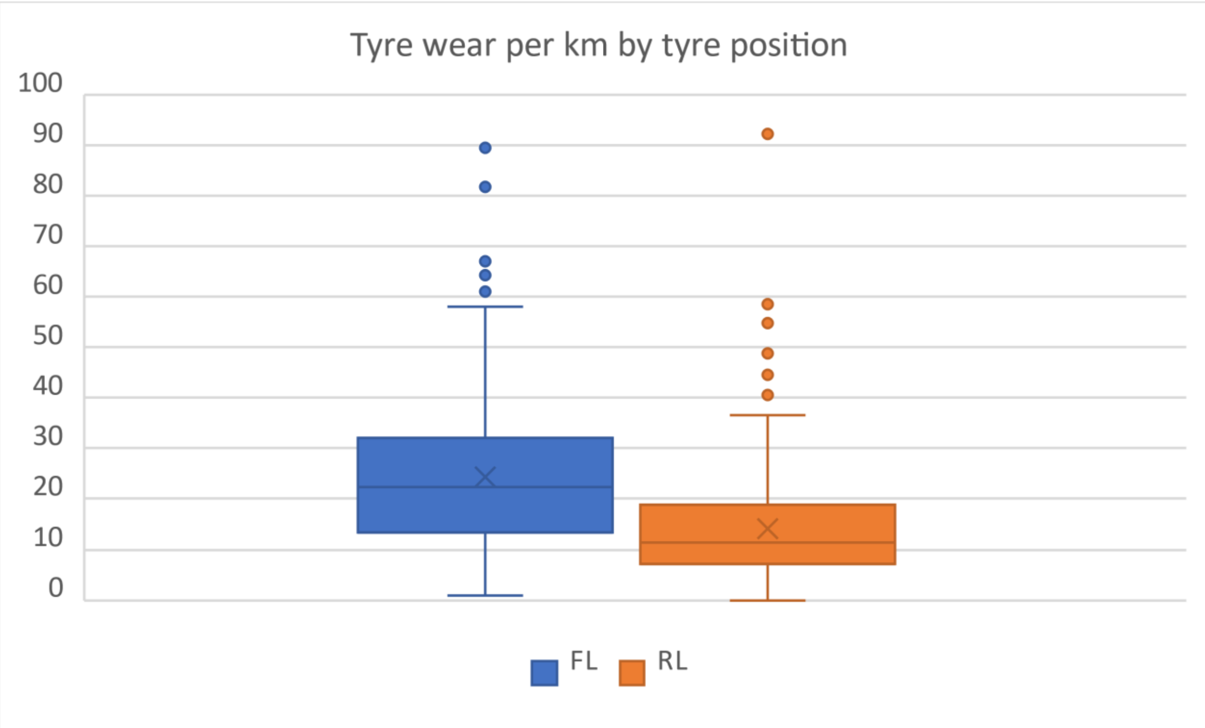

Figure 2.29: Comparison of front left (FL) and rear left (RL) tyres

There were eight types of vehicles involved in the tyre wear campaign. The descriptive statistics of their tyre wear per km are presented in Table 2.9 and also shown in Figure 2.30. The average measurements (i.e. median) vary substantially with 8.770 mg from Skoda Octavia and 26.312 mg from Ford C-Max. The lowest wear measurement (47.739 mg) was obtained from Volkswagen Passat, whereas the highest measurement (92.467 mg) was obtained from Toyota Auris. Volkswagen Passat cars are the only one without outliers.

Table 2.9: Descriptive statistics of tyre wear measured on eight vehicle types

Parameter	ford_c-max	mercedes_b	skoda_octavia	skoda_superb	toyota_auris	toyota_prius	toyota_prius_plus	volkswagen_passat
Minimum	1.573	1.091	0.128	3.794	1.940	4.810	0.000	8.674
Quartile 1	19.184	12.119	6.235	8.288	10.074	15.609	10.179	13.707
Median	26.312	18.927	8.770	11.175	13.535	21.724	17.847	26.036
Quartile 3	29.940	28.003	14.102	17.862	23.576	33.406	27.366	33.185
Maximum	61.046	81.979	67.282	54.820	92.467	67.011	89.508	47.739

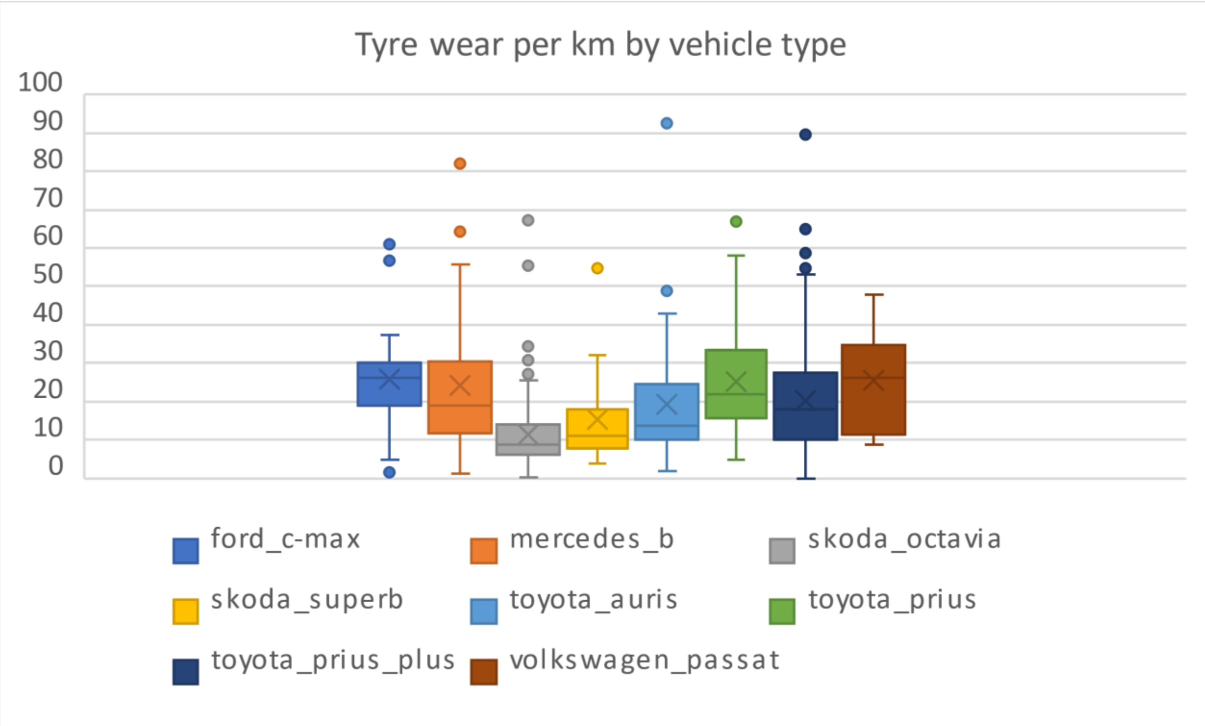

Figure 2.30: Comparison of tyre wear of eight vehicle types

With reference to how tyre wear is affected by size, tyre wear was measured on ten sizes. Their descriptive statistics are presented in Table 2.10 and also shown in Figure 2.31. Tyre size 225/45R17 has the lower average wear measurement but the highest maximum value. Size 225/45R18 has the highest average measurement and also is the only one without outliers.

Table 2.10: Descriptive statistics of tyre wear measured on ten sizes

Parameter	195/65R15	205/55R16	205/60R16	215/45R17	215/50R17	215/55R16	215/55R17	215/60R16	225/45R17	225/45R18
Minimum	1.940	0.128	0.000	4.810	2.243	1.573	4.233	3.794	3.516	5.766
Quartile 1	9.841	6.969	11.171	15.342	9.963	21.051	10.530	8.288	7.276	17.824
Median	12.953	11.625	18.792	20.803	19.165	26.116	18.565	11.175	9.131	32.507
Quartile 3	19.494	19.794	29.152	29.374	23.498	30.415	26.331	21.562	16.667	45.232
Maximum	52.878	64.302	89.508	58.175	58.567	61.046	47.739	54.820	92.467	81.979

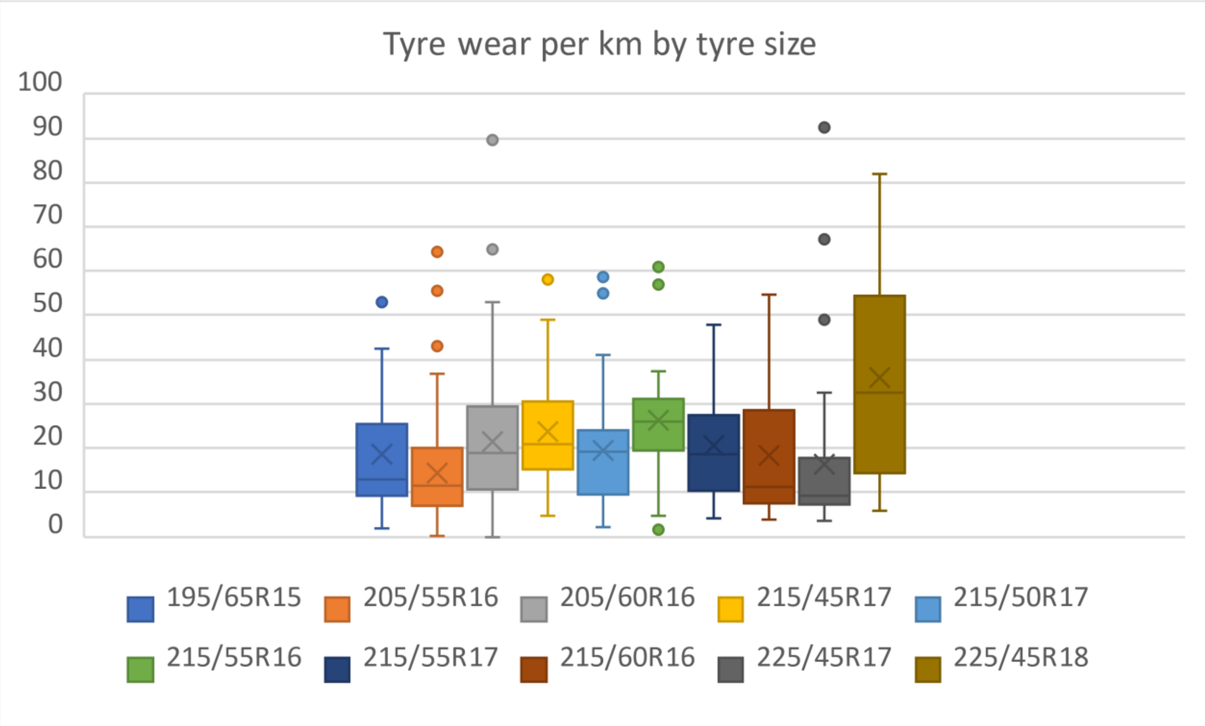

Figure 2.31: Comparison of tyre wear between ten sizes

Finally, the collected tyre wear measurements allow the analysis of tyre types to be carried out as shown in Table 2.11 and in Figure 2.32. The lowest average and maximum wear measurements per km were obtained from the Turanza T001 tyre which is Bridgestone's flagship summer tyre of the touring range fitted to passenger cars. As the company states, it combines great safety, comfort, durability and environmental performance, and to deliver a superior quality. The highest average measurement was collected on a Bridgestone Blizzak LM005 winter tyre. The highest maximum wear was measured on Bridgestone A005, a premium touring All season tyre with directional tread pattern. The Michelin CrossClimate tyre has the smallest range (between maximum and minimum) of 29.291 mg per km and is the only one without outlier measurements.

Table 2.11: Descriptive statistics of six tyre types

Parameter	A005	ALLSEASONCONTACT	CROSS_CLIMATE	LM005	T001	T005
Minimum	0.957	3.453	10.179	16.788	0.274	0.000
Quartile 1	13.882	21.470	12.839	21.746	4.415	6.514
Median	21.249	23.973	18.462	28.074	7.695	9.866
Quartile 3	31.849	29.596	23.926	46.046	12.257	15.282
Maximum	92.467	53.020	39.470	49.621	36.889	67.282

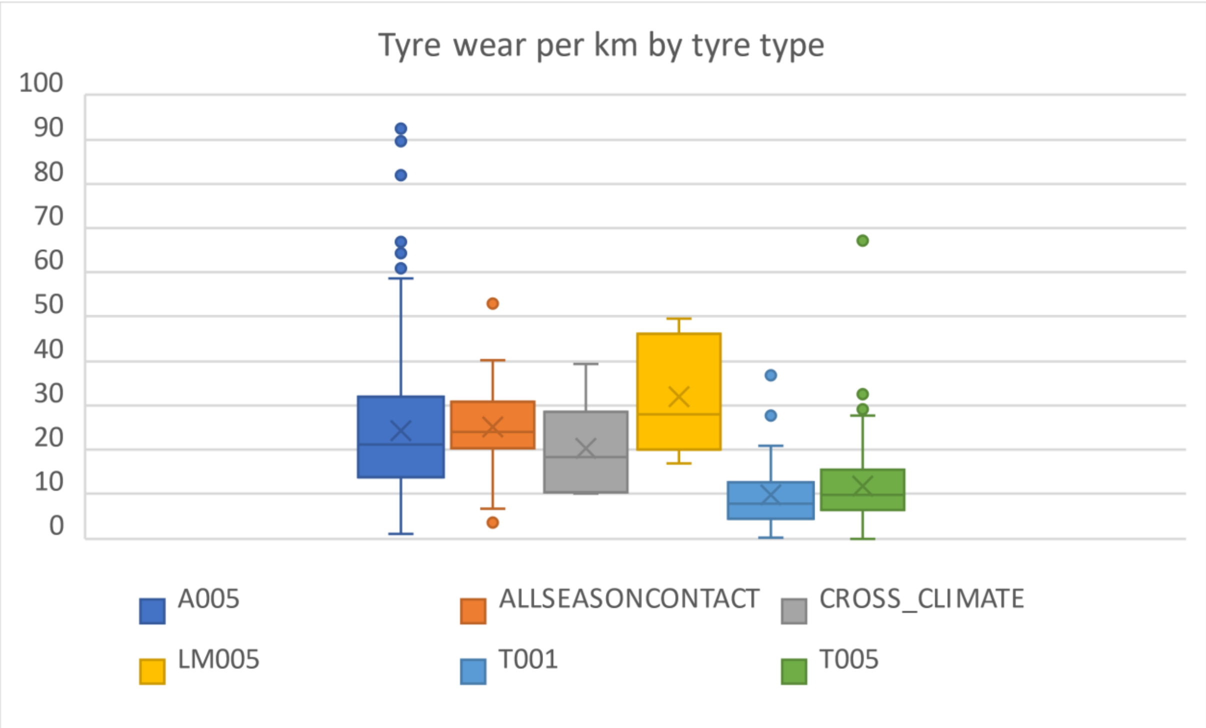

Figure 2.32: Comparison of tyre wear between six types

To conclude, the tyre wear measurements (i.e. mm^3/km) collected in this project vary substantially between tyre positions, vehicle types, tyre sizes as well as tyre types, with a considerable number of outliers. It is not clear whether this variability is acceptable and genuine due to different local road and environment conditions, or is a result of measurement errors. It is envisaged that if the important driving behaviours which result in outlier measurements are not available, many predictive models may not perform well. The link between tyre wear and driving behaviour is quantified in the next section.

2.3.2 Simple regression models for tyre wear prediction

Modelling started by taking as few driving behaviour parameters as possible. A simple linear regression model for tyre wear prediction as originally proposed in MODALES, was defined to take the average values of longitudinal accelerations (*ax*), lateral accelerations (*ay*) and vehicle speeds (*speed*) as independent variables as expressed below.

$$Tire\ Wear = \alpha * ax + \beta * ay + \gamma * speed + cons \qquad \text{(Eq. 2-1)}$$

It is noted that these accelerations and speeds are not actual values and instead they are categorised into bins such as 10, 20 and so on for speed. This may be a reason which leads to poor model performance. As accelerations can be positive and negative, both cause the tyre to wear, their average (i.e. mean) values were calculated without the signs in this simplest model. The separate effects of acceleration and deceleration on tyre wear are modelled in the second regression model. The calibration result of the above model is summarised in Table 2.12.

Table 2.12: A simple regression model using mean values of ax, ay and speed

Coefficient	Value	Variable
α	-0.369	average ax
β	0.783	average ay
γ	-0.007	average speed
cons	11.479	constant
R^2	**0.099**	**R square**

As can be seen in Table 2.12, the R square value is as low as less than 0.1, indicating that the average values of longitudinal and lateral accelerations as well as vehicle speed cannot explain the variability of tyre wear measurements as discussed earlier. Such poor correlation is also illustrated in Figure 2.33 in which it is clear that the simple linear regression model can only represent the average of the real tyre wear measurements.

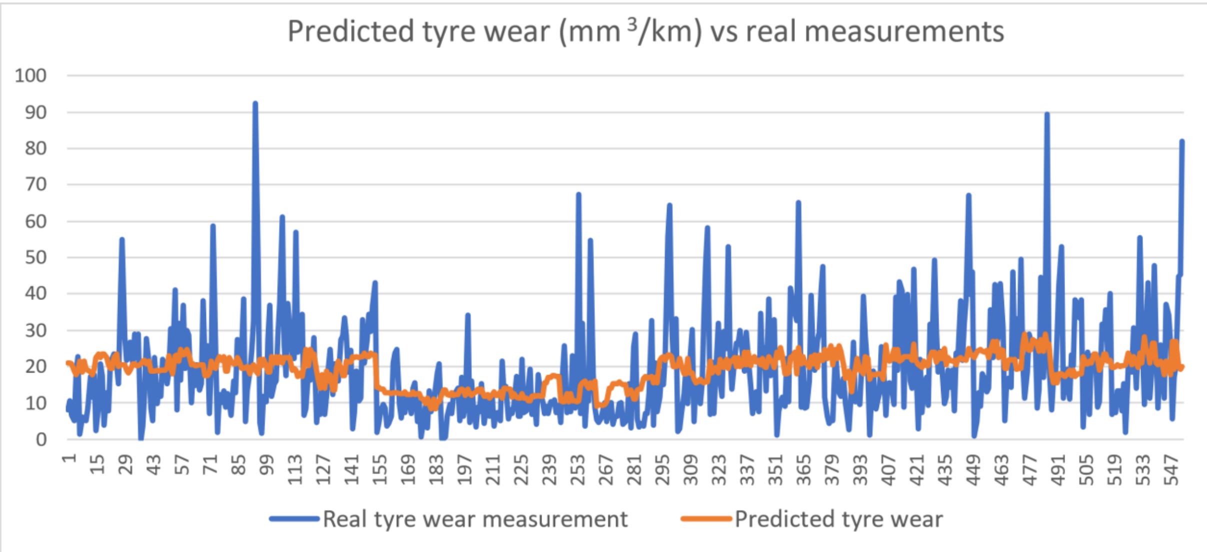

Figure 2.33: Comparison of predicted and real tyre wear

Another simple linear regression model was also tested using acceleration and deceleration separately as shown below.

$$Tire\ Wear = \alpha 1 * (-ax) + \alpha 2 * (+ax) + \beta 1 * (-ay) + \beta 2 * (+ay) + \gamma * speed + cons \quad \text{(Eq. 2-2)}$$

The model calibration result is shown in Table 2.13. As can be seen, the R square value of the second model is slightly higher than that of the first model, but it is still pretty low (just above 0.1), indicating poor prediction of tyre wear from average values of ax, ay and speed.

Table 2.13: A simple regression model using positive and negative accelerations

Coefficient	Value	Variable
α1	0.125	negative average ax
α2	-0.878	positive average ax
β1	0.926	negative average ay
β2	0.624	positive average ay
γ	-0.024	average speed
cons	13.780	constant
R^2	**0.102**	**R square**

To conclude, the average values of the three driving behaviour parameters (i.e. ax, ay and speed) produce poor prediction of tyre wear measurements which exhibit a high degree of variability and asymmetry. This implies that other statistical measures such as skewness and kurtosis should be included as independent variables in the regression model for tyre wear prediction as they represent the degree of the asymmetry and peakedness of the distribution of the tyre wear measurements. To address the effect of the skewness, a non-linear modelling method (i.e. XGBoost) is developed, as presented in the following section.

2.3.3 The XGBoost model

The effect of driving behaviour can be quantified by measuring the tyre wear rate of the vehicle driven by different drivers. The variation in wear rates is very significant (Le Maitre et al., 1998). In this study, the driving behaviour is estimated from longitudinal and lateral accelerations and speed of the vehicle. Its evolution is given by a lognormal (Ax), lateral (Ay), and speed distributions. The four featured parameters of the distributions, including mean value, standard deviation (std), skew and kurtosis (kurt), represent the driving behaviour of each driver.

Figure 2.34 shows that the correlation coefficient of featured parameters. It can be observed that correlation coefficients between mean value and std as well as skew and kurt are 1. It means that they present linear dependence, so seven featured parameters, including Ax mean, Ax skew, Ay mean, Ay skew, speed mean, speed skew, driving distance were chosen to serve as independent variables. Tyre wear rates was chosen as a dependent variable.

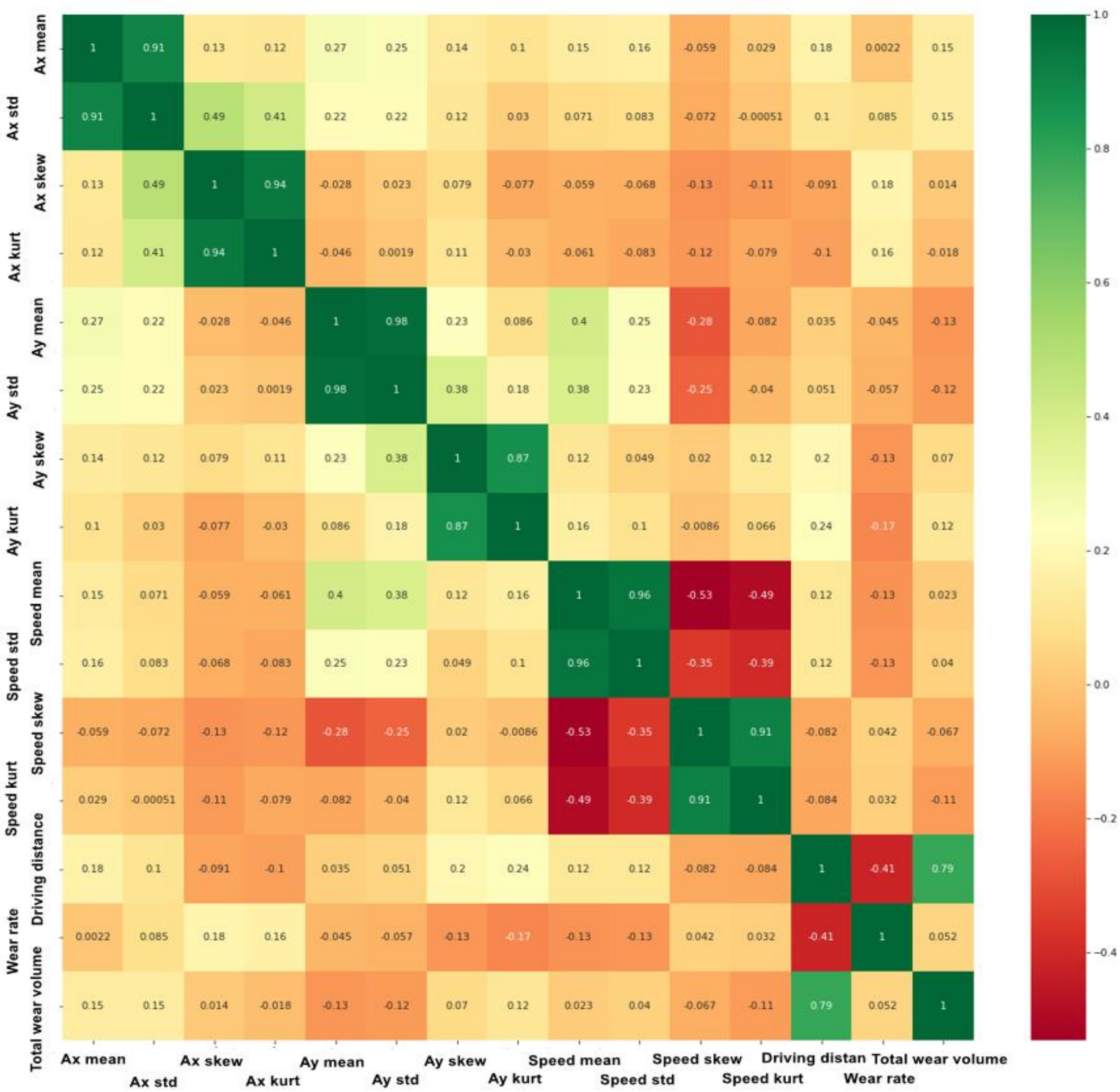

Figure 2.34: Correlation coefficient among featured parameters in the XGBoost model for tyre wear rate

Non-linear fitting method, XGBoost was used to evaluate the relative importance of featured parameters affecting tyre wear rates. XGBoost is a highly effective and widely used machine learning method, including classification, regression, and ranking tasks (Chen and Guestrin, 2016; Mitchell and Frank, 2017; Pan, 2018). Figure 2.35 shows the decision tree ensemble, illustrating how this score can be calculated. The obtained predicted and tested results are shown in Figure 2.36. It can be seen that the predicted data basically present similar evolution trend with tested results. To evaluate the strength of the relationship between these variables, the correlation coefficient, R^2, was calculated by means of simple regression to assess. The ***R^2 value is 0.846*** between the predicted values using XGBoost method and tested values from partners, indicating that proposed XGBoost method seems to promising to predict tyre wear rates of vehicle under actual operating conditions.

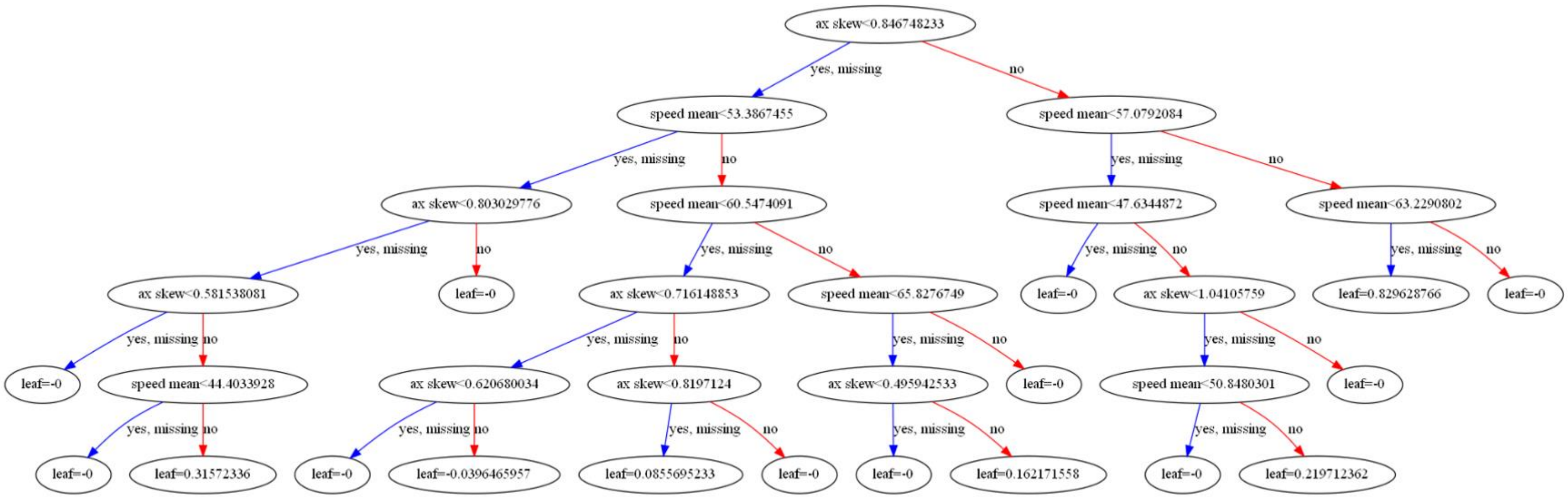

Figure 2.35: Decision tree ensemble for the XGBoost model for tyre wear rate

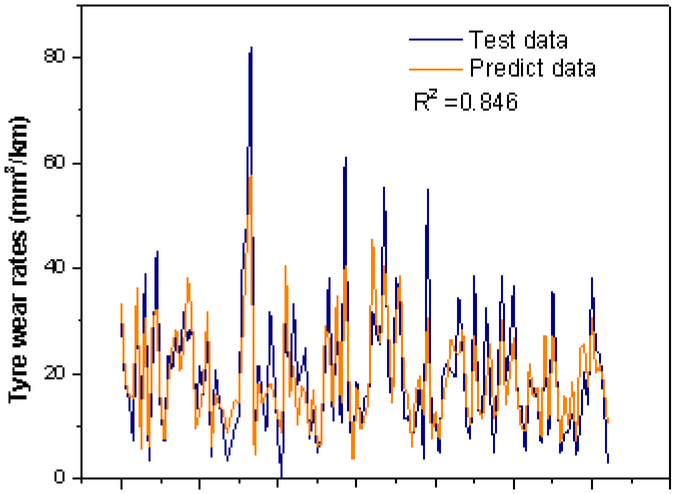

Figure 2.36: Predicted and tested values of tyre wear rates

The outcome of executing the XGBoost is shown in Figure 2.37. We can obtain the results as to which attribute contribute the most towards achieving the result. In short, the feature importance can be found out. From the feature importance plot, it can clearly be seen that *Ax skew* is the most important feature which has contributed towards the prediction of the results. It means that harsh braking and acceleration would lead to a steep increase in tyre wear rate. This is followed by Ay mean, driving distance, speed mean, Ax mean and speed skew. The least important feature is *Ay skew*.

In a study by (Lee et al., 2020), they found that the emission factor of tyre wear particles grown in order of rural area, highway, and urban area. They ascribed this appearance to the higher rates of sudden braking and rapid acceleration of motor vehicles in the urban area. (Beji et al., 2020) discovered a strong increase in emissions at higher speeds and during the most intense accelerations. In addition, they revealed that tyre wear emissions increased significantly with both braking intensity and speed at the start of braking. (Le Maitre et al., 1998) found that tyre wear rates were significantly different between the vehicles driven by professional drivers and moderate use drivers. They ascribed this behaviour to the difference of acceleration level since a professional driver will drive the vehicle at the speed limit with transversal acceleration levels much higher than those of moderate drivers. These data provide the further evidence of the results obtained in the current study.

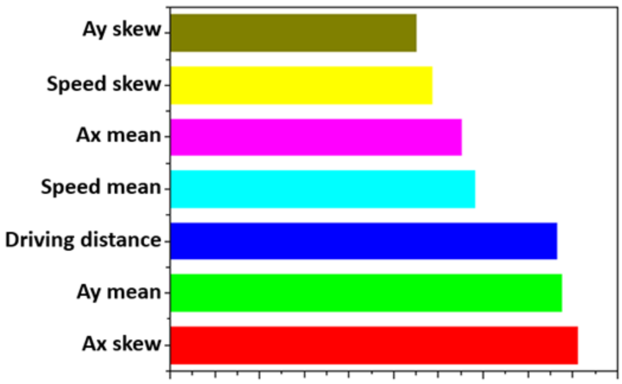

Figure 2.37: Relative importance of featured parameters affecting tyre wear rate

3 Simulation and modelling of exhaust emissions

In this chapter, a passenger car model was setup; additionally, the vehicle model was validated using experimental data; further, the relationships between driving behaviour and pipe-out emissions were analysed; finally, the mathematical emission models were setup based on the simulation results.

3.1 GT-SUITE vehicle modelling

3.1.1 Detailed modelling of the GT-SUITE vehicles

Specifications of the diesel passenger car which was used in this investigation are shown in Table 3.1. This type of car is on the market and is under an emission level of Euro 6. In order to meet stricter emission regulations (such as Euro 7 and real driving emissions), more effective after-treatment devices are necessary to limit the exhaust emissions of cars based on the current technologies. The mass of this car was around 1505 kg. The power of this vehicle was a four-cylinder, four-stroke, turbocharged diesel engine with a maximum power and torque output of 103 kW and 325 N·m respectively. The investigation was based on the simulation model which was conducted using GT-SUITE software. The simulation model is shown in Figure 3.1. This model included powertrain model, emission sources, and after-treatment devices. The powertrain model consisted of a diesel engine, transmission systems, and vehicle body. This engine model was based on the engine maps (brake specific fuel consumption determined by engine speed and torque), and the engine maps were presented in the authors' previous work (Gao et al., 2019a). The after-treatment systems included diesel oxidation catalyst (DOC), diesel particulate filter (DPF), and SCR. This investigation only focused on NO_x, consequently different NO_x reduction after-treatment devices were adopted. The performance of both after-treatment devices were compared with previous work (Gao et al., 2019b) where eHC was used to achieve catalyst fast light-off for decreasing powertrain emissions including hydrocarbon (HC), carbon monoxides (CO), and NO_x.

Table 3.1: Specifications of the diesel passenger car used for modelling in GT-SUITE

Specifications	Value
Vehicle mass	1505 kg
Maximum speed	170 km·h^{-1}
Gear number	6
Fuel	Diesel
Engine type	In-line, four-cylinder, four-stroke
Intake type	Turbocharged intercooler
Fuel injection type	Direct injection
Engine max power/ kW	103 kW @ 4000 rpm
Engine max torque/ N·m	325 N·m @ 1500 rpm
Stroke/ mm	80.4
Bore/ mm	79.1
Compression ratio	16.5
Emission regulation	Euro 6

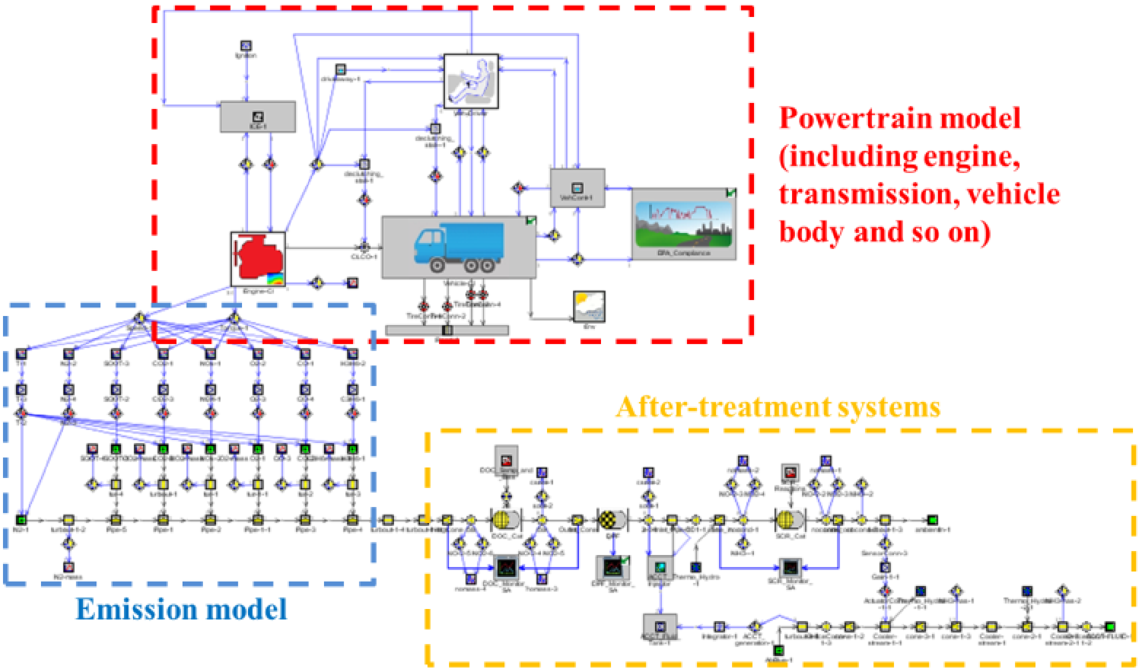

Model of the diesel passenger car

Figure 3.1: Simulation model of the diesel passenger car equipped with after-treatment systems

Figure 3.2 shows the Brake-specific fuel consumption (BSFC) map, which was obtained from the test data of the engine test bench. The minimum BSFC was ~225 $g/(kW{\cdot}h)^{-1}$, being in the range of 1500 RPM ~ 2500 RPM, and high engine loads. The engine operation points in WLTC were mainly located at the low engine load regions, which would cause low brake thermal efficiency in the engine level. Under the conditions of the same engine power output, shifts of the engine operation points to lower engine speed and higher engine load would result in lower fuel consumptions. However, the movements of the engine operation points were constrained by the vehicle conditions, e.g. the transmission system, vehicle velocity, road grade and cargo mass.

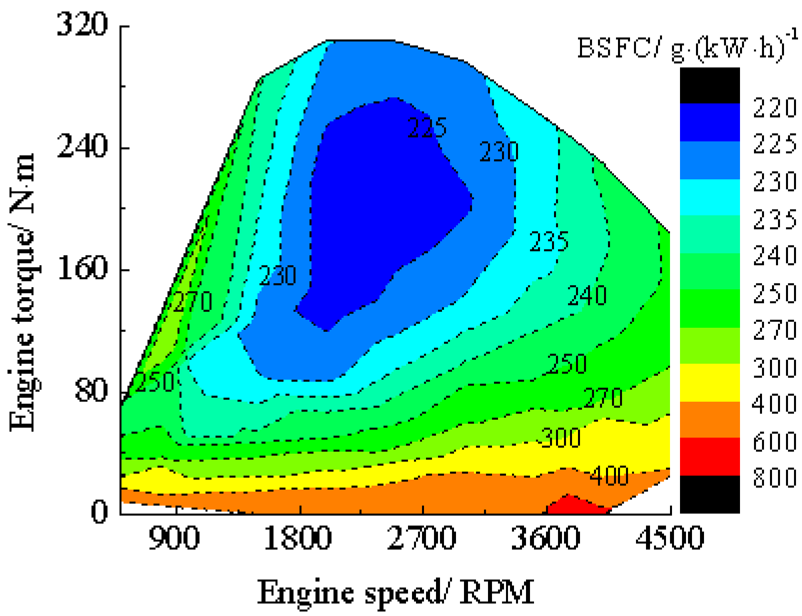

Figure 3.2: Brake-specific fuel consumption map

Figure 3.3 shows the maps of NO_x emissions. The emissions were greatly dependent on the engine operation conditions, and the maximum emission concentration was thousands of times higher than the minimum value. The optimal engine points were under the low engine speed and load conditions for NO_x and soot emissions. There should be some balance among the emissions in eco-driving. The NO_x emission is still a huge challenge to meet stricter emission regulations, so that more attention should be focused on NO_x.

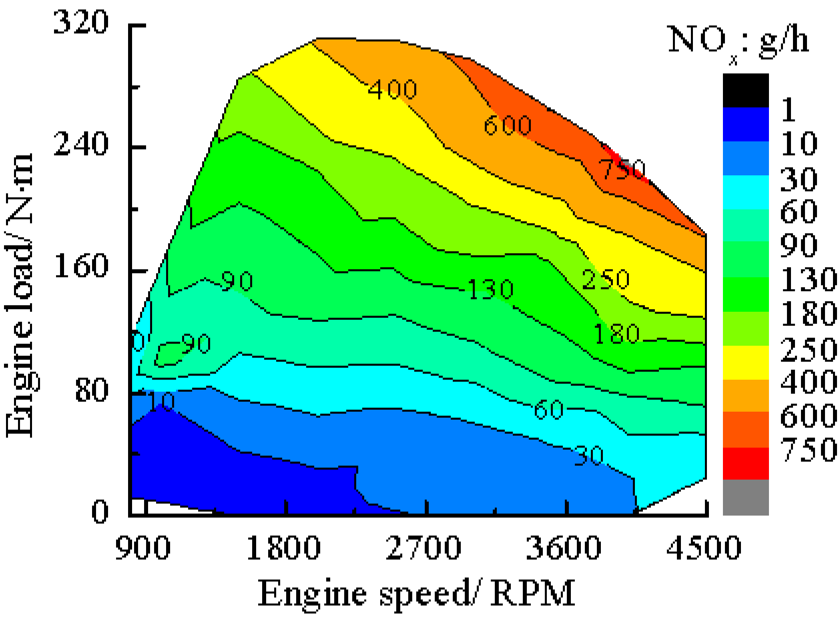

Figure 3.3: NO_x emission map

3.1.2 Validations of simulation models

Worldwide harmonized Light vehicles Test Cycle (WLTC) represents average driving characteristics around the world (Tutuianu et al., 2015), so it was selected in this chapter (Tutuianu et al., 2015). Compared with New European Driving Cycle (NEDC), WLTC covers a broader range of acceleration, and includes typical speed patterns for four different types of roads (Giakoumis and Zachiotis, 2017). This vehicle was tested in the lab based on WLTC. Meanwhile, fuel consumption rates and powertrain emission rates were monitored. Fuel consumption rates from both experiment and simulation model are shown in Figure 3.4(a). As can be seen, fuel consumption rates from simulation matched well with experimental results.

Figure 3.4(b) presents NO_x emissions from engine-out. Since the fuel consumption rates and NO_x emissions (engine-out) were low under low vehicle speed conditions, the errors of the test results over low speed were higher than that of higher vehicle speed. When considering the contributions of the engine-out NO_x emissions to the total emissions, the errors were negligible. In the engine cold start process, the coolant temperature which affected the thermal status of cylinder walls increased gradually. In this simulation, the emission sources were based on emission maps which were obtained after the engine warmed up.

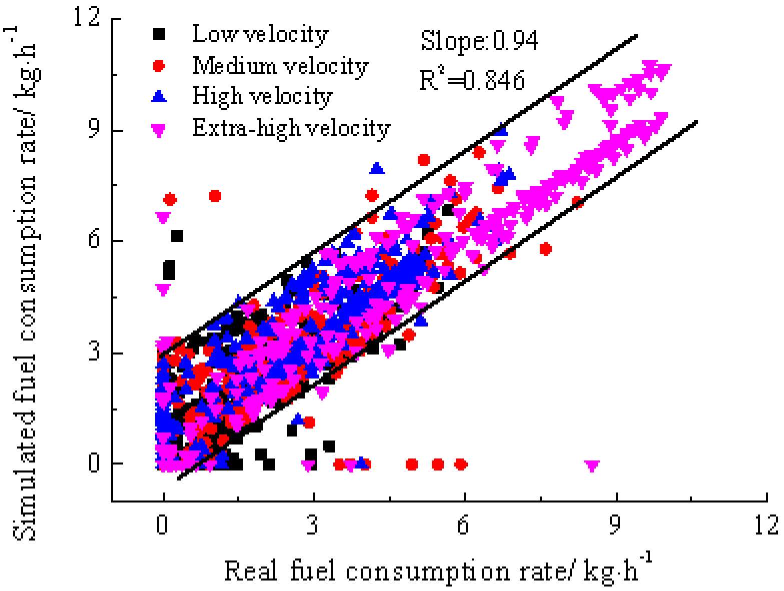

(a) Validation of fuel consumption

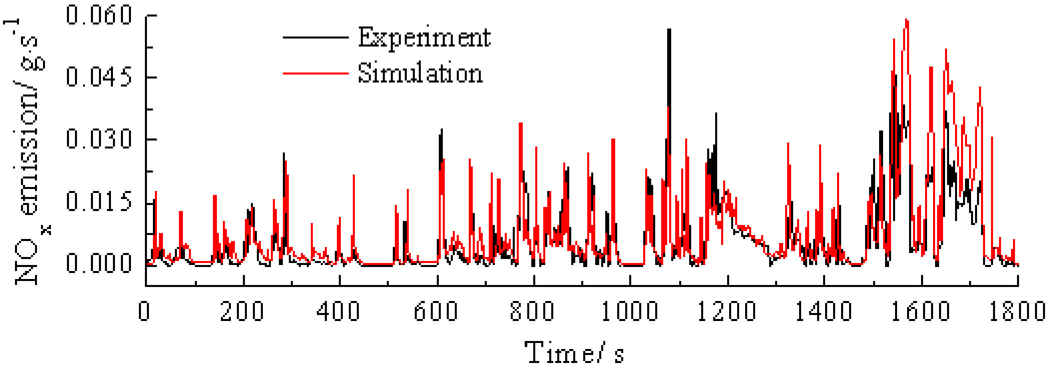

(b) Validations of engine-out NO_x emissions

Figure 3.4: Validation of the vehicle fuel consumption and NO_x emissions

3.2 Driving behaviour analysis over WLTC

Speed distributions by travel durations and distance are shown in Figure 3.5 based on WLTC which included four categories of vehicle speed (see the previous work for speed profile (Gao et al., 2019a)). In terms of the driving durations, low vehicle speed (lower than 5 km/h) accounted for the highest percentage in WLTC. Low vehicle speed usually resulted in high fuel consumption and powertrain emission factors (mass per unit distance). Generally, the durations of individual vehicle speed range dropped with speed increase over WLTC. For the travel distance based on WLTC, the majority of the distance was contributed by medium and high vehicle speed ranges. Acceleration distributions by travel durations and distance over WLTC are shown in Figure 3.6. Acceleration showed normal distributions by both travel durations and distance, with the median value being around zero. Vehicle acceleration range of -0.7 m/s^2~ 0.7 m/s^2 accounted for more than 90% of the travel durations and distance.

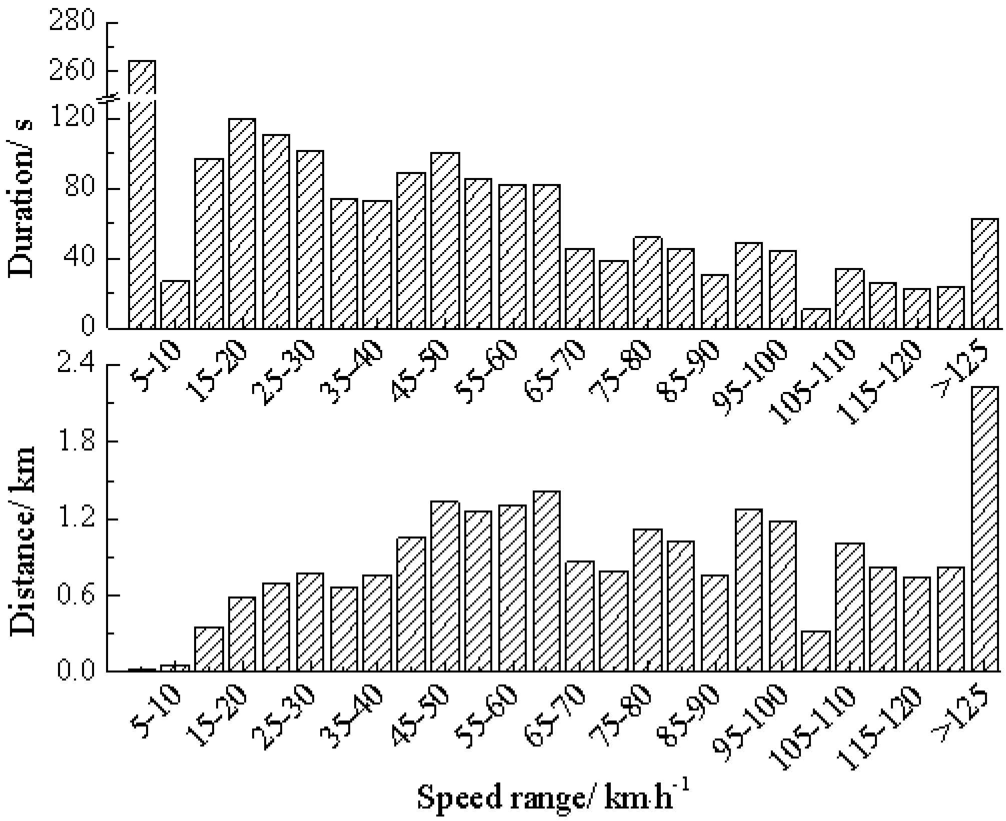

Figure 3.5: Speed distributions by travel durations and distance

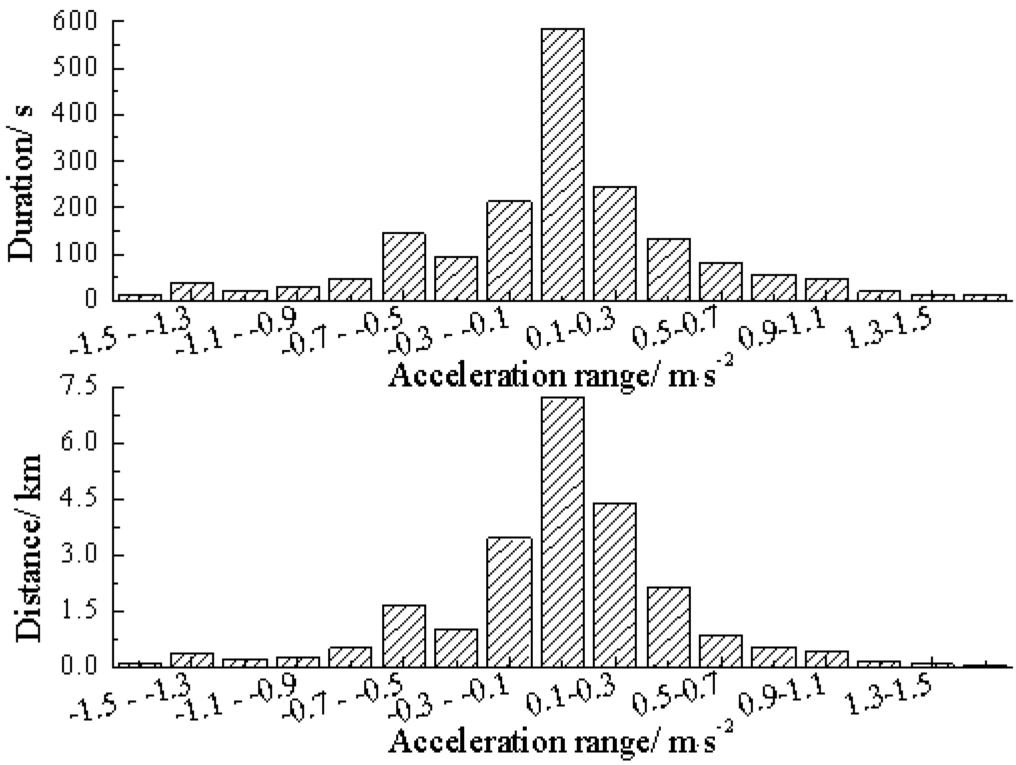

Figure 3.6: Acceleration distributions by travel durations and distance

3.3 Relationship between driving behaviours and fuel consumption

Figure 3.7 shows the fuel consumption rates in WLTC. The fuel consumption rate was dominated by the vehicle speed and acceleration. Huge fuel consumption rate was observed in the extra-high vehicle speed zone, where huge aerodynamic drag caused the decrease of brake thermal efficiency. Ma et. al (Ma et al., 2015) investigated the fuel consumptions under different driving styles, that the fuel consumption in the acceleration process accounted for 56.5% of the overall fuel consumption, and the value in deceleration process was less than 5.7%. The vehicle was recommended to avoid frequent acceleration and deceleration, and to operate at medium-high vehicle velocity conditions in eco-driving, which could be achieved by predicting the traffic conditions (Kamal et al., 2010), training the drivers (Rutty et al., 2013) and choosing the routes (Alam and McNabola, 2014). Additionally, the fuel consumption was at a medium level around 1300 s, caused by small vehicle acceleration despite of high vehicle velocity. The cold start and warm up process were taken into consideration in WLTC, which lowered the fuel economy of the vehicle. Reference (Andrews et al., 2007) indicated that the fuel consumption factor decreased by ~8% and ~14% if the lubricating oil temperature increased by 4 °C and 10 °C, respectively, in the first 6 minutes from cold start. In addition, the fuel economy improvement could reach ~7% during a 22°C cold start if following NEDC, as indicated by Will et. al (Will and Boretti, 2011). The poor fuel economy was mainly caused by the poor in-cylinder combustion, much heat loss and high viscosity of lubricating oil. For the daily short distance journey, the warm up process accounted for a huge percentage of the whole duration, where the fuel economy had huge space for improvement.

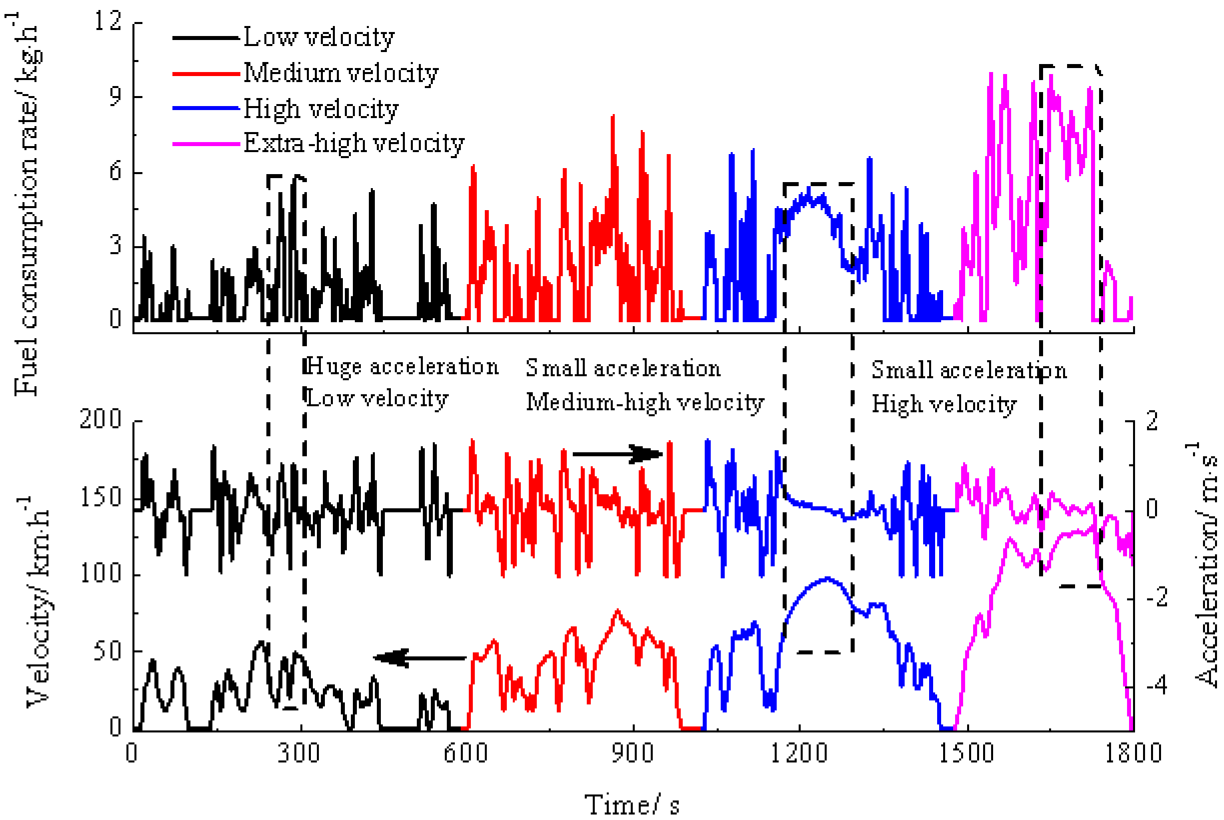

Figure 3.7: Fuel consumption rates in WLTC

Accumulated fuel consumption over various vehicle speed ranges is shown in Figure 3.8(a). As can be seen, the accumulated fuel consumption was approximately 0.02 kg for the speed range of 0 km/h~ 5 km/h although its corresponding travel distance was almost zero. Low-medium vehicle speed accounted for a large proportion of accumulated fuel consumption. Fuel consumption rates per unit distance over various vehicle speed ranges are shown in Figure 3.8(b). Fuel consumption rates for the speed range of 0 km/h~ 5 km/h were approximately 95 kg·(100 km)$^{-1}$, which was mainly caused by frequent idling stages where the fuel consumption per distance was the highest.

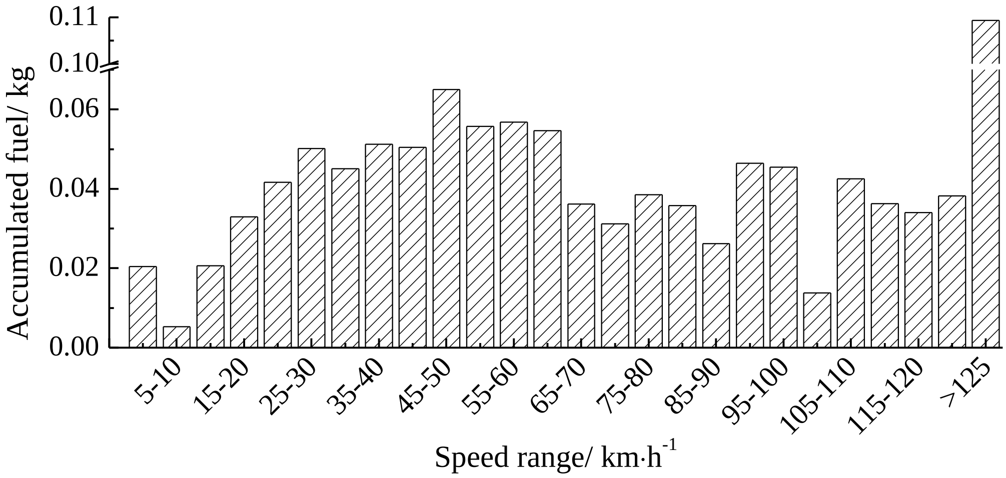

(a) Distributions of fuel consumption over various speed ranges

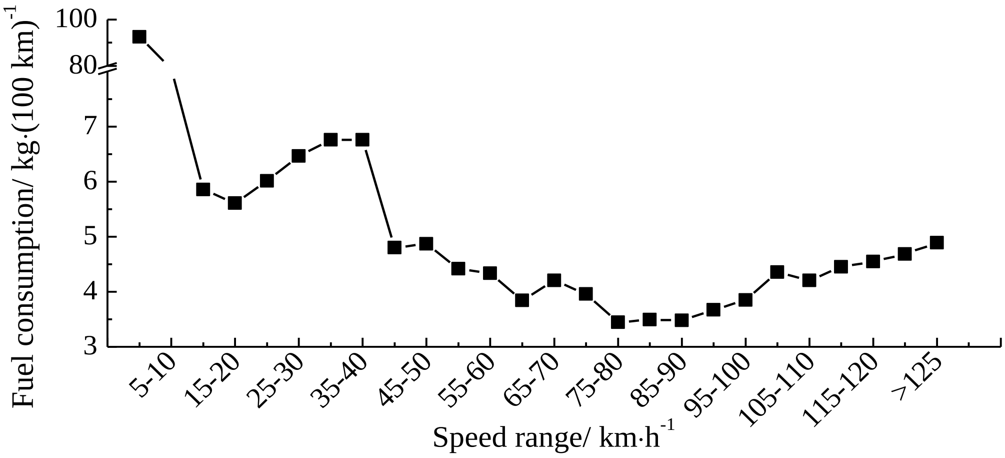

(b) Average fuel consumption rates over various speed ranges

Figure 3.8: Fuel consumption distributions and average fuel consumption rates over speed ranges

Accumulated fuel consumption over various acceleration ranges was different from acceleration distributions by durations and distance, as shown in Figure 3.9(a). The accumulated fuel consumption was almost zero when vehicle acceleration was lower than -0.3 m/s^2, which was caused by the fuel cut-off technology over aggressive deceleration events. Most of the fuel was consumed over the acceleration range of -0.3 m/s^2~ 1.5 m/s^2. Figure 3.9(b) presents the fuel consumption rates per unit distance over various acceleration ranges. It showed that the fuel consumption rates almost linearly increased with acceleration when the acceleration was higher than -0.5 m/s^2. During the real-world driving, gentle driving was suggested to drop the fuel consumption rates by decreasing the frequent acceleration. The explorations of the relationships between fuel consumption and driving behaviours would provide the evidence to drivers on the eco-driving patterns. It helped to decrease the fuel consumption and CO_2 emissions to achieve the cleaner travelling.

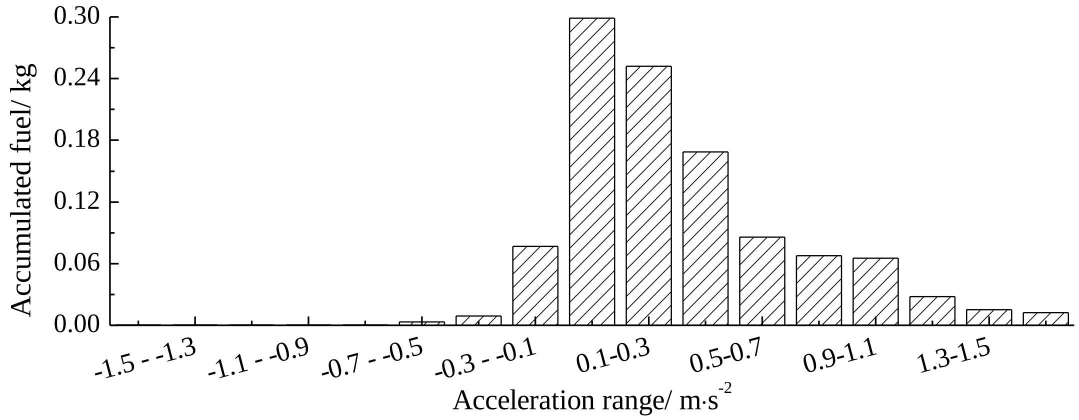

(a) Distributions of fuel consumption over various acceleration ranges

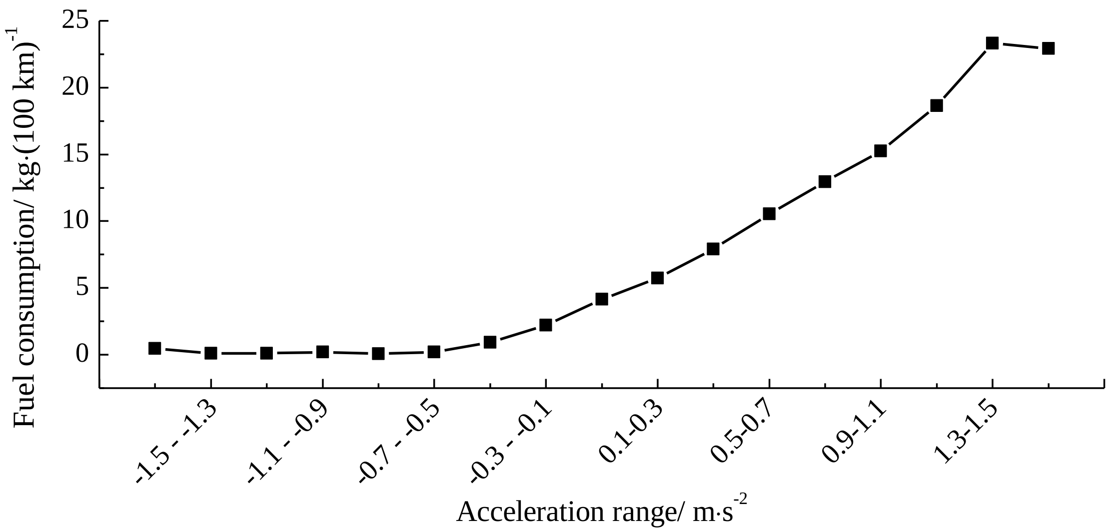

(b) Average fuel consumption rates over various acceleration ranges

Figure 3.9: Fuel consumption distributions and average fuel consumption over acceleration ranges

3.4 Relationships between vehicle speed and acceleration and engine-out NO_x emissions

Engine-out accumulated NO_x emissions are shown in Figure 3.10(a). As can be seen, vehicle speed range of 0 m/h~ 15 km/h contributed a small proportion to the total NO_x emissions compared to other speed ranges due to the short travel distance (see Figure 3.5).

It is clearly shown that medium speed range and extra-high speed range contributed the most accumulated NO_x emissions because of long travel distance over such speed ranges. Speed range of 75~100 km/h generated medium level of accumulated NO_x emissions, resulting from the low emission factors (see Figure 3.10(b)). NO_x emission factors were the lowest in the speed range of 55~100 km/h. NO_x emission factors over low speed range of 0~5 km/h reached 7.2 g/km.

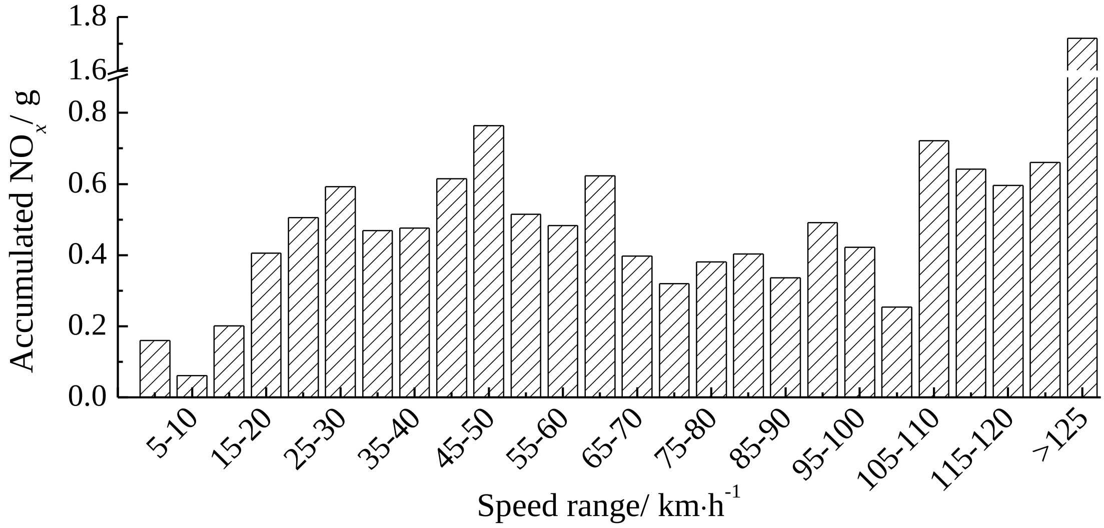

(a) Accumulated NO_x emissions over various speed bins

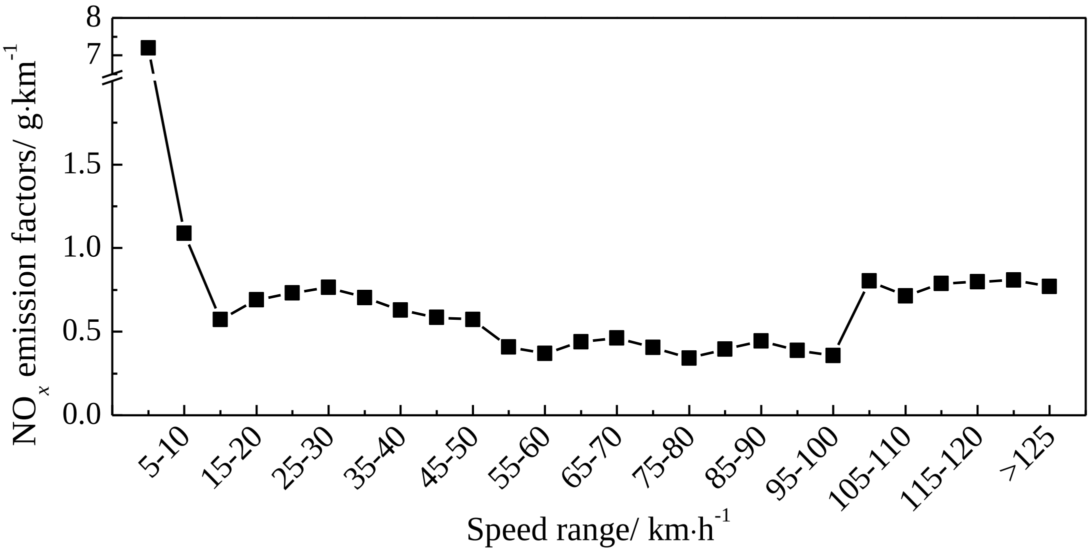

(b) Average NO_x emission factors over various speed ranges

Figure 3.10: Accumulated engine-out NO_x emissions and average emission factors over various speed ranges

Accumulated engine-out NO_x emissions over various acceleration ranges are shown in Figure 3.11(a). NO_x emissions generated in the acceleration range of -0.1 m/s^2~ 1.1 m/s^2 accounted for the largest percentage of NO_x emissions. NO_x emissions over the acceleration range of <-0.2 m/s^2 and >1.6 m/s^2 were quite low. Average NO_x emission factors increased continuously with acceleration when acceleration was higher than -0.1 m/s^2 (see Figure 3.11(b)). NO_x emission factors for the acceleration < -0.1 m/s^2 were almost zero. During the aggressive deceleration process, little fuel was injected into the engine cylinders; even the fuel injection was completely cut off. Large acceleration meant much fuel injection and high combustion temperature which contributed to high NO_x formations.

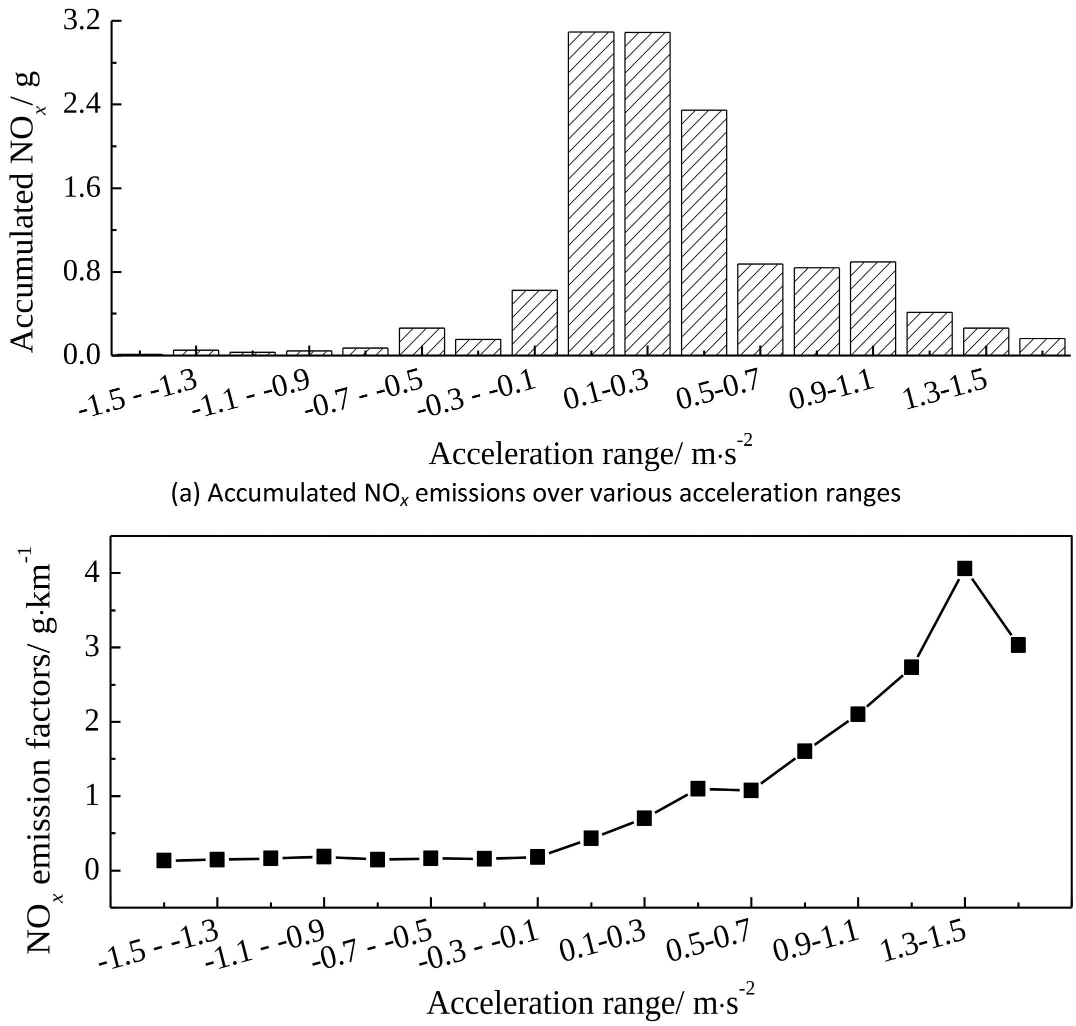

(a) Accumulated NO_x emissions over various acceleration ranges

(b) Average NO_x emission factors over various acceleration ranges

Figure 3.11: Accumulated engine-out NO_x emissions and average emission factors over various acceleration ranges

3.5 Relationships between gear-shift strategy and engine-out NO_x emissions

Gear shift strategy affected the engine operation regions in which the emission factors varies greatly although the power output was the same. So, the gear shift will indirectly influence the powertrain emission factors. Figure 3.12 shows the effect of gear shift strategy on engine-out NO_x emissions in the whole WLTC. There was an optimal gearshift strategy, causing the lowest NO_x emission formations. The engine operation points of WLTC driving cycle in NO_x emission factors and temperature maps are shown in Figure 3.13 and Figure 3.14 respectively. The exhaust temperature would affect the efficiency of the down-stream after-treatment systems.

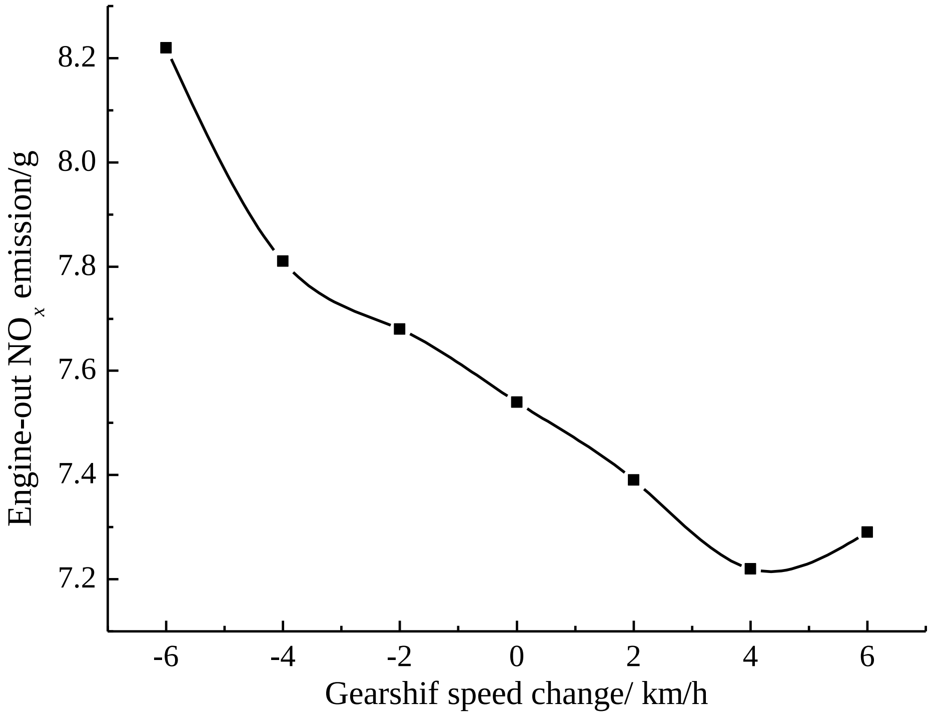

Figure 3.12: Scenarios of the after-treatment system layouts

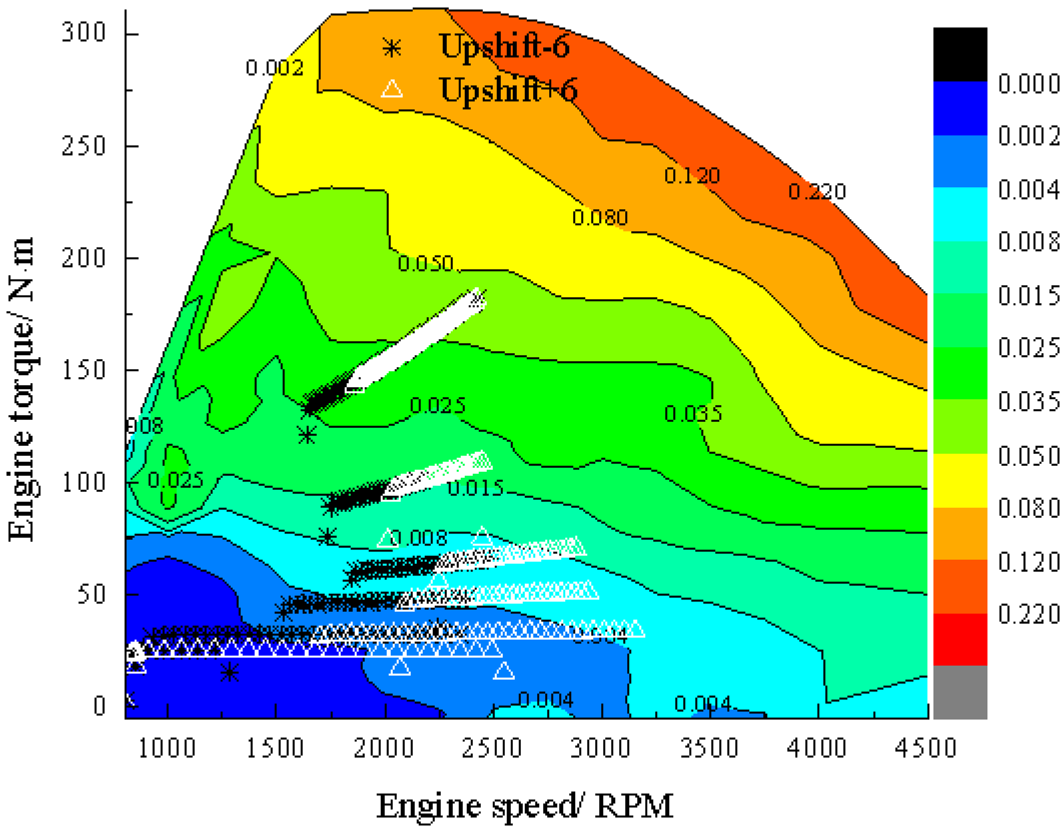

Figure 3.13: Engine operation points in NOx emission map

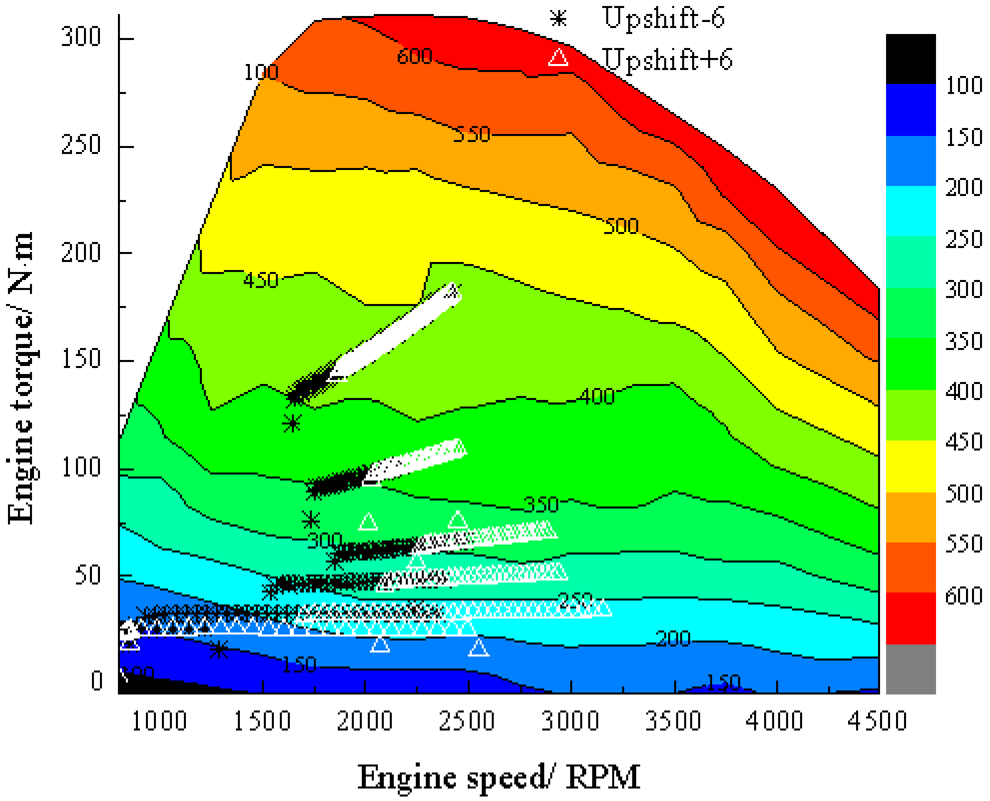

Figure 3.14: Engine operation points in exhaust temperature map

3.6 Mathematical emission model

3.6.1 Instantaneous emission model

The building of the mathematical emission model was based on the simulation results of GT-SUITE vehicle model. Firstly, the relationships between the vehicle power and driving behaviours (e.g. vehicle speed and vehicle acceleration) were set up based on the following equation.

$$P(t) = \frac{1}{3600\eta_d}\ v(t)\left\{\frac{\rho}{25.92} C_D C_h A_f v(t)^2\ + g\ MC_R + g\ M\ \sin\theta + (1+\lambda)\ Ma\right\} \qquad \text{(Eq. 3-1)}$$

where,

- $P(t)$, vehicle power;
- η_d, mechanical efficiency;
- ρ, air density;
- $v(t)$, instantaneous vehicle speed;
- A_f, front area of the vehicle;
- $C_D C_H$, aerodynamic drag coefficient;
- g, gravitational constant;
- C_R, rolling resistant;
- λ, rotational inertia;
- M, vehicle mass;
- θ, road grade;
- $a(t)$**,** instantaneous vehicle speed.

The equation between vehicle power and engine-out emission rates was created based on the simulation results using a specific diesel passenger car. Finally, based on the combinations of both equations, the relationships between engine-out emission rates and driving behaviours were obtained. When the vehicle was fully warmed up, the efficiency of the after-treatment systems was really high, the pipe-out emission rates were quite low. The relationships between pipe-out NO_x emission rates and driving behaviours will be significantly weakened. The input and output parameters of engine-out NO_x mathematical equation model are shown in Table 3.2 and Table 3.3. The relationships between vehicle power and NO_x emissions are shown in Figure 3.15.

$$E_{NOx} = f(P(t)) \qquad \text{(Eq. 3-2)}$$

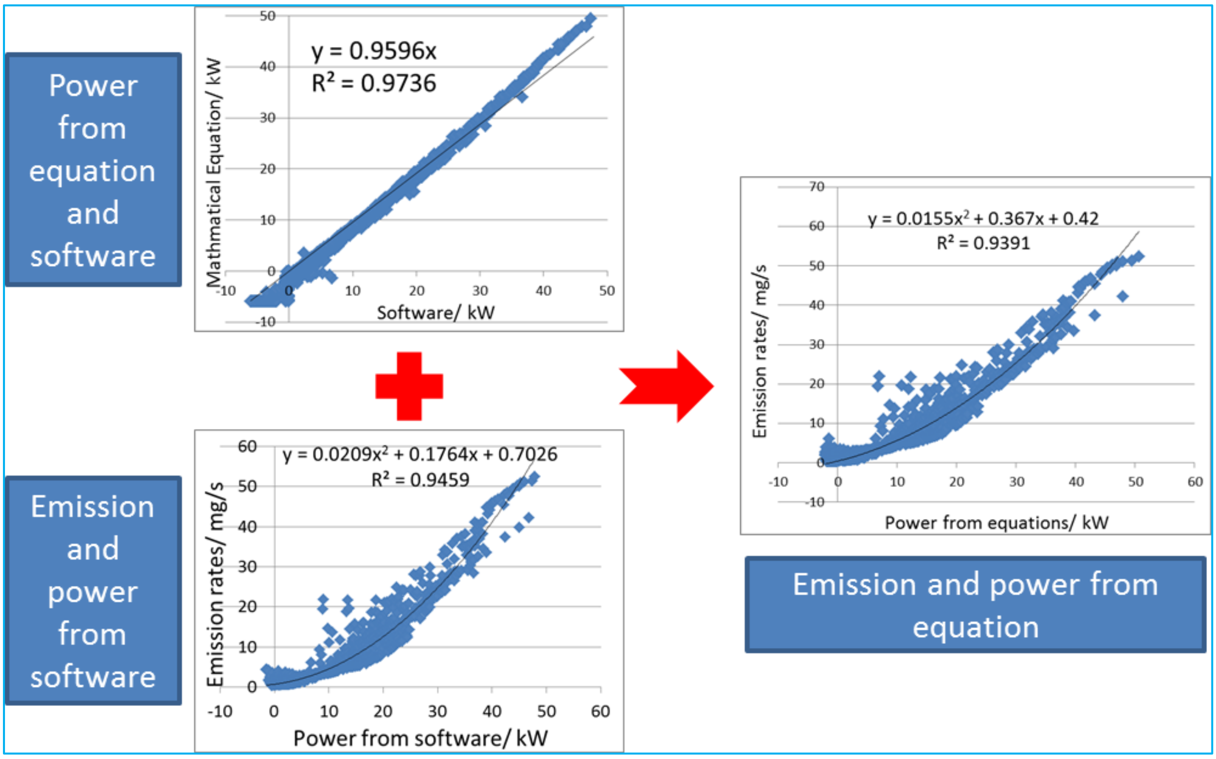

Figure 3.15: The relationships between vehicle power and engine-out NO_x emission

Table 3.2: Input parameters of the mathematical emission model

Input parameters	Units	Frequency
Instantaneous Vehicle speed	km/h	1 Hz
Instantaneous vehicle acceleration	m/s^2	1 Hz
Road gradient	%	1/(10m)

Table 3.3: Output parameters of the mathematical emission model

Output parameters	Units	Frequency
NO_x emission rates	mg/s	1 Hz

The following equation shows the relationship between the instantaneous engine-out emission rates and KPIs of driving behaviours.

$$E_{NOx} = C_1 v^6 + C_2 v^5 + C_3 v^4 + C_4 v^3 + C_5 v^2 + C_6 v + C_0 \quad \text{(Eq. 3-3)}$$

Where,

- C_0~C_6 are coefficients of the Equation;
- E_{NOx} is engine-out NO_x emission rates;
- v is instantaneous vehicle speed;
- a is instantaneous vehicle acceleration;
- θ is road gradient.

In this equation, driving behaviours include the instantaneous vehicle speed and acceleration, and the data frequency is 1Hz.

Table 3.4: Coefficients of mathematical equations

Variables	Coefficients	Value
v^6	C_1	1.21×10^{-12}
v^5	C_2	0
v^4	C_3	$1.24 \times 10^{-7} a + 1.22 \times 10^{-7} sin\theta + 1.6 \times 10^{-2}$
v^3	C_4	3.25×10^{-6}
v^2	C_5	$3.18 \times 10^{-3} a^2 + 0.305(sin\theta)^2 + 8.0 \times 10^{-3} sin\theta + 6.23 \times 10^{-2} asin\theta + 8.14 \times 10^{-4} a + 5.21 \times 10^{-5}$
v^1	C_6	$0.166\text{a} + 1.63\sin\theta + 0.0213$
v^0	C_0	0.42

3.6.2 Scaling up of emission models

The scaling up of the emission models takes (Eq. 3-3 as the baseline which is a Euro-6 diesel passenger car. The emission factors of vehicles varied with the mileage class, as shown in Table 3.5. NO_x emission factors were increased to 1.747 g/km when the mileage was higher than 90000km. Based on the relationships between mileage class and NO_x emission factors, emission factors over different mileage would be obtained.

Table 3.5: Relationships between mileage and NOx emissions (Ntziachristos and Samaras, 2000)

Mileage class, 10^3 km	NOx, g/km
<10	0.639
10-30	0.711
30-50	0.897
50-70	1.142
70-90	1.522
>90	1.747

The relationship between NO_x emission factors and mileage class is given in the following equation,

$$E_M = 6 \times 10^{-7}M^3 + 8 \times 10^{-5}M^2 + 0.0008M^2 + 0.6339 \qquad \text{(Eq. 3-4)}$$

Where,

- M is the mileage of the target vehicle.

The emission limits of different types of passenger cars are shown in Table 3.6. There was an assumption that the real-world NO_x emission factors of different types of vehicles had the same tendency with the emission limits in Table 3.6. Coefficients of the NO_x emission model of a given vehicle are presented in Table 3.7.

Table 3.6: Emission limits of different types of cars

	Vehicle type		Euro 3/ g/km	Euro 4/ g/km	Euro 5/ g/km	Euro 6/ g/km
Passenger car	Petrol		0.15	0.08	0.06	0.06
	Diesel		0.50	0.25	0.18	0.08
Light commercial vehicles	Petrol	Class I	0.15	0.08	0.06	0.06
		Class II	0.18	0.10	0.075	0.075
		Class III	0.21	0.11	0.082	0.082
	Diesel	Class I	0.50	0.25	0.18	0.08
		Class II	0.65	0.33	0.235	0.105
		Class III	0.78	0.39	0.280	0.125
		N_2	n.a.	n.a.	0.280	0.125
Heavy duty	Diesel/ natural gas		5.0 g/kWh	3.5 g/kWh	2.0 g/kWh	0.46 g/kWh

Table 3.7: Coefficients of NO_x emission model of different types of cars

Variables	Coefficients	Value
v^6	C_1	$1.21 \times 10^{-12} k_i j_i$
v^5	C_2	0
v^4	C_3	$(1.24 \times 10^{-7}a + 1.22 \times 10^{-7}sin\theta + 1.6 \times 10^{-2})k_i j_i$
v^3	C_4	$3.25 \times 10^{-6} k_i j_i$
v^2	C_5	$(3.18 \times 10^{-3}a^2 + 0.305(sin\theta)^2 + 8.0 \times 10^{-3}sin\theta + 6.23 \times 10^{-2}asin\theta + 8.14 \times 10^{-4}a + 5.21 \times 10^{-5})k_i j_i$
v^1	C_6	$(0.166a + 1.63\sin\theta + 0.0213)\, k_i j_i$
v^0	C_0	$0.42 k_i j_i$

In Table 3.7, k_i and j_i are calculated using the values in Table 3.5 and Table 3.6,

$$k_i = \frac{E_i}{0.08} \qquad \text{(Eq. 3-5)}$$

$$j_i = \frac{E_M}{0.639} = (6 \times 10^{-7}M_i^3 + 8 \times 10^{-5}M_i^2 + 0.0008M_i + 0.6339)/0.639 \qquad \text{(Eq. 3-6)}$$

where,

- E_i is the corresponding approval emission factors of target vehicle *i* in Table 3.5;
- M_i is the mileage in 10^3km of target vehicle *i*.

3.7 Conclusion

In this section, fuel consumption and NO_x emission characteristics over various scenarios were analysed; the correlations between NO_x emissions and driving behaviours were explored using simulation methods; further, the NO_x emission model of different types of vehicles were setup. The main conclusions are as follows:

(1). Medium and extra-high vehicle speed contributed the highest proportions to the fuel consumption in WLTC. Fuel consumption rates over vehicle speed showed a “V” shape, with the highest fuel consumption rate being under low vehicle speed. Operations with low acceleration had the highest proportions of total fuel consumption, and the fuel consumption rates almost linearly increased with positive acceleration.

(2). Medium and extra-high vehicle speed ranges contributed to the most engine-out emissions; NO_x emission factors were the lowest in the speed range of 50~100 km/h. NO_x emissions generated in the acceleration range of -0.1 m/s^2~ 1.1 m/s^2 accounted for the largest percentage of NO_x emissions. Average NO_x emission factors increased continuously with acceleration when acceleration was higher than -0.1 m/s^2. There was an optimal gearshift strategy, causing the lowest NO_x emission formations, and it corresponded to the gearshift speed change of 4 km/h.

(3). A mathematical NO_x emission model of a diesel passenger car meeting Euro 6 emission regulations was setup based on the simulation results. Taking it as the baseline, the NO_x emission models of different types of vehicles were established based on the mileages and emission standards.

4 Simulation and modelling of brake wear emissions

Non-exhaust airborne particle emissions are a main contribution for the air quality in cities and it can affect human health (Forouzanfar et al., 2016; SCIENTIFIC, 2013). Most of the studies in this field have been focused on engine emissions. Recently, it has been showed that the non-exhaust emissions from road vehicles are as important as the engine emissions for PM_{10} (Grigoratos and Martini, 2015). Brake systems are one of the main sources of non-exhaust emissions. During braking, the rotor slides against the pads and the contact surfaces wear. Some of the wear debris becomes airborne, some falls to the ground, and some gets stuck on surfaces in the environment.

The wear and airborne emissions from disc brakes strongly depend on the contact pressure, temperature, and sliding speed distribution in the contact interface between the pads and rotor (Kukutschová et al., 2011; Mathissen et al., 2018; Tirovic and Day, 1991; Wahlström, Jens et al., 2017). In turn, the wear affects the surface geometries of both the pads and rotor and therefore the contact pressure and temperature distributions. It is hard to study the contact during braking (Eriksson et al., 2001) and thus different simulation approaches focussing on contact pressure, contact temperature, and wear have been developed by different authors in the past (Afzal and Mujeebu, 2019; Söderberg et al., 2008). The overall aim with these kinds of simulation approaches is to explain what is happening in the pad-to-rotor interface during braking and to predict wear and temperature.

Finite Element Analysis (FEA) can be used to better understand the contact behaviour on a macroscopic size scale. (Ouyang, 2008) used an FEA to compute the contact pressure between rotor and pads, and they compared the results with experimental tests. (Han et al., 2017) performed a thermomechanical analysis to study the effect of a non-uniform contact pressure distribution on wear. They also developed a pad shape optimization in order to have a more uniform contact pressure distribution. Infrared thermal images of the rotor can be used to calibrate FEA contact simulations (Goo, 2018). (Schmidt et al., 2018) developed a 3D transient non-linear FEA to predict the wear on a tilted shaft-bushing bearing. (Sun et al., 2019) proposed a model to investigate the rail non-uniform wear evolution combining the vehicle dynamic, the Kalker's variational method and Sheffield University material wear model. (Söderberg et al., 2008) developed an FEA approach to compute the pressure distribution on the contact interface. From the pressure distribution, knowing the sliding velocity, a generalized Archard's wear law and Euler's integration scheme were used to simulate the wear. (Wahlström et al., 2009) further developed this approach to include airborne particle emission.

To our knowledge, Few studies can be found in the literature (Wahlström, 2015), which focus on simulation of airborne particle emissions for the Worldwide Harmonised Light Vehicle Test-Brake (WLTP-Brake). This chapter presents the simulated airborne emissions and compares with from dyno bench tests run with WLTP-Brake in order to validate the simulated results.

4.1 Simulation and experimental methods

Figure 4.1 shows an overview of the simulation methodology and its validation procedure. At first, the specific wear rate and particle rate are mapped with respect to different contact pressures (*p*) and sliding speeds (*v*) by experiments conducted in a pin-on-disc tribometer on material level (Riva et al., 2019; Wahlström, Jens et al., 2017). These maps are then used as input to an FEA on component level. To investigate the validity of the simulation methodology, the simulated pads and rotor wear, and airborne particle emission are compared to experimental measurements in a dyno bench designed for particle emission studies (Perricone et al., 2016).

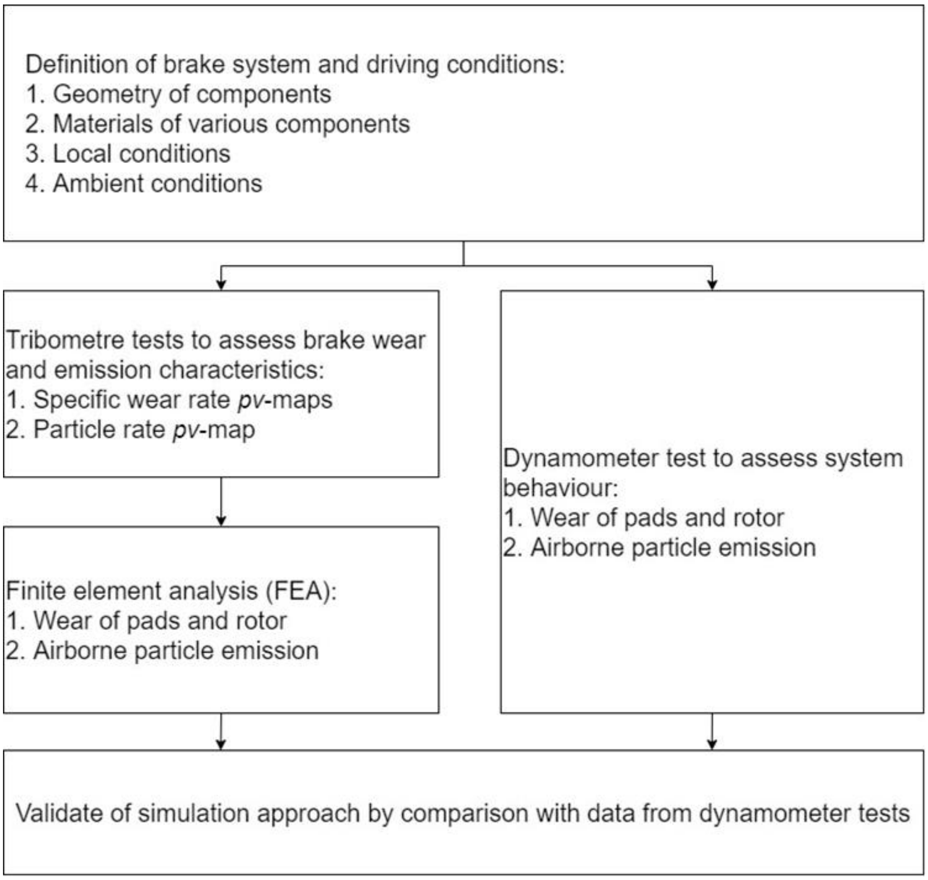

Figure 4.1: Flow Schematic of proposed simulation method for brake wear simulation

4.1.1 Brake system

A left front disc brake system of a typical medium-sized car is used in this study, as shown in Figure 4.2. Important data for the reference car and brake system is summarised in Table 4.1. This disc brake consists of a sliding calliper, two low-metallic pads, and a ventilated grey cast-iron rotor. The densities of the friction material and the rotor are 2.75 and 7.1 g/cm^3, respectively.

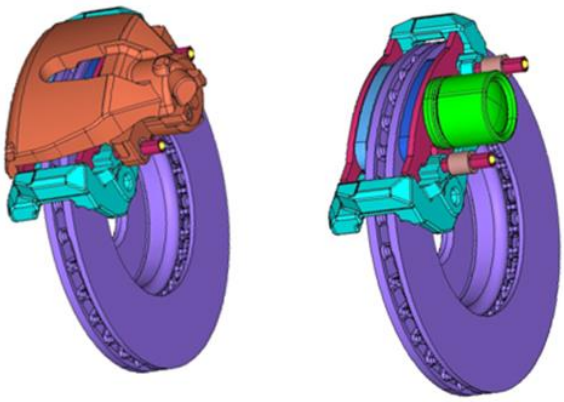

Figure 4.2: Single piston sliding calliper disc brake

Table 4.1: Parameters of the car and its front left disc brake

Brake system	Parameters
Total weight	1600 kg
Wheel radium	314 mm
Rotor outer radius	139 mm
Rotor inner radius	80 mm
Rotor effective radius	113 mm
Pad surface area	5080 mm^2
Cylinder diameter	57 mm

4.1.2 Braking cases

WLTP-Brake was employed to investigate the characteristics of the BWPs. WLTC is the most recently developed test driving cycle. It represents the average driving pattern of light-duty vehicles, which is composed of 700,000 vehicle driving data collected from Europe, the United States, Korea, Japan, and India. The NEDC has been used in European countries to measure the exhaust emissions and fuel economy before WLTC, which consists of four repeated ECE-15 urban driving cycles (UDCs) and one extra-urban driving cycle (EUDC). The EPA Federal Test Procedure, commonly known as FTP-75 for the city driving cycle, is a series of tests defined by the US Environmental Protection Agency (EPA) to measure the tailpipe emissions and fuel economy of passenger cars. The above three test driving cycles were originally intended for measuring the exhaust emissions and fuel economy, not for measuring BWPs, while measuring BWPs.

WLTP-Brake consists of 10 trips, and a soaking time exists between each trip to set the same initial operating temperature of the brake disc. In the current procedure of WLPT-Brake cycle established by PMP, the soaking condition of each trip is determined as temperature based (initial operating disc temperature of 40 ◦C), not time based. In this study, although the soaking condition of each trip was determined as time based which was 10 min of soaking time, the initial operating temperature was maintained below 40 ◦C.

4.1.3 FEA approach

The first step of the simulation algorithm is to set up the FE-model to compute the contact pressure distribution during braking in order to be able to calculate the wear and the particle emissions. The model has been developed starting from the work of Valota et al. (Valota et al., 2017). It has been expanded to consider the specific wear variation of the pads with sliding velocity and contact pressure, and to compute the particle emissions by introducing wear and particle emission *pv*-maps. The simulation procedure has been implemented in Abaqus (Abaqus). A routine has been developed to compute the wear and the particle emissions for each braking of the load cycle test. After each braking, the mesh is updated by removing the computed wear and the FEA is solved for the next braking. Figure 4.3 shows an overview of the proposed simulation algorithm. In the following sections, the FE model setup, the wear, and particle emission routine will be illustrated.

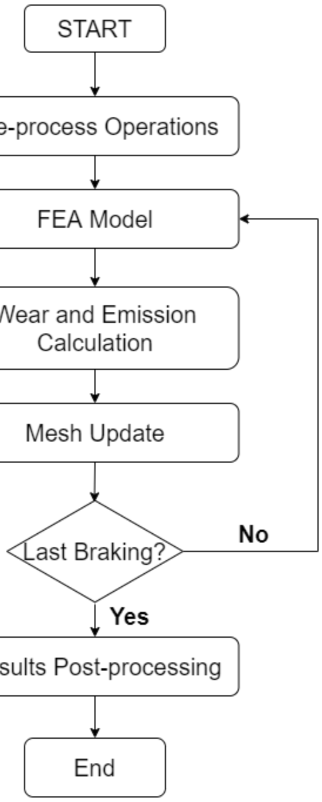

Figure 4.3: An overview of the brake wear simulation algorithm

4.1.3.1 Pre-process

The procedure starts with a pre-process in which the geometries are defined, the meshes are generated, and test cycle is set. The FE simulation includes the disc brake components: rotor, pads friction material, back-plates, piston, calliper, carrier, and sliding pins. An illustration of the meshed components is presented in Figure 4.4. The applied load and the rotational velocity are defined by the test cycle. The calliper can slide with respect to the grounded carrier on the sliding pins. The load consists of two steps. First, the pressure is applied on the back of the piston and to the cylinder walls. Second, the pressure is kept and a motion is applied to the rotor to simulate the rotation.

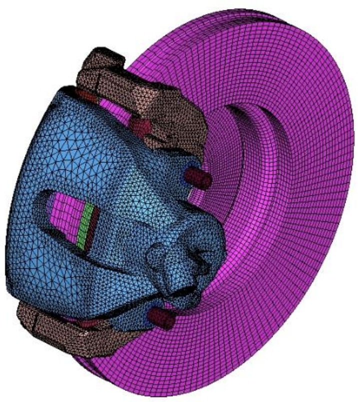

Figure 4.4: Mesh of the disc brake geometry

The FEA output is the contact pressure distribution of the pads-disc interface during braking. To simplify the wear routine, the rotor and friction material mesh is set to be hexahedral and the angular distance between nodes (Δθ) on the brake ring is set to be constant. Abaqus ALE (Arbitrary Lagrangian Eulerian adaptive meshing) technique manages the nodes position update after every braking (Abaqus).

4.1.3.2 Wear calculation

A subroutine has been developed in order to determine the wear and the particle emissions during a test cycle. The wear and the emissions are considered for both the pads and the rotor. The *pv*-map in Figure 4.5 is used to compute the pad-specific wear rate as a function of the local contact pressure and the sliding velocity. The disc specific wear rate is set as constant. A generalization of Archard's wear law (Archard, 1953) is used to compute the amount of wear for every node. According to this law, for the pad nodes, the wear is given by the product between the specific wear rate, the contact pressure, and the sliding distance:

$$\Delta h_p = k_p(p,v) \cdot p \cdot \Delta s \qquad \text{(Eq. 4-1)}$$

Where:

- k_p is the specific wear rate of the pad, and it is a function of pressure and velocity;
- p is the cell contact pressure that is kept constant;
- Δs is the node sliding distance;

To make the speed change during a braking into account, every braking is divided into n steps and Eq. (4-1) is computed *n* times for every braking. The deceleration *a* is considered constant during a single braking. Considering the time discretisation of each brake event, the pad wear during a single braking can be re-written as follows:

$$\Delta h_p = p \sum_{i=1}^{n} k_p(p, \tfrac{v_i + v_{i+1}}{2}) \Delta s_i \qquad \text{(Eq. 4-2)}$$

Where:

- Δs_i is the sliding distance during a sub-step.

Considering the constant deceleration a, it can be computed using the linear motion equation by Eq. (4-3):

$$\Delta s_i = v_i \Delta t + \tfrac{1}{2} a \Delta t^2 \qquad \text{(Eq. 4-3)}$$

Assuming a constant deceleration during a braking, the disc wear can be computed as follows (Valota et al., 2017):

$$\Delta h_d = \frac{\alpha}{2\pi} \sum_{\theta=0}^{2\pi} k_d \frac{p(r,\theta) + p(r,\theta+\Delta\theta)}{2} \Delta\theta \cdot r \qquad \text{(Eq. 4-4)}$$

Where:

- α is the rotation angle;
- k_d is the disc specific wear rate;

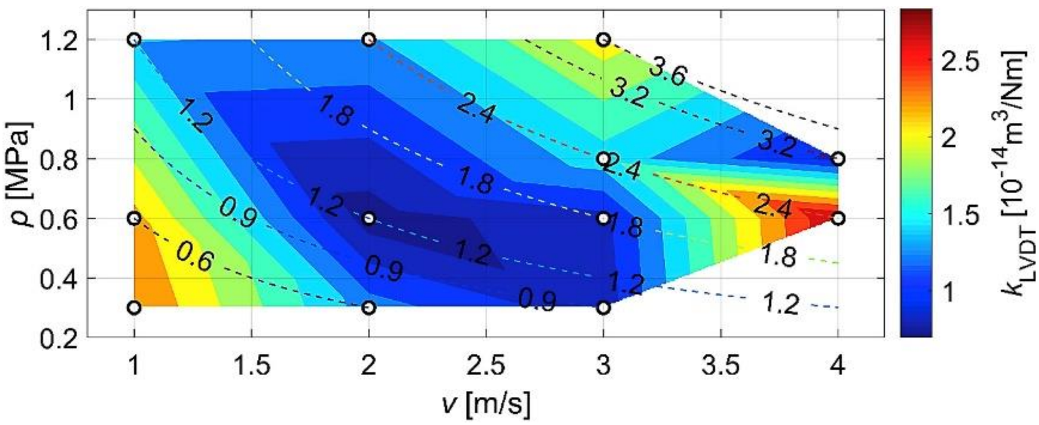

Figure 4.5: Nominal contact pressure (p) and sliding velocity (v) map of the pin specific wear rate (k_{LVDT}).

In the above figure, the *p* and *v* used in the pin-on-disc tribometer are marked with circles. The *pv*-values are represented with dashed isolines (Wahlström, J. et al., 2017)

4.1.3.3 Particle emission calculation

In the same way as for the pad wear, a *pv*-map used as input for the particle emission computation (Figure 4.6). From this map, knowing the node contact pressure and the sliding velocity, the particle emissions are given as mass per sliding distance [µg/m]. Starting from the map it is possible to compute the total brake emissions for each brake event. The brake emission for each braking, in terms of mass, is given by the map in Figure 4.6 scaling the nodal area with the pin area and considering the sampling efficiencies:

$$m_{particle} = \varphi_{POD} n_{ELPI+}(p, v) \frac{A_{nodal}}{A_{pin}} \quad \text{(Eq. 4-5)}$$

Where:

- n_{ELPI+} is the particle emission per sliding distance and is given by the *pv*-map;
- A_{nodal} is the nodal area of the FEA mesh;
- A_{pin} is the pin area;
- φ_{POD} is the particle sampling efficiency of the pin-on-disc tribometer due to anisokinetic sampling.

This sampling efficiency has been simulated with a CFD (Computational Fluid Dynamics) analysis by (Riva et al., 2017) to 80.1% for PM_{10} emissions and considers the sampling losses due to anisokinetic conditions in the tribometer test setup. Considering that in every braking the contact pressure and the deceleration are constant, only the velocity changes. To consider this velocity change, as done for the pad wear computation, every braking can be time-discretised in n sub-steps, and Eq. (4-6) can be re-written as follows:

$$m_{particle} = \varphi_{POD} \left(\sum_{i=1}^{n} n_{ELPI+}(p, v)\, \Delta s_i\right) \frac{A_{nodal}}{A_{pin}} \quad \text{(Eq. 4-6)}$$

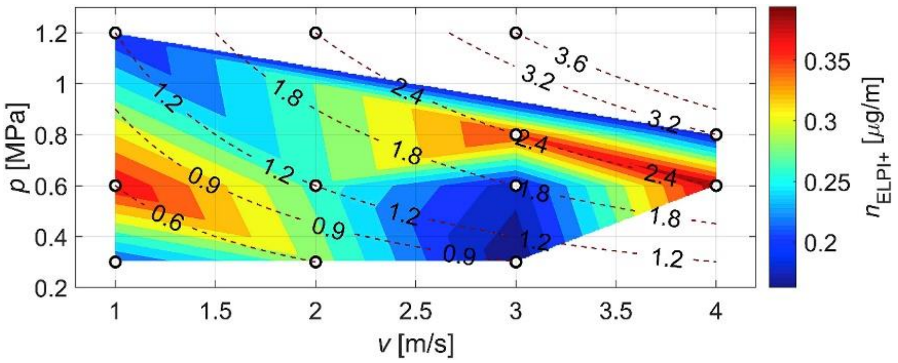

Figure 4.6: Nominal contact pressure (*p*) and sliding velocity (*v*) map of the airborne mass rate (n_{ELPI+}).

In the above figure, the *p* and *v* used in the pin-on-disc tribometer are marked with circles. The *pv*-values are represented with dashed isolines (Wahlström, J. et al., 2017)

The dyno bench is schematically illustrated in Figure 2.20 and described in Section 2.2.1.

4.2 Brake wear analysis

A simulation tool that can provide a prediction of wear and airborne emissions from disc brakes could be a crucial tool in the design phase of novel disc brake systems. In the present work, the validity of an FEA simulation approach to predict wear and airborne emissions was investigated.

The contact pressure distribution for two similar brake events, in terms of pressure in the cylinder of the calliper (p_{cyl}), at the beginning of the WLTP-brake cycle are shown in Figure 4.7 in order to illustrate the development of the contact pressure. The brake events correspond to brake event #5, p_{cyl}=0.54 MPa. The piston side pad contact pressure distributions (Figure 4.7: left column) show that the pressure increases with the radii and toward the disc inner side at the beginning of the test; at the end of the cycle the contact pressure is more uniform. On the finger side (Figure 4.7: right column), the contact pressure increases just with the radii at the beginning of the cycle and it has a gradient from the centre to the inner and outer sides at the end of the cycle. It can be also noted that the only border that works a lot during braking is the outer side of the pistons pad, where high pressure values are shown.

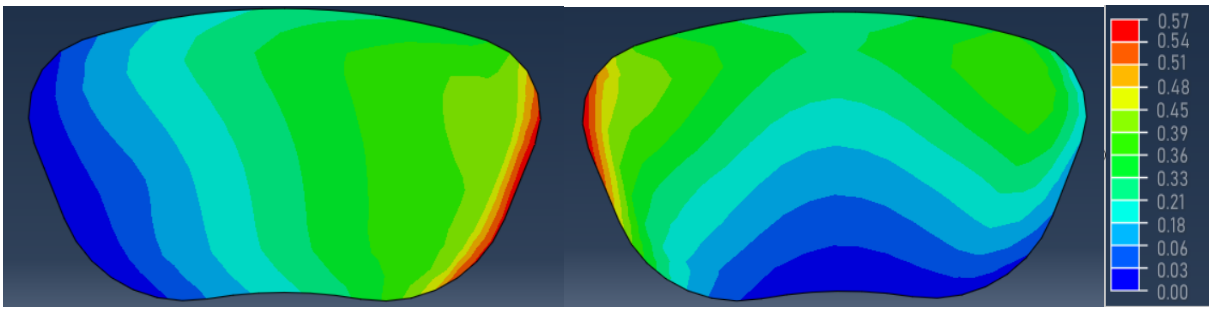

Figure 4.7: Contact pressure distribution (MPa) on the brake piston (left column) and finger side (right column)

The pad wear after the brake event #5 is shown in Figure 4.8. The pad wear is generally higher for larger radii. Moreover, the wear gradient is moved slightly towards the inner side for the piston side pad. Two of the main factors influencing the wear are the contact pressure and sliding distance. By comparing brake event #5, it is possible to see how the wear of the pads and adapt their contact surfaces to even out the contact pressure distributions. This is a consequence of the Archard's wear law. Also, it is possible to see that the wear increases with the sliding distance for both the pads and the rotor. This is clearer on the rotor surface since there is no wear gradient in the tangential direction due to the rotation. In contrary, the pad wear is influenced by the contact pressure and the sliding velocity in a tangential direction. It is important to remember that the pad wear dependence on the contact pressure and sliding velocity is non-linear since it also depends on the specific wear of the pad, which depends on these two variables. Temperature effects are neglected in the presented simulation approach.

It is known that the temperature of disc brake systems influences both the material and system parameters for the pads and rotor. Thermal expansion or softening of the materials could affect the contact pressure distribution and contact area, and in turn, the local wear. Also, it is known that the resin of the pad materials is sensitive to high temperatures. (Cristol-Bulthé et al., 2008) tested an OMC pin against a cast iron disc with a pin-on-disc tribometer at different controlled disc temperatures, and concluded that the wear depth of the pad resin is about 35–55 µm disc temperatures below 100° and 50–75 µm disc temperatures above 500 °C. This could also affect the contact pressure and area distribution. It should be mentioned that, as regards wear and emissions, the dependence of temperature is implicitly given by the *pv*-maps, since a higher *pv* will result in a higher temperature.

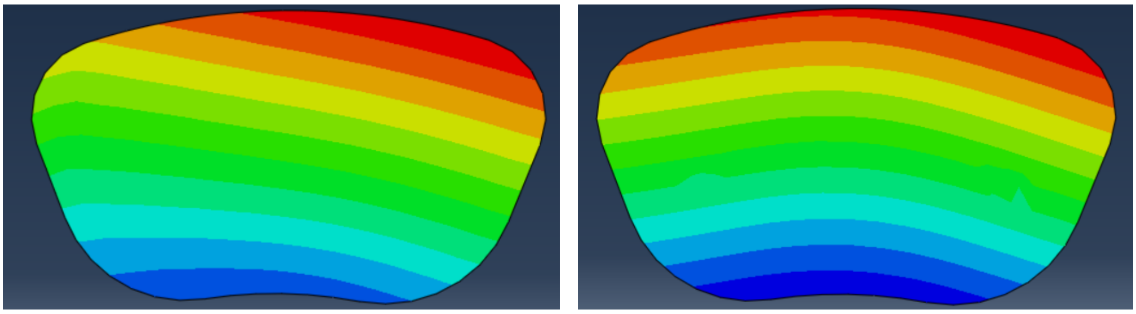

Figure 4.8: Brake pad wear on the piston (left column) and finger side (right column)

4.3 PM_{10} emissions of WLTP brake cycle

To better understand the differences in simulated and measured wear two points are discussed below. First, the load is determined by the brake torque to obtain a constant deceleration in the inertia dyno test while in the FEA the cylinder pressure and coefficient of friction are set as constant. This results in a constant brake torque during a brake event. The first reduced cycles could still be in the run-in phase. On the other hand, the simulation corresponds to a single reduced WLTP-brake cycle, with the geometry corresponding to the new configuration.

There are few studies reported in the literature about the simulation of airborne emissions from disc brakes. (Wahlström, J. et al., 2017) presented an FEA approach and used it to simulate wear and airborne emissions from a disc brake contact pair run at constant normal load and rotational velocity. The images presented of the simulated wear are different from the result presented in the present section. This could be explained by the fact that they did not include the effect of the calliper in the FEA. By including the calliper, it is possible to consider non-symmetric effects between the piston and finger side. The contact pressure acting on the finger side pad is not the same as the piston side pad since the load is applied in a different way (see Figure 4.7). Moreover, the brake torque pushes the back-plates of the pads against the calliper supports which results in a non-symmetric pressure distribution in the tangential direction. Also, the reduced WLTP-brake cycle used in the present work is made by continuously changing brake torque and rotational velocity, because it represents a city traffic cycle. With this kind of cycle, no steady state condition is reached in the end, and no uniform contact pressure distribution is reached. The specific wear rate and contact pressure are not constant due to the continuous change in the kind of brake event. Sliding distance, instead, is always higher on external radii, which is why it appears clear for both pads and rotor that the higher the radius, the higher the wear is. The same considerations can be made when looking at the work of (Söderberg et al., 2008) where the influence of the pistons is more evident on the wear.

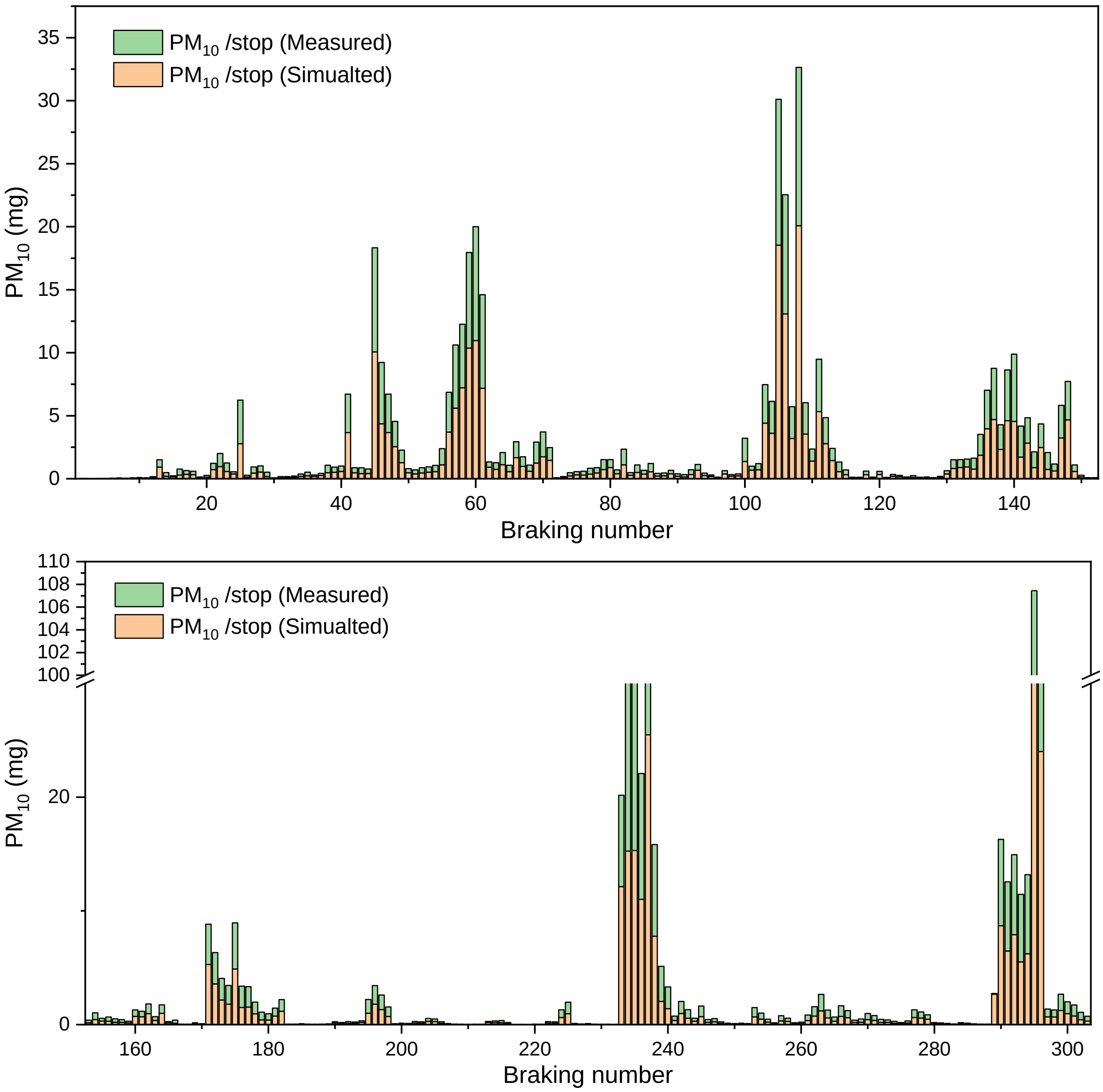

Figure 4.9: Brake wear PM_{10} emissions obtained the simulation and experimental test

(Valota et al., 2017) showed the results of a FEA using a fixed calliper tested with the SAE-J2707 wear cycle. This cycle is divided into blocks of equal deceleration braking. In this way, a situation closer to the steady condition seems to be reached and the disc wear is uniform along the braking ring where the pads slide. Also, the pad wear is more uniform, but is more concentrated in the upper half of the contact area. It is important to underline that these results were obtained considering a fixed calliper, so the pressure distribution can be completely different because the braking mechanism is different. (AbuBakar and Ouyang, 2008) used an FEA approach to simulate the contact pressure distribution during 80 min of dragging at constant pressure and rotational velocity. A floating calliper like the one used in this work has been employed. At the beginning of the cycle they found higher pressure values at higher radii, while after 80 min the contact pressure is more uniform on the entire surface, which is higher where the contact pressure and the sliding distance are greater. This behaviour is in line with what has been presented in this work, especially for pad on the finger side. One way to investigate and validate a simulation model is to compare experimental and simulation results. The focus of the driving cycle used in the present work was to simulate WLTP-brake driving cycle. To simulate the total wear and airborne emissions during the lifetime of a brake system, different test cycles which consider different driving styles and traffic situations could be run.

Figure 4.10 shows the total brake wear PM_{10} emissions during the WLTP-brake cycle. The WLTP brake test consists of 10 trips, totalling 192 km. It can be seen that the total brake wear PM_{10} emissions are the largest for Trip 10, which is related to braking events in this trip. In general, the tested PM_{10} emissions is larger than that from simulation in the cases of trips.

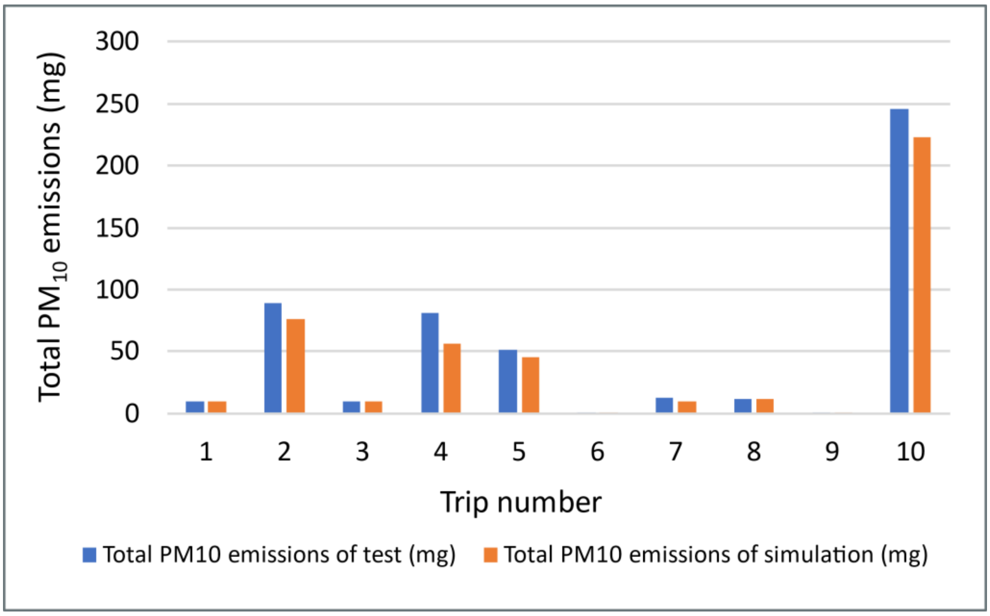

Figure 4.10: Total brake wear PM_{10} emissions during 10 trips of the WLTP-brake cycle

Figure 4.11 shows the brake wear emissions from simulated and tested data. The linear correlation coefficient, R^2, was calculated by means of simple linear regression to assess the strength of the linear relationship between these variables. The R^2 values are 0.91 between the brake wear PM_{10} emissions from the simulated and tested results, as shown in Figure 4.11. This result indicates that the simulated data has a definite correlation with the experimental test results. As a result, the simulation results are in good agreement with the experimental data. Based on this, the proposed methodology seems promising to simulate brake wear emissions from a disc brake system during WLTP-brake driving conditions.

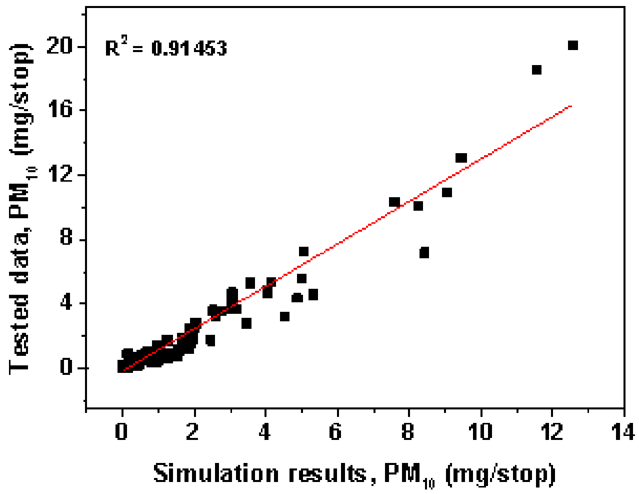

Figure 4.11: Brake wear emissions from simulation and tested data

4.4 Relationship between particle emissions and braking conditions

Figure 4.12 shows the relationship between the brake wear PM_{10} emissions and both the initial braking speed and the deceleration rate. Each bubble represents one stop, and the diameter of the bubble represents the deceleration rate. It is apparent that the brake wear PM_{10} emissions are associated with not only initial braking speed and deceleration rates. In general, most of braking event with higher initial braking speed and more intensive braking leads to higher brake wear PM_{10} emissions. From a thermodynamic perspective, higher deceleration rates most likely lead to higher local temperature at and very near the friction surfaces, where decomposition and volatilization of material is likely to take place. The findings in this study were reported by (Kukutschová et al., 2011; Niemann et al., 2020; Zum Hagen et al., 2019), who revealed that more nanoparticle generated from brake wear had a strong relationship with local temperature. As a result, harsh braking at higher speeds is to be avoided. (Vojtisek-Lom et al., 2021) revealed that braking from 175 to 100 km/h and from 5.28 to 7–9 m·s^{-2} caused 4–5 orders of magnitude more brake wear particles per stop and roughly 3 orders of magnitude brake wear particles per kWh compared to the majority of WLTP braking events at 20–70 km/h.

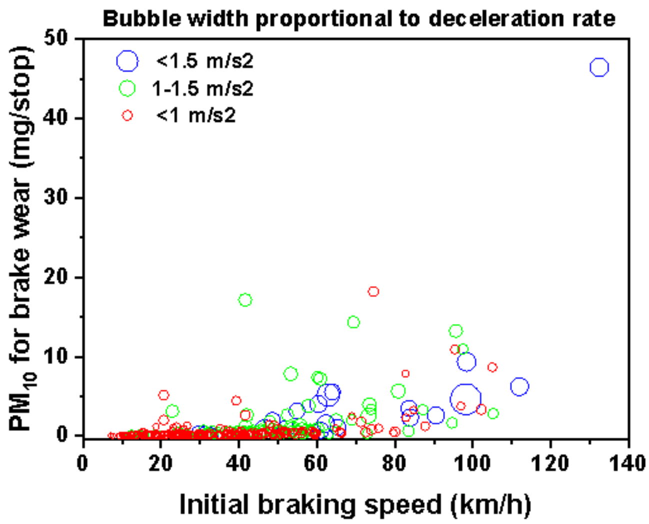

Figure 4.12: Brake wear PM_{10} per stop as a function of the initial braking speed

In the above figure, the bubble width is proportional to the deceleration rate. The relationship between the brake wear PM_{10} emissions and both the initial braking speed and the kinetic energy dissipated is presented in Figure 4.13. It shows a dependency on the brake wear PM_{10} per stop the total energy dissipated, with bubble area proportional to the average braking power. The brake wear emissions are expected to increase with the energy dissipated, while this relationship appears not to be proportional since braking event with lower kinetic energy dissipated emits higher brake wear PM_{10} emissions. (Vojtisek-Lom et al., 2021) found that brake wear particles appeared to be proportional with the energy dissipated until about 100 kJ per stop, after which the number of particles increases sharply with increasing energy dissipated, with higher braking power being somewhat associated with higher particle production.

From the operator perspective, the aggressiveness of driving can be monitored using inexpensive accelerometers and OBD and GPS data, as it is also associated with higher fuel consumption, higher emissions, higher tyre wear, and in many cases by increased probability of an accident due to reduced margin of safety. From the traffic planning and regulatory perspective, the data clearly demonstrates the benefits of enforcing the speed limits, as well as the benefits of reducing motorway speed limits in regions with poor air quality. Both have been proposed and, in some regions, implemented to reduce the emissions of CO_2, particulate matter and nitrogen oxides. Setting a legislative limit on the deceleration rate is not feasible, however, adherence to the general safety recommendations in road design and marking (adequate deceleration lanes, advanced warnings about necessary deceleration, appropriate speed limits), and enforcement of the safe following distance between vehicles, could prevent at least inadvertent harsh braking.

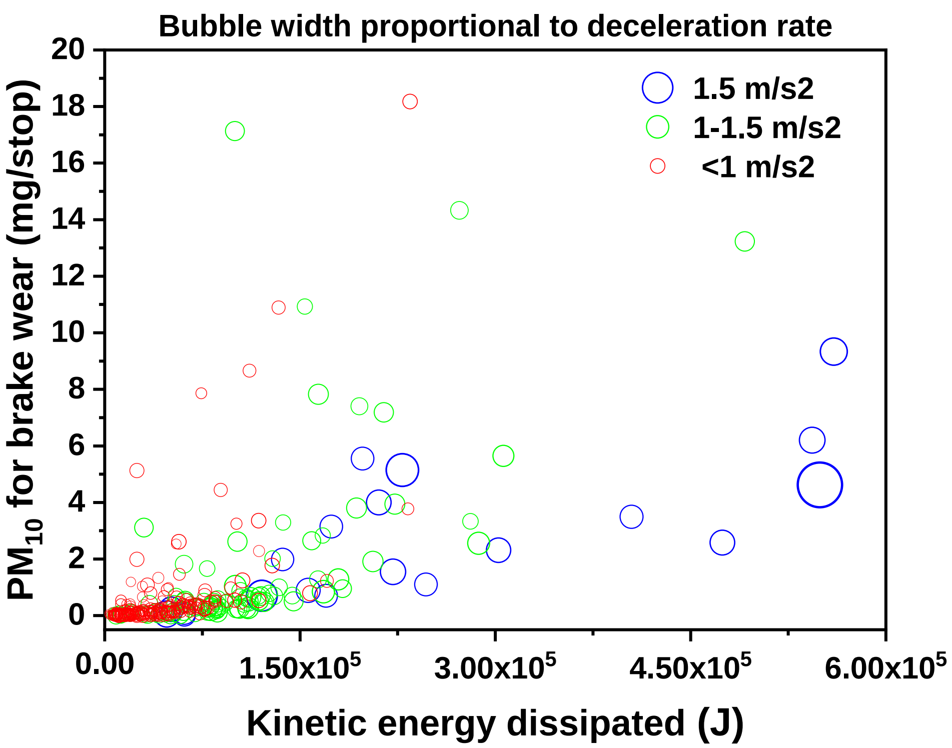

Figure 4.13: Brake wear PM_{10} emissions per stop vs. energy dissipated per stop

4.5 Mathematical model of brake wear emissions

The calculation equation is as follows according to the classical Archard wear theory was proposed by J. Archard (Archard, 1953):

$$V_w = \frac{1}{3} K F_N L \qquad \text{(Eq. 4-7)}$$

Where,

- V_w is the wear volume;
- F_N is the normal force of the contact surface;
- K is the specific wear rate that is related to material component;
- L is the relative sliding distance.

When braking, the work done against friction must be equal to kinetic energy of the vehicle (Kakad et al., 2017).

$$NkF_N L \cong \frac{1}{2} M(v_1^2 - v_2^2) \longrightarrow F_N L \cong \frac{1}{2} \frac{M(v_1^2 - v_2^2)}{Nk} \qquad \text{(Eq. 4-8)}$$

$$V_w = \varphi K \frac{F_N L}{3} = \frac{KM}{6Nk}(v_1^2 - v_2^2) \qquad \text{(Eq. 4-9)}$$

Where,

- N is the number of brake assembly of each vehicle;
- k is friction coefficient;
- M is mass of vehicle;
- v_1 is velocity when the vehicle begins to brake;
- v_2 is velocity when the vehicle stop to brake.

$$m = \rho V_w = \varphi K \frac{F_N \rho L}{3} = \frac{K \rho \varphi M}{6Nk}(v_1^2 - v_2^2) \quad \begin{cases} \varphi = 1 & T_{pad} < 200°C \\ \varphi = 1.8 & 200°C \leq T_{pad} \leq 250°C \\ \varphi = 5.6 & T_{pad} > 250°C \end{cases} \qquad \text{(Eq. 4-10)}$$

Where,

- ρ is density of brake pad or brake disc;
- φ is coefficient regarding brake pad temperature.

We calculated the brake wear emissions of a reduced temperature-driven LACT using this mathematical model. A reduced temperature-driven LACT was developed by (Mathissen and Evans, 2019). The reduced LACT cycle consists of a sub-set (217 decelerations) of the n full LACT (3542 decelerations). The median initial velocity and decelerations of the reduced LACT cycle were chosen to be the same as for full LACT cycle. In the reduced LACT, the next deceleration starts when the rotor temperature is below a certain value. The brake wear emissions obtained from mathematical model and literature simulated data (Riva et al., 2019) are shown in Figure 4.14. It can be seen that these two results present similar evolution trend, indicating this mathematical model can well predict brake wear emissions.

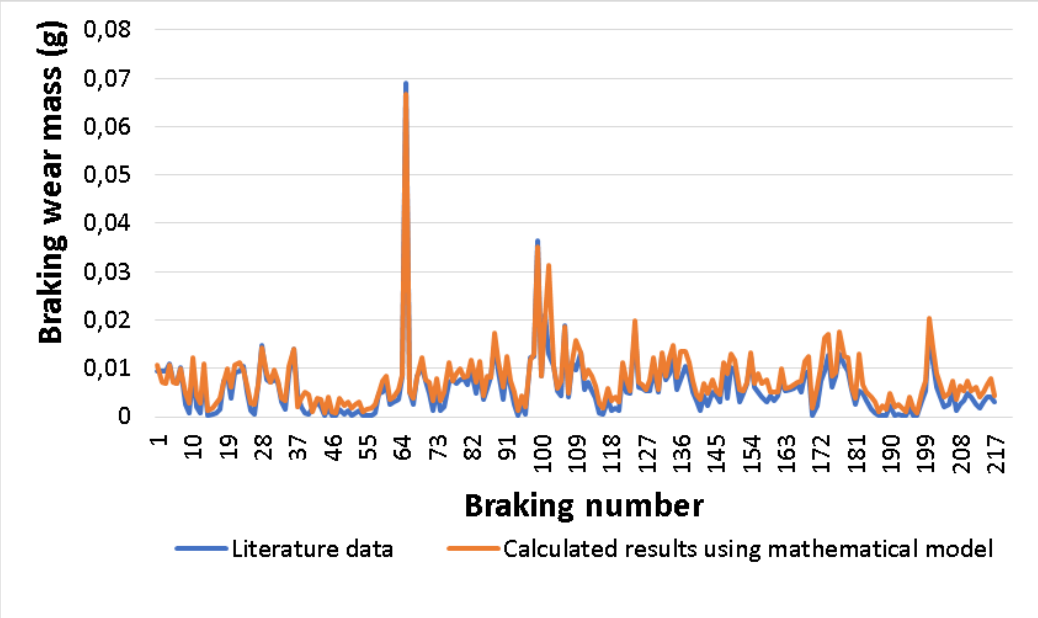

Figure 4.14: A comparison between the results of the mathematical mode and literature data for brake wear (Riva et al., 2019)

To assess the strength of the linear relationship between these variables, the linear correlation coefficient, R^2, was calculated by means of simple linear regression. The R^2 values are 0.92 between the brake wear emissions from the mathematical model and literature simulation data, as shown in Figure 4.15. In addition, the RMSE value is 1.2E-4. These data suggest that the data from mathematical model has a definite correlation with the literature simulation results. As a consequence, the mathematical model can total brake wear emissions accurately evaluate total brake wear emissions.

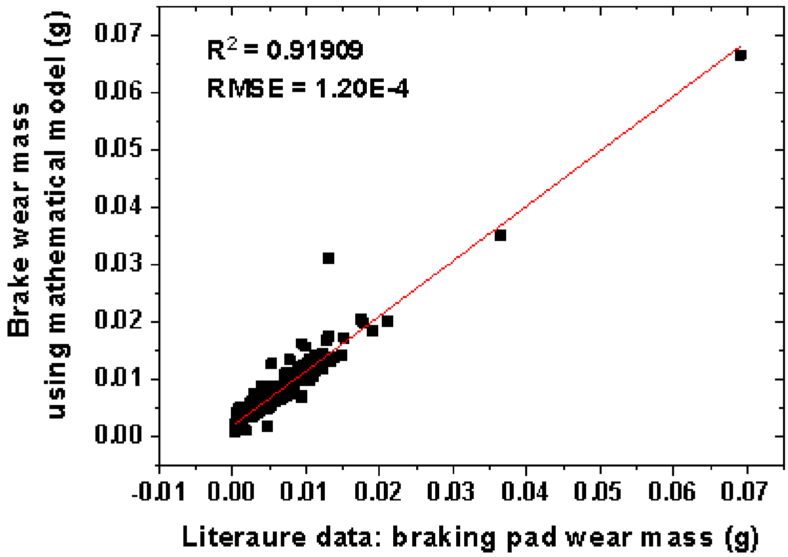

Figure 4.15: Brake wear emissions obtained from the mathematical model vs. literature data (Riva et al., 2019)

5 Simulation and modelling of tyre wear emissions

Among the composition components of an automobile tyre, the outer rubber layer called the tyre tread is composed of many grooves and blocks in complex pattern for the sake of major tyre running performances such as traction, braking, riding comfort, and the hydroplaning (Cho, J.R. et al., 2005). Contacting directly with ground within the postcard size of contact area, the tyre tread wears down owing to the inevitable frictional slip against the abrasive ground. This tyre wear not only degrades the tyre running performances and shorten the tyre lifetime but also becomes a crucial source of air pollution. In this connection, together with the recent worldwide intensification of the environmental protection regulation and the high-mileage warranty for tyre, the development of high wear-resisting tyre has become a great challenging subject to both tyre and car makers (Knisley, 2002; Koishi and Shida, 2006).

In general, the wear performance of a tyre that has been already manufactured has been traditionally evaluated either by outdoor tyre wear testing along a specified wear test course or using indoor wear testing system making use of a MTS machine equipped with the control system that reproduces the actual outdoor force conditions (Stalnaker and Turner, 2002). However, these experimental methods are impractical for the design of a new tyre model satisfying the target wear performance, because the need of a number of trial tyre productions and time-consuming wear tests cannot meet the design cycle times that are shortened in response to car maker requirements. In this context, a time- and cost-effective numerical technique for accurately predicting the tread wear amount is highly desired at the design stage.

On the other hand, the tread wear is influenced by many factors such as the material and structural compositions of tread, ground and loading/driving conditions, environmental conditions, and so on (Zheng, 2003). This implies that the reliability of wear amount and wear depth predicted by a numerical technique is strongly dependent on how accurately these conditions are taken into consideration. Thus, the essential considerations for the reliable wear prediction are the elaborate 3D detailed modelling (Cho et al., 2004) of the complex tyre material composition and the tread pattern blocks, a suitable wear model to correlate the frictional energy dissipation and the tread wear rate, the acquirement of driving and loading conditions exerted on the tyre during the actual outdoor wear test (Cho and Jung, 2007; Cho et al., 2004).

This chapter primarily focuses on the effect of driving behaviour on tyre wear emissions. Driving conditions in the actual outdoor wear test were extracted from the vehicle acceleration histogram (Zheng, 2003) and classified into nine representative driving mode with different force kinematic/ force conditions.

5.1 Simulation methodology

5.1.1 Simulation model description

Figure 5.1 shows a structure of radial automobile tyre, the tread part is composed of rubber blocks and grooves in complex pattern for the sake of traction, braking, hydroplaning, and so on. Since the frictional slip is on the abrasive ground, it is not too much to say that the tyre lifetime is determined by the tread wear performance. In general, the tread wear is characterized by the tread shape (called the crown contour) and the pattern blocks as well as the rubber compound properties, so that the development of high wear-resisting tyres can be achieved by appropriately designing these parameters (Cho, J. et al., 2005).

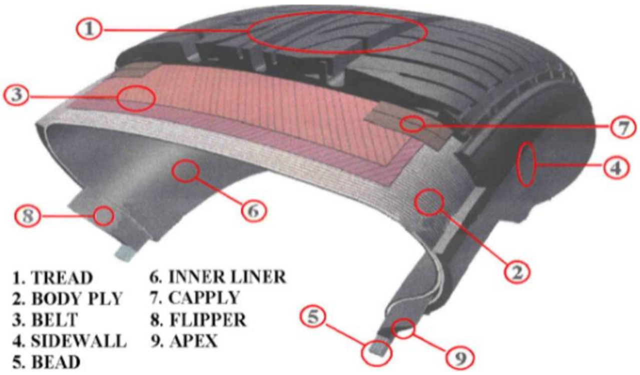

Figure 5.1: Structural compositions of car tyre

As it is well known, wear is classified largely into abrasive, corrosive, adhesive, and fatigue wears according to the wear mechanism, and generally two or more kinds of wears appear at the same time in a single wear phenomenon. The tread wear is characterized by the abrasion of rubber compound that is accompanied by the frictional energy dissipation through the tyre footprint. As a result, both the contact force and the slip distance within the tyre footprint area become key factors in the tread wear evaluation. However, both are not only non-uniform within the tyre footprint region but also influenced by many factors such as the crown shape, the tread pattern, the ground and loading conditions, the driver's driving style, and the environmental conditions.

The material composition of most tyres is distinguished largely into the fibre-reinforced rubber (FRR) parts and the remaining pure rubber part. The FRR parts of the tyre model considered here are composed of a single-ply polyester carcass, two steel belt layers, and several steel bead cords. Since the FRR parts are in the highly complex structure, their material models are chosen based on the goal of the numerical simulation. In the static tyre analysis, those parts are usually modelled using solid elements like rebar elements, and which does not make too much trouble in aspect of CPU time. However, in the dynamic tyre analysis this full modelling requires extremely long CPU time, so the FRR parts are modelled as either composite membrane or composite shell. In the current study, two belt layers in underlying rubber matrix and a carcass layer shield with inner liner are modelled using composite shells. On the other hand, steel cords and underlying rubber matrix in the bead region are modelled as homogenized solid by utilizing the modified rule of mixtures (Cho and Ha, 2001).

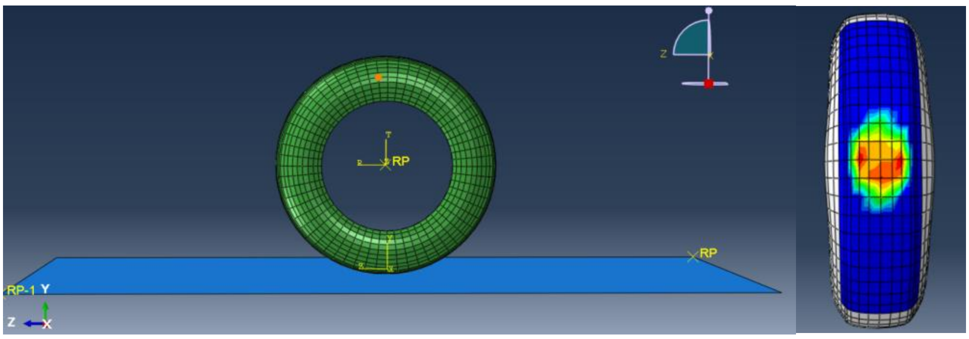

Figure 5.2: 3D physical model with patterned mesh

Figure 5.2 shows a 3D physical model with patterned mesh, including pure rubber solid, composite shell, and homogenized solid elements. Meanwhile, the tyre body and tread meshes have different mesh densities so that both are incompatible along the common interface. The tread and body meshes are separately generated at the beginning and then both are to be assembled by the incompatible surface-to-surface tying algorithm supported by ABAQUS (Manual, 2002).

5.1.2 Evaluation of tyre tread wear amount

While driving a vehicle, tyres are subjected to various dynamic forces and moments from the vehicle body and the ground, and most of them are transferred to the tyre axes. Meanwhile, the loading condition of a tyre depends largely on the driving condition of a vehicle, even though other factors such as the road and environmental conditions that are characterized by the steering (or slip) angle, cruising, acceleration, and braking are also involved (Zheng, 2003). From the tyre mechanics point of view, both the lateral force and the camber angle are strongly affected by the slip angle while the wheel torque displays the remarkable change to cruising, accelerating, and braking. In this context, we classify the tyre driving conditions into nine major modes: cruising, accelerating, and braking modes in the left, centre, and right directions, respectively.

On the other hand, the loading conditions, and the occurrence frequencies of individual driving modes in an actual wear test can be either measured directly from the outdoor test driving with the special instruments or extracted from the virtual simulation. For the numerical simulation to compute the frictional energy densities, the required conditions except for usual simulation parameters are vehicle velocity, lateral and vertical forces, wheel torque, camber and slip angle, and the occurrence weight corresponding to each driving mode.

We next describe how to estimate the tread wear amount of a patterned tyre under the specific wear test conditions. Let us denote $E_{F,tot}^{I}$ and A_i as the total frictional energy dissipation and the total contact area of tyre per revolution in the *i*-th driving mode, then the corresponding averaged frictional energy density E_F^I is calculated by

$$E_F^I = \frac{E_{F,tot}^{i}}{A_i}, i = 1, 2, \cdots, 9 \qquad \text{(Eq. 5-1)}$$

The corresponding volumetric wear rate per unit area of the tyre footprint in the *i*-th mode is calculated by

$$\dot{W}^{\iota}(\mathrm{m}^3/\mathrm{s\,m}^2) = 6C\left[E_F^i(\mathrm{J/m}^2)\right]^m, i = 1, 2, \cdots, 9 \qquad \text{(Eq. 5-2)}$$

As a result, the total volumetric wear amount $W_{rev}^{i}\,(\mathrm{m}^3/\mathrm{rev})$ of the tread rubber blocks per revolution in the *i*-th driving mode becomes

$$W_{rev}^{i} = \Delta t_i A_i \dot{W}^{\iota}, i = 1, 2, \cdots, 9 \qquad \text{(Eq. 5-3)}$$

Where:

- Δt_i denotes the time taken for a revolution of tyre.

We denote ω_i (0<ω_i<1) as the weighting factor that is defined by the relative occurrence frequency of *i*-th driving mode. Then, the total volumetric wear amount W_{tot} (m^3) of tyre tread after completing an actual outdoor wear test can be estimated by

$$W_{tot} = N(\omega_1 W_{rev}^1 + \omega_2 W_{rev}^2 + \cdots + \omega_9 W_{rev}^9) \qquad \text{(Eq. 5-4)}$$

with the total revolution number *N* of tyre. The final wear depth *H*(m) of tyre tread can be approximately calculated as

$$H = W_{tot}/A, \;\; A{=}\omega_1 A_1 + \omega_2 A_2 + \cdots + \omega_9 A_9 \qquad \text{(Eq. 5-5)}$$

Where:

- A denotes the weight-averaged total contact area of tyre per revolution.

5.1.3 Validation of simulation models

A non-symmetric patterned tyre P205/60R15 is considered for the numerical implementation of the proposed wear amount estimate. Tread rubber blocks are manufactured with carbon-black-filled polybutadiene and the width *b* is 205 mm. The frictional dynamic rolling analyses were performed by ABAQUS/Explicit code (Manual, 2002) and individual driving modes are implemented after the tyre reaches the steady-state dynamic rolling. Here, the steady state rolling of a tyre with the pre-set vehicle speed *V* is reached by a series of three sequential simulations: inflation up to the pre-set inflation pressure *p* contact with the ground by the action of vertical force F_V, and linear acceleration from rest to the desired uniform speed *V*.

The internal pressure *p* and the uniform vehicle speed *V* are given by 206.85 kPa and 60 km/h, and the frictional coefficient μ between tyre and ground and the penalty parameter k_p are set by 0.8 and 10 MPa, respectively, regardless of the driving mode. On the other hand, the remaining loading conditions are dependent on the driving mode and the values recorded in Table 5.1 are quoted from the paper by (Zheng, 2003). These values were extracted from the virtual simulation by utilizing the available vehicle acceleration histogram. The loading conditions for each driving modes are applied once the tyre reaches the steady-state dynamic rolling with the vehicle speed V of 60 km/h.

Table 5.1: Tyre loading conditions taken for nine representative driving modes

Driving mode	Vertical force, N	Lateral force, N	Torque, N m	Camber angle, °C
Left accelerating	4225.94	731.43	233.65	−0.2533
Left cruising	4474.24	671.91	32.82	−0.2506
Left braking	4576.59	842.05	−125.87	−0.4437
Centre accelerating	4800.82	−205.10	275.56	0.4228
Centre cruising	4942.08	−140.11	81.88	0.3380
Centre braking	5232.27	−88.78	−209.03	0.1911
Right[1] accelerating	5491.41	−1355.71	238.59	1.1481
Right cruising	5492.57	−1042.61	26.99	0.9103
Right braking	5725.42	−1178.19	−129.76	0.9358

Figure 5.3 shows the tyre wear emissions from the simulation and literature data. To validate the simulation results, the linear correlation coefficient, R^2, was calculated by means of simple linear regression. The R^2 value is 0.892 between the simulated tyre wear emissions and published literature

[1] Please note that these results are based on the **left** tyres which take on more force than the right counterparts when the vehicle goes around right curves, especially sweeping turns. Likewise, the **right** tyres take on more force than the left counterparts when the vehicle goes around left curves.

(Xu, 2014). The result indicates that simulation and literature results present a definite linear correlation, which agrees well with our simulation results.

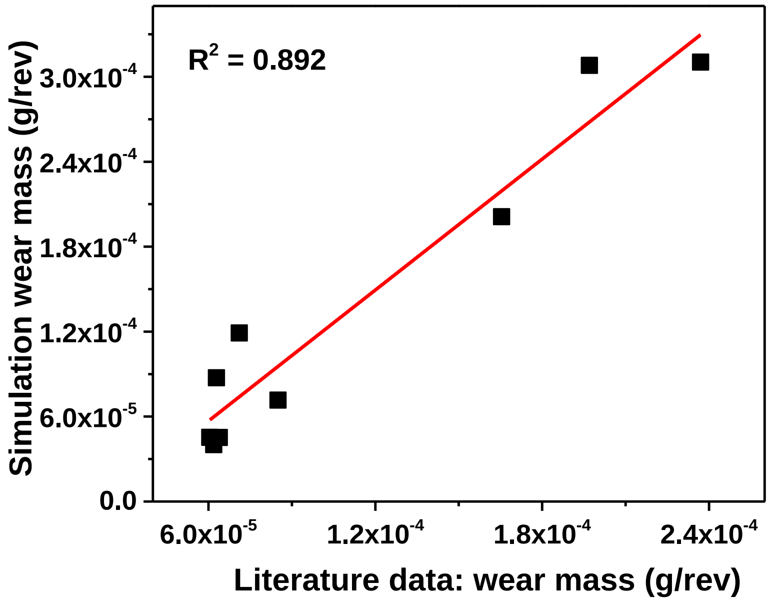

Figure 5.3: Tyre wear emissions from simulation and literature data

5.2 Effect of driving speed on tyre wear emissions

Under a steady lateral load of 3920 N, the left front tyre simulation was performed to generate tyre wear emissions at driving speeds of 40, 60, 80, 100 and 120 km/h. The total tyre wear emissions under various driving speed are shown in Figure 5.4.

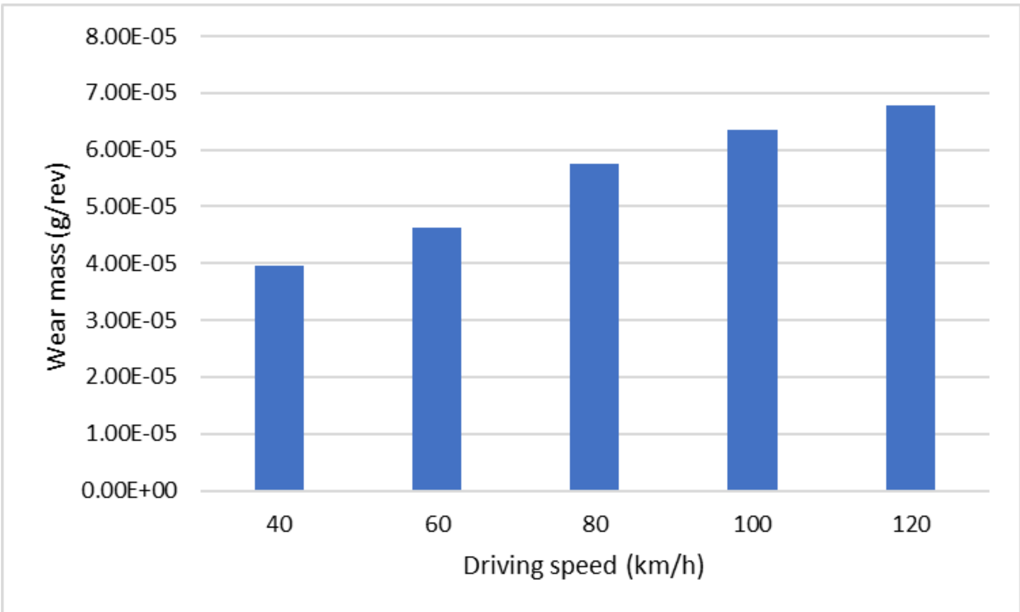

Figure 5.4: Tyre wear emissions as a function of driving speed

The total tyre wear mass tends to increase as the driving speed increases. The increase rate from 40 to 80 km/h is larger than that from 80 to 120 km/h. The total tyre wear emissions were positively correlated with driving speed. Tyre wear emissions are known to be generated by shearing forces

(Kreider et al., 2010) and through volatilization (Mathissen et al., 2011). The former mechanism predominantly results in coarse particles, whereas the latter generates smaller fine particles through the evaporation of volatile content. When the harsh braking of driving vehicle does not occur, the shear stress acting on the tyre surface was limited, while the volatilization process became relatively dominant at the high speeds produced. As a result, compared to PM_{10} particles, $PM_{2.5}$ particles were generated more. In a study of by (Kim and Lee, 2018), they found that $PM_{2.5}/PM_{10}$ ratio increased as the driving speed increased. That is, fewer PM_{10} and more $PM_{2.5}$ particles were generated.

In addition, they reported that driving speed appeared not to significantly affect the tyre wear mass size distribution, whereas its concentration tended to increase with elevated driving speed. The same conclusion has been reached by (Grigoratos et al., 2018), who pointed out that the tread-wear rating seemed not to affect the shape of mass size distributions of tyre wear particles. (Hussein et al., 2008) and (Kwak et al., 2013) reported unimodal tyre wear mass size distributions with mode diameters of 2−3 μm and 3−5 μm, respectively. However, (Kim and Lee, 2018) found that the tyre wear mass concentrations observed were relatively low compared to other literature mentioned above, which is possibly due to the effects of background particles or differences in experimental methods.

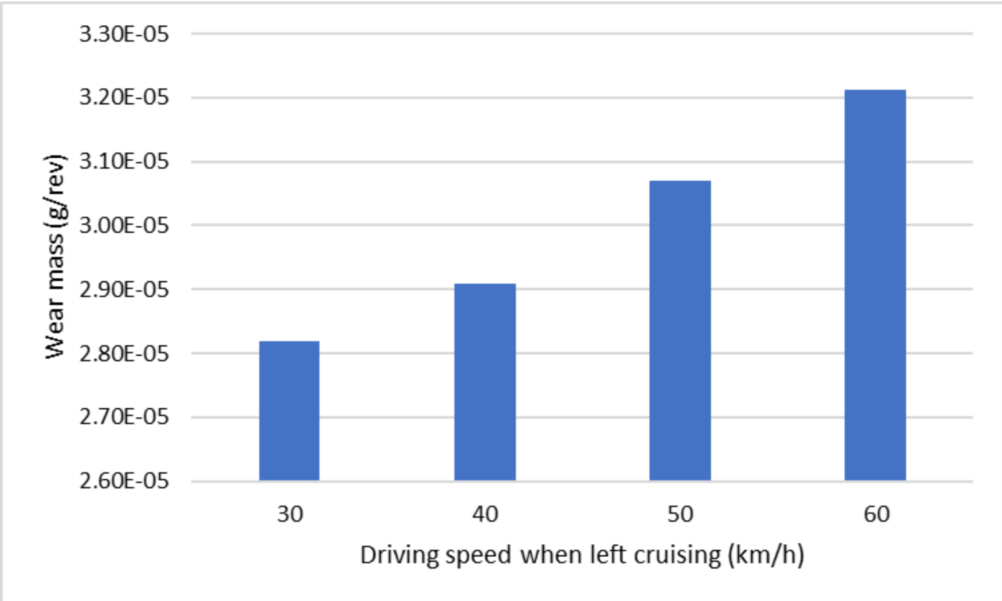

Figure 5.5: Left tyre wear emissions as a function of driving speed when left cruising

5.3 Effect of deceleration rates on tyre wear emissions

Under a steady lateral load of 3920 N, the left front tyre simulation was performed to generate tyre wear emissions at deceleration rates of 0.5, 1, 1.5, and 2 m/s^2 when straight braking with initial braking speed of 60 km/h.

Figure 5.6 shows tyre wear emissions as a function of deceleration rates when straight braking. An exponential increase in tyre wear emissions was observed, indicating that tyre wear emissions increase significantly with the braking intensity. Similar finding was reported by (Lee et al., 2013), who measured the tyre wear emissions on real road with rapid deceleration rate of full stop braking was 2.6 m/s^2. They revealed that upon rapid deceleration, a large quantity of particles was generated when compared to constant speed conditions.

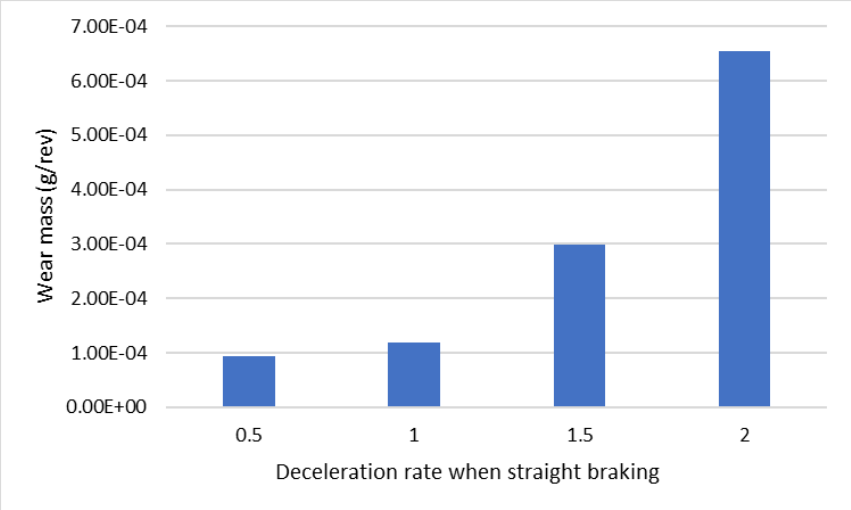

Figure 5.6: Left tyre wear emissions as a function of deceleration rates when straight braking

However, it is worth mentioning that the authors have mentioned whether the source of particles at the peak value came from tyre-road interface or from brake pad because the particle sampling was conducted at the tyre-road interface only. (Kim and Lee, 2018) stated that the deceleration rates could exert a significant impact on tyre wear emissions and found that the concentration of tyre wear emission increased with both braking intensity and speed.

Figure 5.7 shows the tyre wear emissions as a function of deceleration rates when right braking with initial speed of 40 km/h. Under a steady lateral load of 3920 N, the left front tyre simulation was performed to generate tyre wear emissions at deceleration rates of 0.5, 1, 1.5, and 2 m/s^2. Although the initial speed is smaller than that in Figure 5.6, the tyre wear emissions is larger relative to that at the same deceleration rates. In addition, the tyre wear emissions also present a similar trend as the deceleration rate increases. (Mathissen et al., 2011) performed the measurement of tyre wear particles using an instrumented sport utility vehicle equipped with summer tyres. The experimental results showed that harsh braking would generate more ultrafine particles from tyre wear.

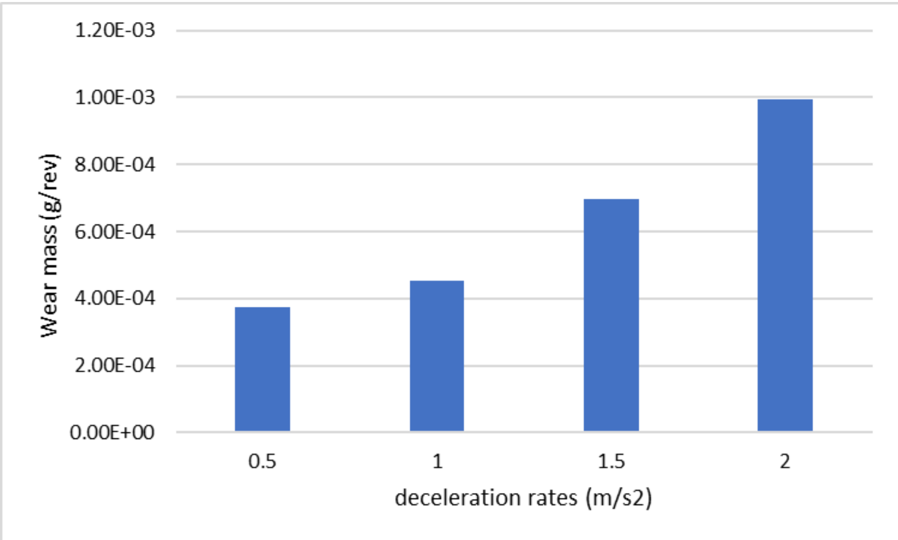

Figure 5.7: Left tyre wear emissions as a function of deceleration rates when right braking

Figure 5.8 shows tyre wear emissions as a function of deceleration rates with the initial speed of 40 km/h when left braking. Under a steady lateral load of 3920 N, the left front tyre simulation was performed to generate tyre wear emissions at deceleration rates of 0.5, 1, 1.5, and 2 m/s^2. In this case, the tyre wear emissions are the least compared to when right and straight braking. This phenomenon is because the centre of vehicle deviates to the right tyre, which in turn, leads to the reduction in tyre wear emissions.

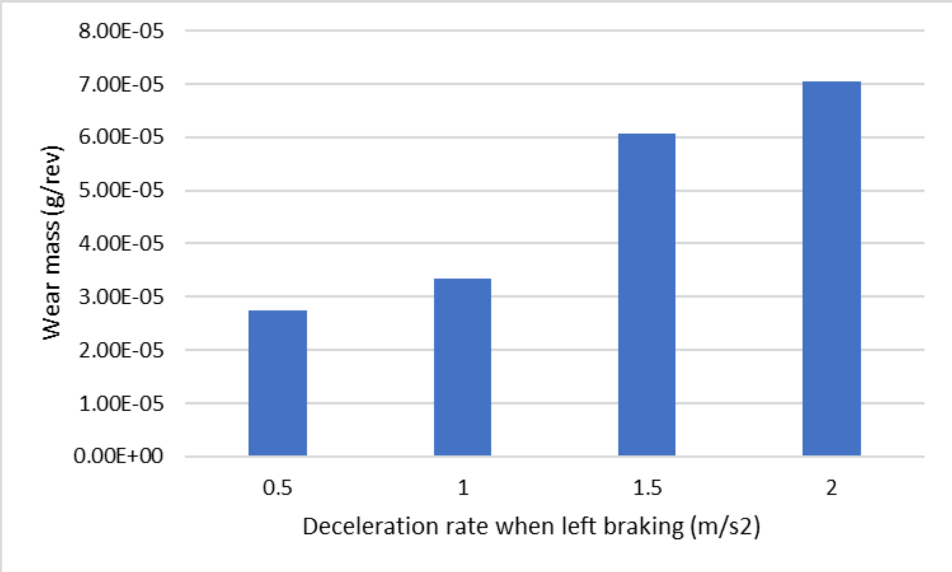

Figure 5.8: Left tyre wear emissions as a function of deceleration rates when left braking

5.4 Effect of acceleration rates on tyre wear emissions

Under a steady lateral load of 3920 N, the left front tyre simulation was performed to generate tyre wear emissions at driving speeds of 60 km/h with acceleration rates of 1.3, 1.6, 1.9 and 2.2 m/s^2. Figure 5.9 shows the total tyre wear emissions under various acceleration rates.

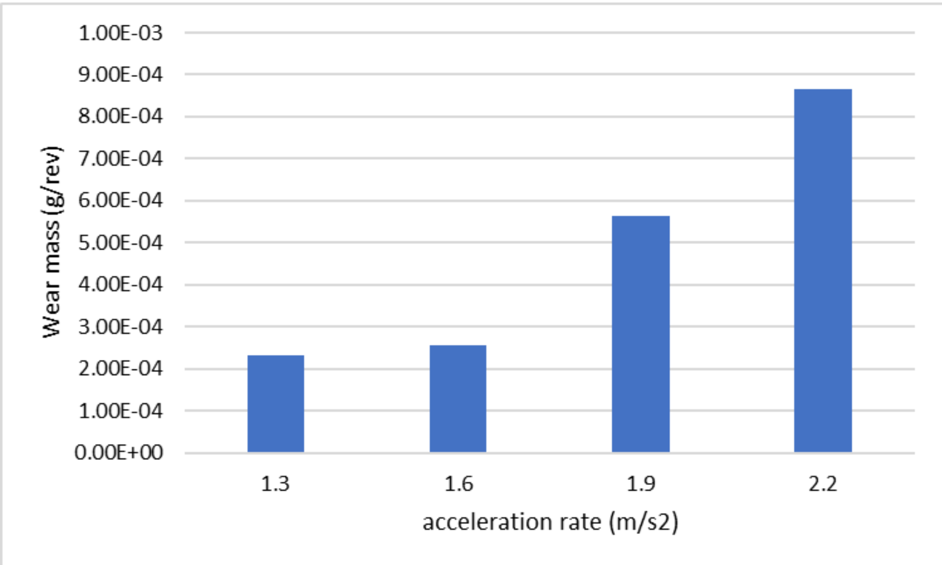

Figure 5.9: Left tyre wear emissions as a function of acceleration rates when straight accelerating

It can be seen in Figure 5.9 that the total tyre wear mass presents a similar exponential growth. (Beji et al., 2020) reported that the higher speeds and during the most intense accelerations would lead to a strong increase in emissions. In addition, they figured out that tyre wear emissions were mostly in the <0.1 µm range by number, with an accumulation mode centred at 0.2–0.3 µm and a major coarse mode centred at 2–4 µm by mass. The strongest accelerations (>2.50 m/s^2) favoured the production of particles smaller than 0.1 µm, while higher speeds and heavy high-speed decelerations increased the rate of coarse particles.

Under a steady lateral load of 3920 N, the left front tyre simulation was performed to generate tyre wear emissions at driving speeds of 20 km/h with left acceleration rates of 1.3, 1.6, 1.9 and 2.2 m/s^2, and the results of total tyre wear emissions are presented in Figure 5.10. It can be observed that the total tyre wear mass increases as the left accelerating rates rise. Compared to the results in Figure 5-9, the total tyre wear emissions are observed to be emitted less. As a result, the tyre wear emissions are associated with not only acceleration rates but also driving speed when accelerating. Similar finding was reported by (Beji et al., 2020), who found that tyre wear emission could be significantly lower in urban areas and remote suburban roads. They attributed primarily this finding to the lower driving speeds and numerous idling periods associated with urban driving. The limited emissions for remote suburban roads can be explained by a combination of moderate speeds (around 50 km/h) and frequent sweeping or vacuuming of the pavement.

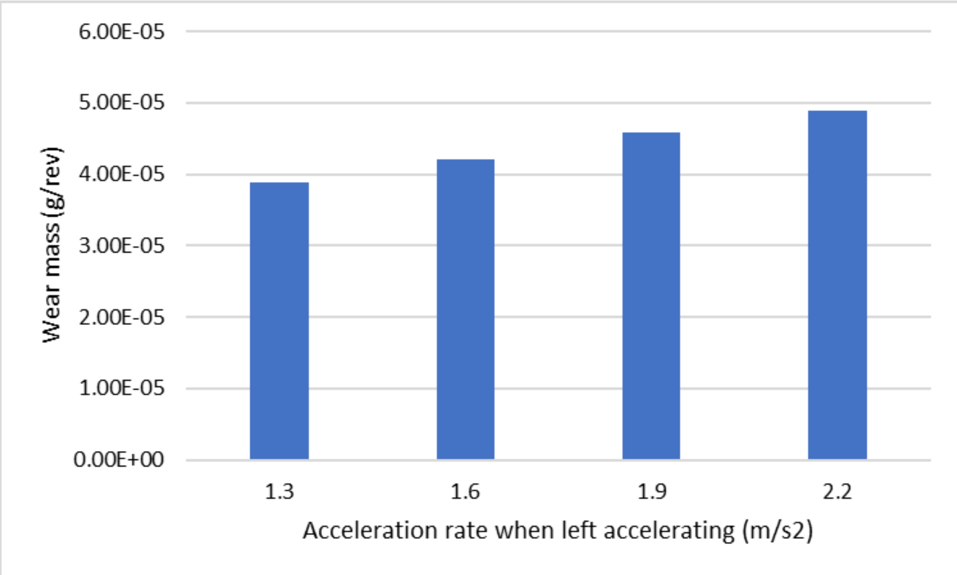

Figure 5.10: Left tyre wear emissions as a function of acceleration rates when left accelerating

5.5 Mathematical model of tyre wear emissions

According to the reported literature (Cho et al., 2011; Lupker et al., 2004), the frictional power per unit contact area vs. mass loss per unit covered area relation may be approximated by the following expression:

$$m_T = \varphi k_1 (w)^{k_2} BD \qquad \text{(Eq. 5-6)}$$

$$w = \frac{P(t)}{\varphi NBL} \qquad \text{(Eq. 5-7)}$$

Where,

- m_T is the mass loss;
- φ is the transverse reduction coefficient due to the tyre pattern;
- w is the frictional power per unit contact area;
- k_1 and k_2 are two constants that characterize the wear behaviour of the rubber compound at a given temperature and on a given abrasive surface;
- B is contact width between tyre and ground and D is the driven distance of vehicle;
- N is the number of tyre of the vehicle; L is the contact length between tyre and ground;
- $P(t)$ is the energy consumption.

The $P(t)$ can be obtained from the equation below according to the literature

$$P(t) = \frac{1}{3600\eta_d}\ v(t)\left\{\frac{\rho}{25.92}C_D C_h A_f v(t)^2\ + \frac{g\ M\ C_r}{1000}[c_1 v(t) + c_2] + g\ M\ G(t) + (1+\lambda)\ M\frac{dv}{dt}\right\}$$

(Eq. 5-8)

Where,

- C_h is altitude;
- g is gravity;
- ρ is air density;
- $G(t)$ is slope;
- M is vehicle weight;
- A_f is vehicle frontal area;
- C_D is aerodynamic drag coefficient;
- C_r is rolling resistance factor;
- c_1 and c_2 are rolling parameters;
- η_d is driveline efficiency;
- λ is Rotl masses.

6 Multi-objective optimisation

Driving style, road geometry, and surrounding traffic conditions have a significant impact on a vehicle's fuel consumption and emissions. Often, drivers are not aware of the optimal speed profile for a given route that will well balance the consumed fuel and pollutants emitted. Moreover, the global optimal speed profile depends on many other factors such as driver's safety and comfort, surrounding traffic conditions and road conditions such as slope. In most previous research, the optimal speed profile of a vehicle is generated under the consideration of a single objective (e.g. eco-driving) plus some other necessary or auxiliary requirements as aforementioned. For instance, in Jia et al (2021), a time-varying adaptive model predictive control (MPC) model is proposed to calculate the instantaneous optimal speed profile with the main aim of minimizing energy consumption.

In this section, the possibility in considering multiple objectives to simultaneously optimise several factors, such as energy consumption, and emissions from several pollutants such as NOx, COx and PMs is investigated. Based on Jia's MPC model, a multi-objective model is proposed by adding extra terms in the objectives and constraints to reflect the consideration in minimising emissions together with energy consumption and other factors such as safety and comfort requirements. Some preliminary experiment results are also given and compared to previous results in Jia et al (2021).

The investigation in the direction of multi-objective optimisation is still ongoing and more sophisticated modelling strategies such as Pareto front will be explored in future work such that a set of results corresponding to different trade-offs among the objective terms can be generated for the user to choose based on his/her preferences.

6.1 Previous work

In this section, the previous work reported in Jia et al (2021) is briefly introduced. Our newly developed model is based on this work.

Predictive cruise control (PCC) is a powerful approach to optimising energy consumption of vehicles. Traditional PCC systems can only get a sub-optimal speed profile based on a shorter prediction horizon. The recently emerging IT and computing technologies such as vehicular communication, cloud computing, and Internet of Things (IoT) provide great potentials in improving the conventional PCC systems.

In Jia et al (2021), a general framework for the enhanced cloud-based PCC system is proposed, which integrates a data-driven traffic predictive model and instantaneous control algorithms. The authors introduce a novel multi-view convolutional neural network (CNN) deep learning algorithm to forecast traffic situation based on both historical and real-time traffic data collected from fields, and a time-varying adaptive model predictive control (MPC) to obtain the instantaneous optimal speed profile such that the energy consumption is minimised. This approach is verified via simulations (by SUMO[2]) in which the impact of various traffic condition on the PCC-enabled HDV has been fully evaluated. Numerical experiments based on the road and traffic data in one segment of the UK M25 motorway were conducted and show the usefulness of this approach.

[2] Available: https://sumo.dlr.de/index.html

6.1.1 Jia's MPC model

The MPC model presented in Jia et al (2021) is elaborated in this sub-section. The main objective of this model is to find the optimal speed profile that minimises fuel consumption subject to several physical dynamics and safety constraints. Other objectives such as driver's comfort and synchronisation with surrounding traffics (predicted by the CNN deep learning algorithm) are also included as secondary terms to optimise. The overall form of the MPC model can be summarised as:

Min	*Fuel consumptions (+ sync with surrounding traffic + driver comfort)*
Subject to	*Vehicle dynamics*
	Physical constraints
	Safety constraints

To suit the MPC's principle, the entire route is discretised into many intervals in distance, indexed by i. Each time, a problem instance of the MPC model is solved within an interval i and its results are used as the input of the MPC problem instance of the next interval. This is because the model needs the information of the surrounding traffic in real-time to minimise the difference between the vehicle's speed and the desired speed given either as the average speed of the surrounding traffic or predicted by the CNN algorithm. The fuel consumption in the objective is numerically represented by the vehicle's engine energy $E_e(i)$.

A more detailed mathematical formulation of the MPC model in Jia et al (2021) is:

$$\min \quad J(i) = \lambda_e \sum_{j=i}^{i+n_p-1} E_e(i)^2 + \lambda_k \sum_{j=i}^{i+n_p-1} \left[E_k(i) - \frac{1}{2} M_e v_d^2(i)\right]^2 + \lambda_s \sum_{j=i}^{i+n_p-1} [E_e(i) - E_e(i-1)]^2$$

(Eq. 6-1)

Subject to

$$E_k(i+1) = A(i)E_k(i) + [E_e(i) - E_b(i)] - D(i) \qquad \text{(Eq. 6-2)}$$

where,

$$A(i) = 1 - \frac{\rho(i) A_f C_d(i) \Delta s}{M_e} \qquad \text{(Eq. 6-3)}$$

$$D(i) = [M_v g C_r(i) \cos\theta(i) + M_v g \sin\theta(i)] \cdot \Delta s \qquad \text{(Eq. 6-4)}$$

$$\frac{1}{2} m v_{\min}^2 \leq E_k \leq \frac{1}{2} m v_{\max}^2 \qquad \text{(Eq. 6-5)}$$

$$0 \leq E_e \leq \frac{\eta \gamma_g T_e^{\max}}{R_w} \Delta s \qquad \text{(Eq. 6-6)}$$

$$-\frac{T_b^{max}}{R_w} \Delta s \leq E_b \leq 0 \qquad \text{(Eq. 6-7)}$$

$$\gamma_g = \text{Const.} \qquad \text{(Eq. 6-8)}$$

where,

- i is the index of intervals
- $J(i)$ is sum of cost to be minimised for interval i;
- $E_e(i)$ is engine energy;
- $E_k(i)$ is kinetic energy;
- $E_b(i)$ is braking energy;
- M_e is effective mass (including inertia);
- M_v is vehicle mass;
- v_d is desired speed (from surrounding traffic);
- ρ is air density
- A_f is vehicle frontal area;
- C_d is aerodynamic drag coefficient;
- C_r is rolling resistance factor;
- g is gravity acceleration
- θ is road grade
- v_{min}, v_{max} are minimum and maximum speed
- η is transmission efficiency
- γ_g is gear ratio
- T_e^{max} is maximum engine torque
- T_b^{max} is maximum brake torque
- R_w is tyre radius

The model also has other constraints on safety and headway which are omitted here.

The first term in the objective represents the engine energy, while the second and third for surrounding traffic and driver comfort. Note that all objective terms should be quadratic as the MPC model is solved by a quadratic solver in MATLAB's MPC control toolbox.

6.1.2 Results from Jia's model

The results of the MPC model for generating speed profiles from Jia et al (2021) are summarised here. A traffic simulator SUMO was used for generating traffic demands at different levels, including free traffic, congested traffic, and accidents. One segment of the UK M25 motorway integrated with its elevation information was chosen as the target route in the experiments. Three target speed policies were used in determining the desired speed v_d as in the MPC formulation:

(1) Constant speed policy (CSP) where the vehicle tries to keep its speed at a recommended value of 25 m/s, regardless of the surrounding traffic
(2) Average speed policy (ASP) where the vehicle tries to follow the real-time average speed of its preceding and vehicles, and
(3) Predicted speed policy (PSP) where the vehicle is provided with the traffic speed profile of future distance steps obtained from the CNN traffic speed prediction and road condition ahead.

Both free traffic and heavy traffic conditions were tested against the above three policies. Under free traffic conditions, since there is no surrounding traffic, all three policies gave the same speed profile aiming to reach 25 m/s. Further experiments were conducted to let the weight on surrounding traffic synchronisation (λ_k) be different values. The results on free traffic conditions are given in Figure 6.1.

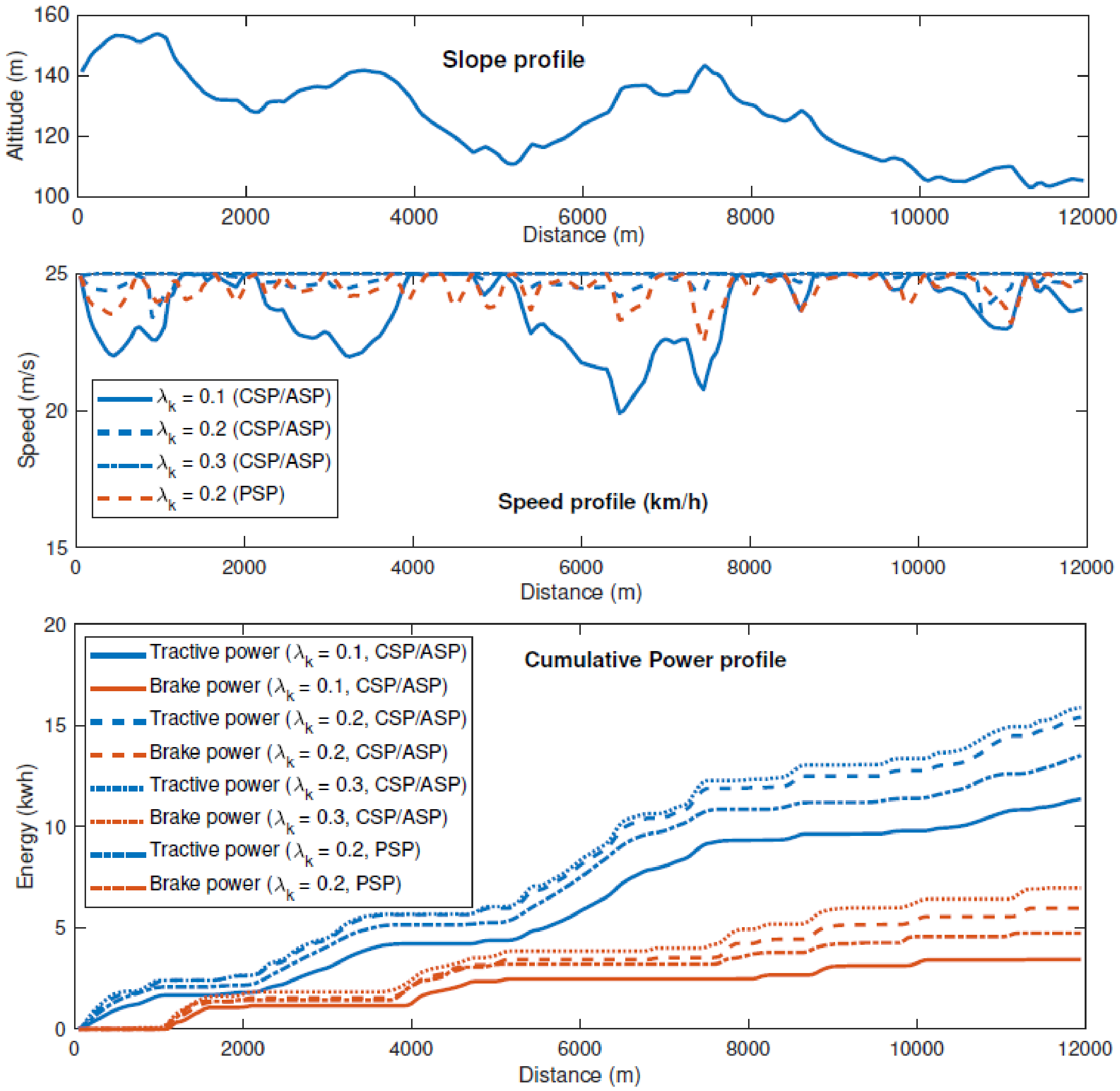

Figure 6.1: Results of speed/power profiles under free traffic conditions (Jia et al, 2021)

Experiments on heavy traffic conditions were also conducted. In this case, the speed profiles showed different patterns with the same weight settings against the three policies. Figure 6.2 gives the results from heavy traffic conditions.

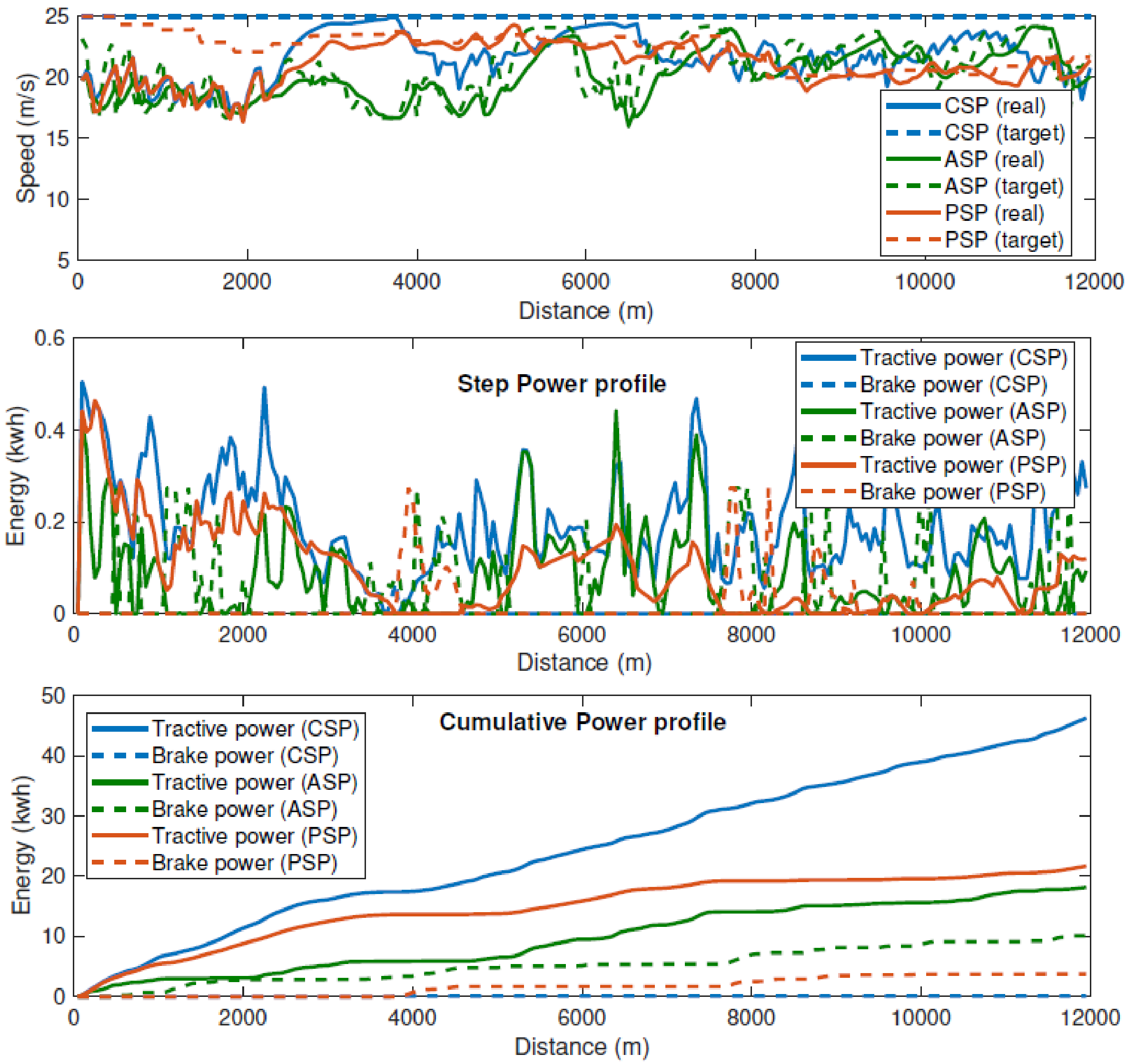

Figure 6.2: Results of speed/power profiles under heavy traffic conditions (Jia et al, 2021)

6.2 Modification on Jia's energy model for vehicle emissions

In this section, a modified MPC model based on the MPC model from Jia et al (2021) is presented where in the objective the original term on minimising the engine energy $\sum E_e(i)^2$ is replaced by a new term on pollutant emissions. The results from this modified MPC model are summarised and compared with the results from Jia et al (2021). The new term is a combination of several pollutants based on the empirical numeric relations between engine and NOx, and then to link the emission of other pollutants by their unified monetary values associated with NOx. It also has the ability to solve problems with a more MOOP flavour by including the original fuel term in the objective.

6.2.1 Relation between engine energy and NOx emissions

Based on the results from the earlier chapters of this deliverable, the relation between engine energy and NOx emissions can be described by Figure 6.3.

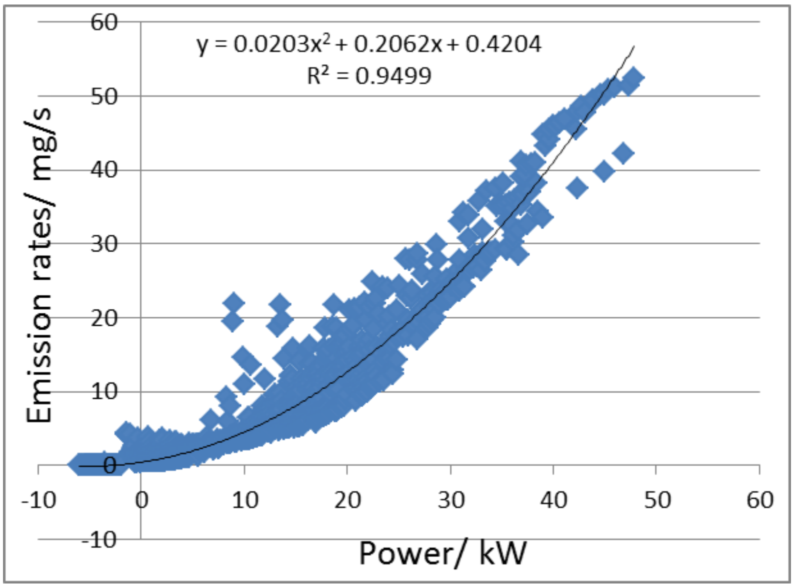

Figure 6.3: The relationships between vehicle power and emissions (all the data based on WLTC)

Based on Figure 6.3, the resultant numerical relation between NOx emission (P_N) and engine energy (E_e) can thus be expressed by the following formula

$$P_N = 0.0203E_e^2 + 0.2062E_e + 0.4204 \qquad \text{(Eq. 6-9)}$$

No data of similar relations between engine energy and the other pollutants (i.e. $PM_{2.5}$, PM_{10}, NH_3 and VOC) are available at the moment. To link the emission values of the other pollutants to engine energy, monetary values (unified costs in Sterling pound per unit amount) are used to link all pollutants under the same metric, including NOx. The details in the monetary values are given in Table 6.1 (Liu et al 2021). Note that the values were further processed such that the adjusted monetary value of NOx is 1.

Table 6.1: Mean monetary values for pollutants emitted

Pollutants emitted	Mean monetary value (£/tonne)	Equivalent in euro (€/tonne)[3]	Adjusted values
$PM_{2.5}$ from road transport	81,518	95 141	8.991617
PM_{10} from road transport	54,862	64 031	6.051401
NOx from road transport	9,066	10 581	1
NH_3	7,923	9 247	0.873925
VOC	102	119	0.011251

[3] Using 28 August 2021 exchange rate

6.2.2 MPC model on emissions

Based on Jia et al (2021), the modified MPC model can be summarised as:

Min	*Fuel consumptions (with 0 weight in experiments) + pollutant emissions (+ sync with surrounding traffic + driver comfort)*
Subject to	*Vehicle dynamics*
	Physical constraints
	Safety constraints

The detailed objective of the modified model is given as:

$$
\begin{aligned}
\min \quad J(i) = {} & \lambda_e \sum_{j=i}^{i+n_p-1} E_e(i)^2 \\
& + \lambda_k \sum_{j=i}^{i+n_p-1} \left[E_k(i) - \frac{1}{2} M_e v_d^2(i)\right]^2 \\
& + \lambda_s \sum_{j=i}^{i+n_p-1} [E_e(i) - E_e(i-1)]^2 + \lambda_N \sum_{j=i}^{i+n_p-1} [aE_e(i)^2 + bE_e(i) + c]
\end{aligned}
$$

(Eq. 6-10)

Note the newly added term for emissions in the end where λ_N is the weight for emissions. Some transformation is needed in the modified model with NOx and other emissions to merge the λ_e term with the λ_N term. By only focusing on the expressions inside Σ, the terms are converted to:

$$
\begin{aligned}
& \lambda_e E_e^2 + \lambda_N(aE_e^2 + bE_e + c) = (\lambda_e + \lambda_N a)E_e^2 + \lambda_N bE_e + \lambda_N c \\
& = \lambda_N \left[\left(\frac{\lambda_e}{\lambda_N} + a\right) E_e^2 + bE_e + c\right] \xRightarrow{\frac{\lambda_e}{\lambda_N} + a := a'} \lambda_N a' \left(E_e + \frac{b}{2a'}\right)^2 + \text{Const.}^4 \\
& \xRightarrow{E_e' = E_e + \frac{b}{2a'}} \lambda_N a'(E_e')^2 + Const.
\end{aligned}
$$

(Eq. 6-11)

Let $E_e' = E_e + \frac{b}{2a'}$ be a new decision variable (replacing E_e), the original objective $J(i)$ is transformed into (dropping the constant term):

$$
\begin{aligned}
\min \quad J(i) = {} & \lambda_N a' \sum_{j=i}^{i+n_p-1} E_e'(i)^2 \\
& + \lambda_k \sum_{j=i}^{i+n_p-1} \left[E_k(i) - \frac{1}{2} M_e v_d^2(i)\right]^2 + \lambda_s \sum_{j=i}^{i+n_p-1} [E_e'(i) - E_e'(i-1)]^2
\end{aligned}
$$

[4] Const. = $\lambda_N(c - \frac{b^2}{4a'})$.

(Eq. 6-12)

To solely minimise emission plus surrounding traffic synchronisation and driver comfort, let $\lambda_e = 0$ in defining the new objective terms. Subsequent constraints are transformed into:

Vehicle dynamics:

$$E_k(i+1) = A(i)E_k(i) + B(i)U'(i) - D'(i)$$

(Eq. 6-13)

where,

$$A(i) = 1 - \frac{\rho(i)A_f C_d(i)\Delta s}{M_e}, B(i) = [1 \quad -1]$$

(Eq. 6-14)

$$U'(i) = \begin{bmatrix} E_e{}'(i) \\ E_b(i) \end{bmatrix}, \qquad D'(i) = D(i) + \frac{b}{2a'}$$

(Eq. 6-15)

$$D(i) = [M_v g C_r(i)\cos\theta(i) + M_v g \sin\theta(i)] \cdot \Delta s$$

(Eq. 6-16)

NOx pollution emission level constraints:

$$P_N^{min} \leq P_N \leq P_N^{max} \qquad \text{(Eq. 6-17)}$$

Physical constraints:

$$\frac{1}{2} m v_{\min} \leq E_k \leq \frac{1}{2} m v_{\max} \qquad \text{(Eq. 6-18)}$$

$$0 \leq E_e' - \frac{b}{2a'} \leq \frac{\eta \gamma_g T_e^{\max}}{R_w} \Delta s \qquad \text{(Eq. 6-19)}$$

$$-\frac{T_b^{max}}{R_w} \Delta s \leq E_b \leq 0 \qquad \text{(Eq. 6-20)}$$

$$\gamma_g = \text{Const.} \qquad \text{(Eq. 6-21)}$$

Other constraints on safety and headway large remain the same as in Jia et al (2021) so they are omitted here.

6.2.3 Experiment results on the modified MPC model

The same types of experiments as in Jia et al (2021) were conducted by replacing the original MPC model only emphasises fuel consumption with our modified model that emphasises on pollutant emissions. The same speed control policies were used, i.e. (1) Constant speed policy (CSP), (2) average speed policy (ASP) and (3) predicted speed policy (PSP). Both free and heavy traffic scenarios were considered. The weight on emissions λ_N is set as 2.5 to give emission terms a higher priority.

The experiments were based exactly on the same road (UK M25) and same traffic and road conditions simulated by SUMO as in Jia et al (2021).

The results of free traffic and heavy traffic are summarised in Figure 6.4 and Figure 6.5, respectively.

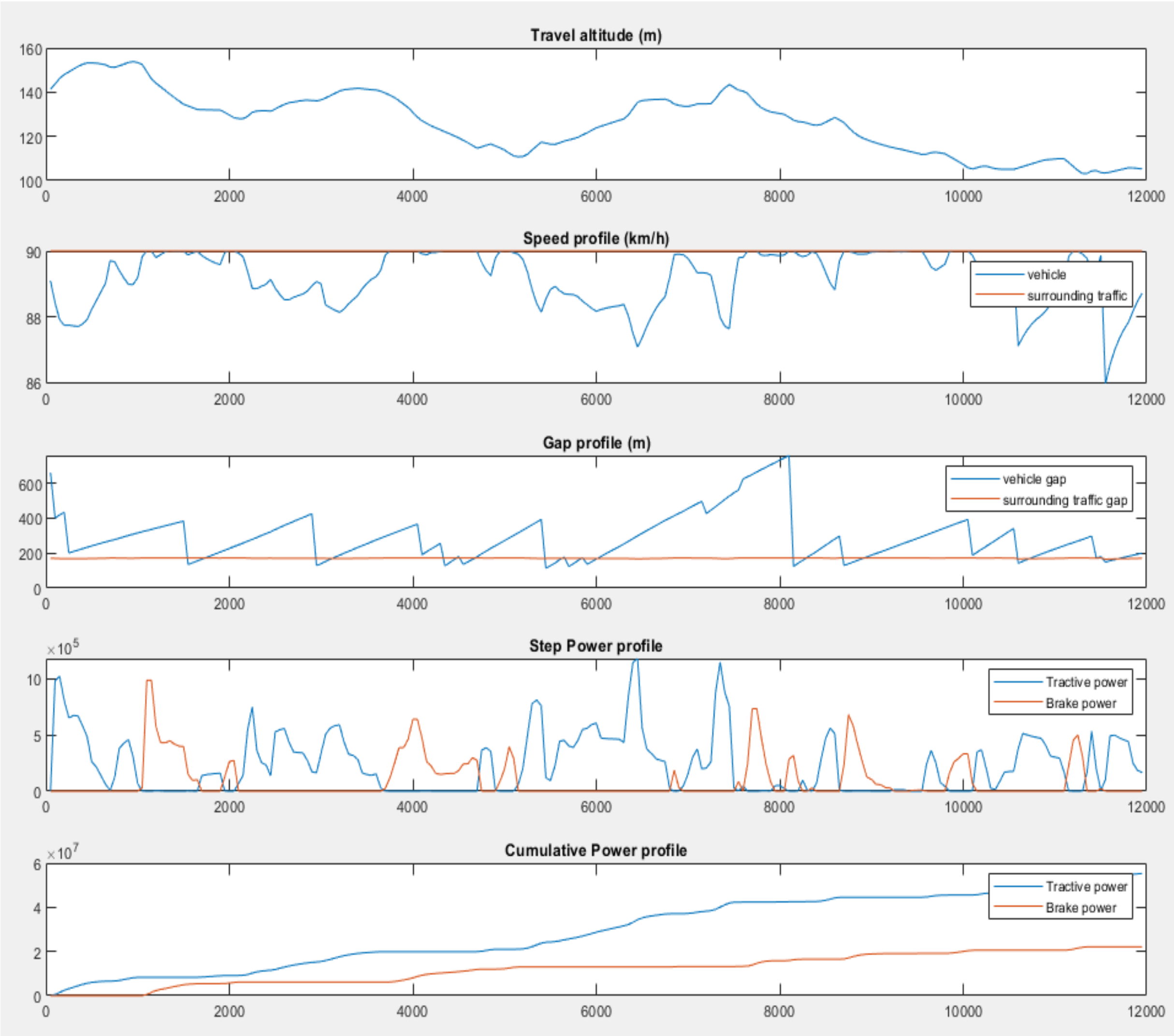

Figure 6.4: Results of the modified MPC under free traffic conditions

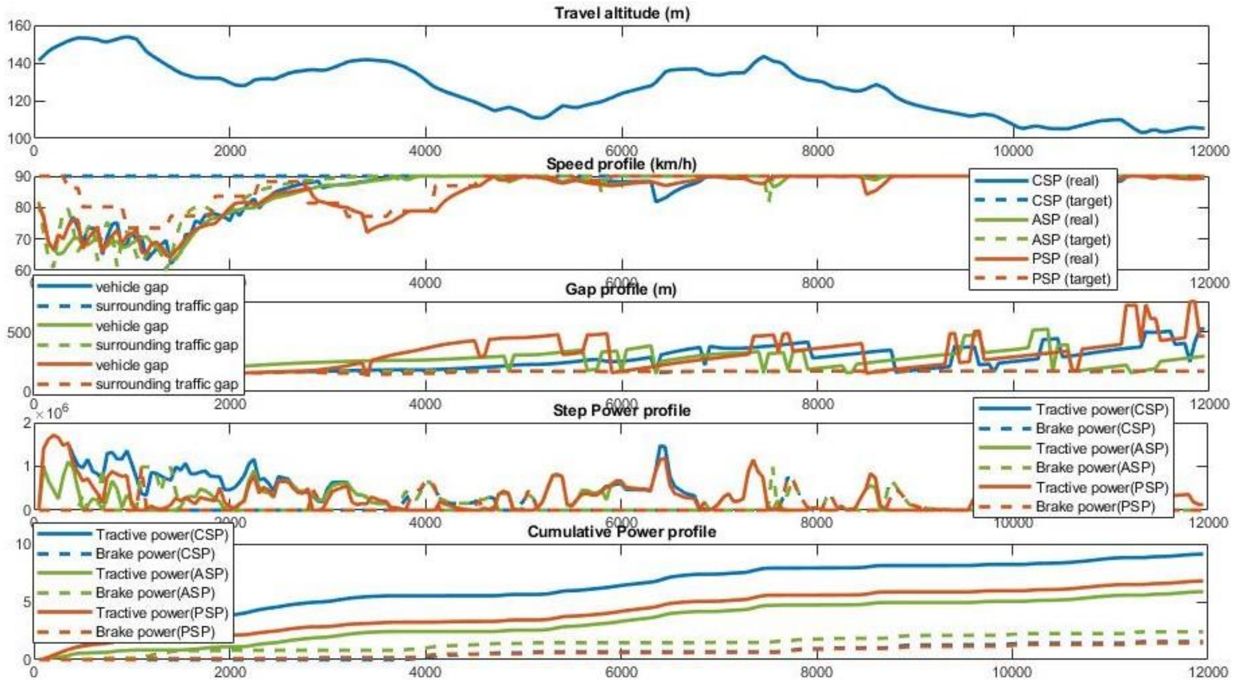

Figure 6.5: Results of the modified MPC under heavy traffic conditions with three policies

Comparing the results of the ***free traffic*** instance between the original MPC minimising fuel (as shown in Figure 6.1) and the modified MPC minimising emissions (as shown in Figure 6.4) with the same weight on speed deviation ($\lambda_k = 0.2$) , it can be observed that the speed profile patterns are rather similar for most sections on the route. This is probably because the strongly positive correlation between the engine energy and NOx emission shown by Figure 6.3. On the other hand, at the later stages roughly after 10000 metres, the speed profile of the emission-focused model shows a tendency of lower velocities including the global minimum speed values over the entire journey. On the contrary, in the speed profile generated from the fuel-focused model, such a pattern at the later stages is not seen and the lowest speed values appear approximately in the middle parts of the journey.

The results of the ***heavy traffic*** instance between the two MPC models under the policies of CSP, ASP and PSP were also analysed and compared. A common pattern in the speed profiles generated by all the three polices in the emission-focused model is that both the vehicle speed and target speed begin to significantly converge to the default speed of 90 km/h roughly after the middle point of 5000 metres. In other words, all speed curves, in all policies and both desired and actual, will converge to the default maximum value in the second half of the journey. However, this pattern is not seen from the results given by the original model minimising fuel, where the speed profile curves show constant deviation from the default speed at the top (except CSP, where the target speed is always a constant at 90 km/h). The intuitive interpretation is if the model only tries to minimise emissions, the driver needs to frequently slow down in the first half of the journey but can drive at a higher speed (close to the maximum of 90 km/h) in most parts of the second half of the journey. This is particularly the case for the CSP and ASP policies. On the other hand, to only minimise fuel, the driver has to regularly slow down and speed up during the entire journey, and the speed curves are below the default maximum value. Although a similar tendency that the average speed at the first half of the journey is lower than that in the second half is seen, the contrast between the two halves is much less apparent compared to the emission-focused model. Another difference between the two models is in the fuel-focused model, it is the ASP policy (green) that gives the smallest average speed over the entire journey, while in the emission-focused mode, PSP (orange) presents the smallest average speed. Those significant differences between the two models under heavy traffic scenarios are perhaps due to the complicated environments and factors that can affect the speed calculations in the heavy traffic cases, such that the strong correlation between fuel and NOx can no longer lead to similar results between the two models as in the free traffic case. Any tiny perturbation in the process may result in a different outcome which may lead to an even more different result in a sequential manner, considering MPC is calculated from a sequence of optimisation iterations.

6.3 Future work

The model proposed in the previous section has certain limitations, particularly in how to link NOx emissions with other kinds of emissions solely based on their monetary values. Moreover, it is commonly accepted that combining Pareto-style multi-objective optimisation with MPC is unpractical and a simple combination of weighted sum is often used as a compromise (Bemporad et al 2009). In the future, a more accurate two-phase model that tries to keep a Pareto-style result while also take advantage of the accuracy from MPC will be considered. A brief outline of this two-phase model is presented here, and more details need to be further investigated in the next round of MODALES.

The two-phase model decomposes the entire solution process into two levels: a high-level deterministic free traffic optimal control/dynamic programming (DP) problem, and a low-level stochastic MPC problem.

6.3.1 Phase-1 (P1): High-level deterministic free-traffic optimal control problem

Solve a coarse Multi-objective Optimisation Problem (MOOP) problem (with fuel, emissions, etc) using traditional optimal control / dynamic programming methods considering historic average speed and route condition such as gradients (all deterministic). An example of such a global deterministic model minimising fuel can be found in Ozatay et al. (2014). For a specific problem with fixed objectives, this high-level model only needs to be solved for once such that traditional MOOP methods (weighted sum, epsilon-constraint) are applicable.

- Advantage: this gives a globally optimised solution with respect to most deterministic characteristics, such as route gradient, historic average speed, vehicle dynamics, physical constraints
- This global solution cannot be achieved by the previous MPC, whose solution is highly locally focussed.
- The speed profiles generate by Phase-1 provide high-quality “global model solutions” to be followed by Phase-2.

Output: A Pareto front with coarse solutions $p \in P$ (speed profiles) and their respective objective term weights $\boldsymbol{w}_p = \left(w_{p1}, w_{p2}, \dots, w_{pn}\right)^T, p \in P$.

Figure 6.6 gives an illustrative diagram summarising the above global traffic free deterministic model (Phase-1). First, deterministic input such as road grade, traffic signals, distances, historic average traffic speed and the necessary vehicle dynamic, safety and comfort constraints are provided to a free traffic scenario where no surrounding traffic is considered. Then, this free traffic problem will be solved by a dynamic programming model by discretising the route into distance intervals and allowed speeds into fixed values with an appropriate granularity. A globally optimal speed profile will thus be obtained by DP search where each step determines the transition from the current distance/speed combination to the next one. By applying MOOP to the DP model, a Pareto front can be found showing different trade-offs. Each point on the Pareto front corresponds to a complete speed profile.

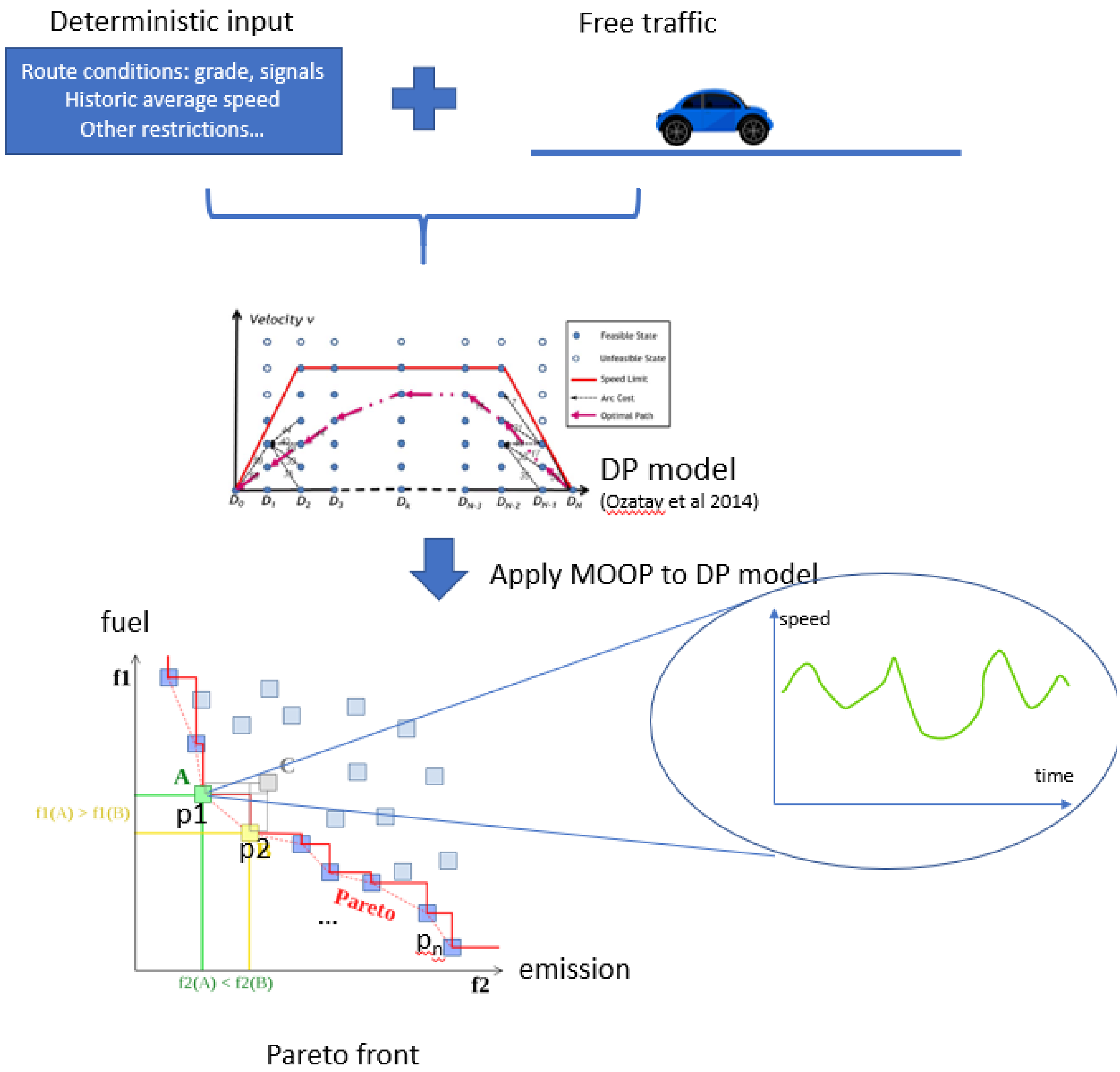

Figure 6.6: High-level Phase-1 model (global, deterministic and free traffic)

6.3.2 Phase 2 (P2): low-level stochastic MPC considering surrounding traffic predictions

For each point p (a speed profile associated with a weight vector $\mathbf{w}_p$) on the Pareto front from P1:

Solve an MPC (similar to Jia et al 2021) on p and $\mathbf{w}_p$ considering predicted real-time traffic conditions (average surrounding or predicted by some machine learning methods), where it

- Minimises fuel, emissions and other necessary objectives
- minimises deviation from Pareto front speed (try to keep some global optimality)
- minimises deviation the “desired” from real-time predictions (which can’t be realised in P1)
- considers safety requirements (which cannot be realised in P1)

- considers vehicle dynamics and physical constraints

Figure 6.7 gives an illustrative diagram summarising the low-level real-time MPC model (Phase-2), which takes the output Pareto points as its input and uses the MPC model to give refined final solutions. For each point in the Pareto front, a MPC model similar to the one proposed in Eq. (7-12) - (7-21) is formulated and solved to reflect real-time traffic conditions with surrounding traffics while also try to minimise the deviation between the real-time profile and the global optimal profile from Phase-1. Therefore, this final set of solutions both considers global optimality established under a Pareto-style MOOP and real-time stochastic requirements with surrounding traffics.

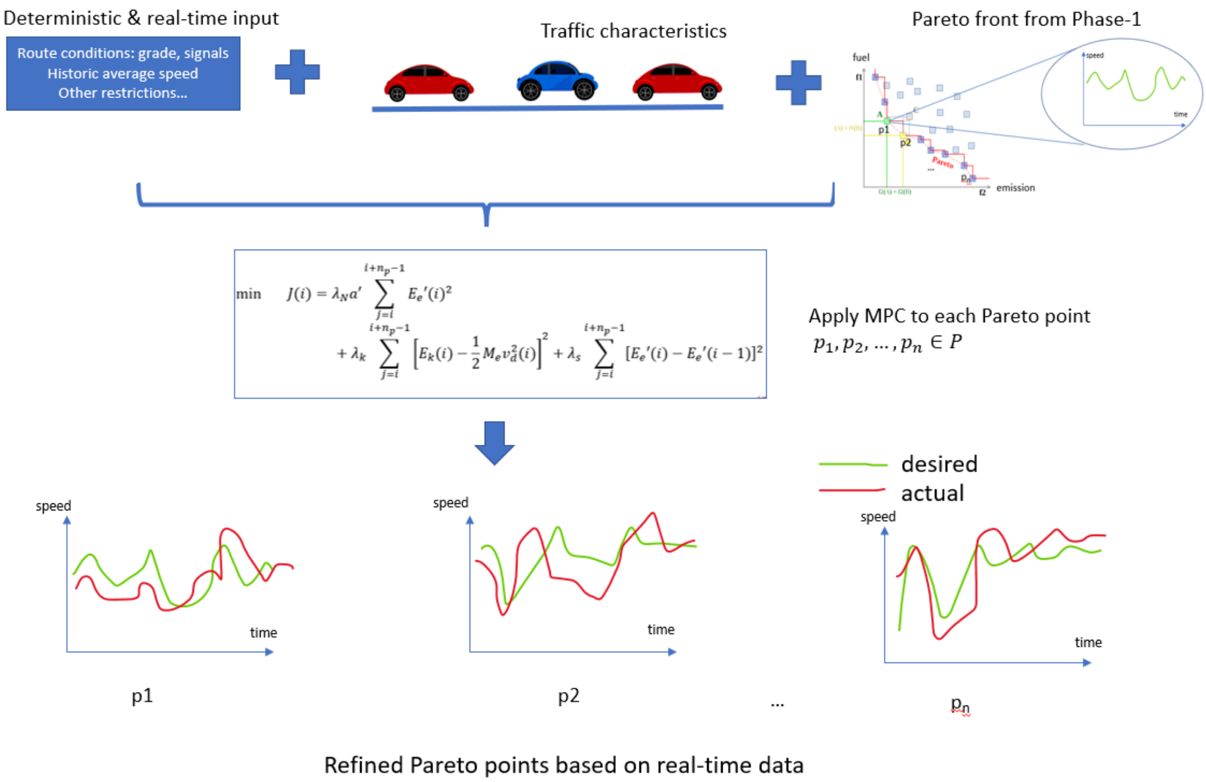

$$\min \quad J(i) = \lambda_N a' \sum_{j=i}^{i+n_p-1} E_e'(i)^2 + \lambda_k \sum_{j=i}^{i+n_p-1} \left[E_k(i) - \frac{1}{2} M_e v_d^2(i)\right]^2 + \lambda_s \sum_{j=i}^{i+n_p-1} [E_e'(i) - E_e'(i-1)]^2$$

Figure 6.7: Low-level Phase-2 model (local, real-time/stochastic and heavy traffic)

The specific algorithmic design of the above two-phase model will soon be carried out in the next round of research. In addition, more pollutants will be included in the new model(s), e.g. tyre ware mass and brake-related emissions.

6.4 Conclusions

In this chapter, a piece of closely relevant previous work in MPC optimal control models minimising fuel consumption is reviewed. Based on this work, a modified MPC model is proposed and tested where the fuel term in the objective is replaced with a new term minimising emissions including NOx, NH3, VOC and PM. This connection can be established because there is a simulated relation between power energy and NOx, as well as unified monetary values among all these pollutants. Experimental results of the new and original MPC approaches are compared. Finally, future research directions are discussed where a two-phase model is briefly outlined and to be further investigated in the future. This will be reported in MODALES D6.4 when the model is applied to the trail data to be collected in eight European cities plus City of Nanjing in China.

7 Rankings of driving behaviour Key Performance Indicators

In this chapter, the driving behaviour Key Performance Indicators (KPIs) related to powertrain emissions are ranked based on their importance; additionally, the driving tips are provided to drop the powertrain emissions from the viewpoint of driving behaviours.

7.1 Driving behaviour KPIs ranking of powertrain emissions

The KPIs ranking is based on the simulation results of GT-SUITE model. Given a specific change of the KPIs, corresponding changes in percentage of the emission factors can be calculated using the simulation results. The higher changes in the emission factors, the more important are the KPIs to the emissions. The KPIs are described in Table 7.1. Part of the KPIs in Table 7.1 such as "average acceleration", "average speed", "average speed without stops", "average deceleration", "% of time in acceleration", "% of distance in acceleration", "% of time in deceleration", and "% of distance in deceleration" were borrowed from the published work; the other KPIs were proposed by the authors based on the driving behaviour analysis.

Table 7.1: KPIs ranking based on the simulation results

Definition	KPIs for exhaust emissions	Unit	Ranking	Emission factor change (%) to KPIs change (%)	Driving tips
The proportions of acceleration >0.9 m/s^2 duration in the total travel time	Aggressiveness (% of time in the acceleration >0.9 m/s^2)	%	1	65.7%	Avoid aggressive acceleration durations if unnecessary
Average acceleration in the journey	Average acceleration	m/s^2	2	53.2%	Avoid aggressive acceleration if unnecessary
The proportions of speed interval of 20~50 km/h in the total travel time	% of time in speed interval of 20~50 km/h	%	3	20.3%	Try to drive in the speed interval of 20~50 km/h if possible
Average driving speed in the journey	Average speed	m/s	4	19.8%	Avoid aggressive acceleration if unnecessary
Average driving speed in the journey without the stop events	Average speed without stops	m/s	5	19.3%	Try to avoid the stop events if possible
The proportions of deceleration of -0.9~0 m/s^2 in the total travel time	% of time in the deceleration -0.9~0 m/s^2	%	6	14.2%	Try to increase the durations in acceleration range of --0.9~0 m/s^2
Average deceleration in the journey	Average deceleration	m/s^2	7	13.9%	Avoid aggressive deceleration if unnecessary

Definition	KPIs for exhaust emissions	Unit	Ranking	Emission factor change (%) to KPIs change (%)	Driving tips
The proportions of acceleration duration in the total travel time	% of time in acceleration	%	8	9.1%	Try to decrease the acceleration durations
The proportions of acceleration distance in the total travel distance	% of distance in acceleration	%	9	7.5%	Try to decrease the acceleration distance
The proportions of deceleration duration in the total travel time	% of time in deceleration	%	10	6.4%	Try to decrease the acceleration durations
The proportions of deceleration distance in the total travel distance	% of distance in deceleration	%	11	5.8%	Try to decrease the acceleration distance
The proportions of speed interval 50~70 km/h in the total travel distance	% of distance in speed interval 50~70 km/h	%	12	4.3%	Try to drive in the speed range of 50~70 km/h if possible
The driving speed when the gear is prepared to upshift	Gear upshift speed	m/s	13	1.3%	Try to use a proper high gear if possible
The driving speed when the gear is prepared to downshift	Gear downshift speed	m/s	14	0.9%	Try to use a proper high gear if possible

1: the most important; 14: the least important

7.2 Rankings of driving behaviour KPIs for brake wear emissions

The rankings of driving behaviour KPIs for brake wear emissions can be obtained, including the following steps:

- The brake wear emissions from our simulation result serve as the output variable.
- The driving behaviour KPIs for brake emissions set as the input variable.
- Obtain the output results by changing single input variable and leaving other input variables unchanged.
- Calculate the importance by dividing the % change in the output variable over the % change in the input variable.

The obtained results are listed in Table 7.2. From this table, it can be seen that deceleration rates of braking event have the most impact on the brake wear emissions, while average initial speed when braking presents the least influence on the brake wear emissions.

Table 7.2: Rankings of driving behaviour KPIs for brake wear emissions

Driving behaviour KPIs for brake emissions	Unit	Ranking (1: most important)	Ratio of output % change to input %
Deceleration rate of braking	$m\ s^{-2}$	1	1.83
Average deceleration rate when braking	$m\ s^{-2}$	2	1.67
Braking distance	m	3	1.47
Braking time	s	4	1.38
Initial speed when braking	km/h	5	0.96
Average initial speed when braking	km/h	6	0.79

7.3 Rankings of driving behaviour KPIs for tyre wear emissions

The rankings of driving behaviour KPIs for tyre wear emissions can be obtained, including the following steps:

- The tyre wear emissions from our simulation result serve as the output variable.
- The driving behaviour KPIs for tyre emissions set as the input variable.
- Obtain the output results by changing single input variable and leaving other input variables unchanged.
- Calculate the importance by dividing the % change in the output variable over the % change in the input variable.

Table 7.3 summarises the rankings of driving behaviour KPIs affecting the wear emissions of the ***left tyres*** studied in this work. It can be seen that *deceleration rate when vehicle right braking* presents the largest contribution for tyre wear, followed by *acceleration rate when vehicle right acceleration*, and *initial speed when right braking*. On the other hand, the least influence factor affecting tyre wear is *driving speed when vehicle left cruising*.

Table 7.3: Rankings of driving behaviour KPIs for left-tyre wear emissions

Driving behaviours KPIs for tyre emissions	Wear amount (m^3/rev)	Wear mass (g/rev)	Ranking	Ratio of output % change to input %
Deceleration rate when right braking	$5.43\ 10^{-10}$	$6.30\ 10^{-4}$	1	3.29
Acceleration rate when right accelerating	$4.13\ 10^{-10}$	$4.80\ 10^{-4}$	2	2.76
Initial speed when right braking	$3.14\ 10^{-10}$	$3.64\ 10^{-4}$	3	2.62
Initial speed when right accelerating	$2.82\ 10^{-10}$	$3.27\ 10^{-4}$	4	1.76
Deceleration rate when straight braking	$2.51\ 10^{-10}$	$2.91\ 10^{-4}$	5	1.35
Acceleration rate when straight accelerating	$1.78\ 10^{-10}$	$2.07\ 10^{-4}$	6	0.99

Driving behaviours KPIs for tyre emissions	Wear amount (m^3/rev)	Wear mass (g/rev)	Ranking	Ratio of output % change to input %
Initial speed when straight braking	$1.49\ 10^{-10}$	$1.73\ 10^{-4}$	7	0.68
Initial speed when right cruising	$1.27\ 10^{-10}$	$1.47\ 10^{-4}$	8	0.59
Initial speed when straight accelerating	$1.07\ 10^{-10}$	$1.24\ 10^{-4}$	9	0.50
Driving speed when straight cruising	$4.73\ 10^{-11}$	$5.49\ 10^{-5}$	10	0.46
Deceleration rate when left braking	$4.14\ 10^{-11}$	$4.80\ 10^{-5}$	11	0.39
Acceleration rate when left accelerating	$3.79\ 10^{-11}$	$4.40\ 10^{-5}$	12	0.37
Initial speed when left braking	$2.65\ 10^{-11}$	$3.07\ 10^{-5}$	13	0.32
Driving speed when left cruising	$2.59\ 10^{-11}$	$3.00\ 10^{-5}$	14	0.23

8 Conclusions

This deliverable reports the results produced by Task 3.5 in which a thorough investigation into the correlation between vehicle emissions and driving behaviour has been carried out, aimed at providing quantitative evidence and tools for the development of low-emission driving guidelines and practices. The models developed have used as much monitored data or measurements as possible from the previous tasks (i.e. 3.1, 3.2 and 3.3). They have produced a comparable and promising outcome with reference to the monitored data, as summarised below.

- The PEMS exhaust data is accurate and adequate (second by second) for instantaneous emission modelling, with a high level of agreement with the prediction of the models.
- Brake wear measurements collected in-lab are also accurate and reliable, and can be used to directly validate the results of the mathematical models as both have the same output frequency.
- Real-world wear measurements of the **left tyres** (i.e. on the left side of the vehicle) were collected every three months or so. As the actual corresponding driving behaviour data (e.g. acceleration, speed) can not be made available for analysis due to data privacy and business interest, the behaviour data are classified into bins/categories. Analysis shows that tyre wear measurements exhibit a high degree of asymmetry with outliers far away from the average value. Simply linear regression models fail to correlate average categorical accelerations (both longitudinal and lateral) and vehicle speed to tyre wear. More advanced non-linear models (e.g. the XGBoost non-linear fitting method) seem to be able to improve the correlation considerably, with a R square value of 0.846, due to their capability of capturing the skewness and peaked-ness of the tyre wear measurements.

To overcome the limitations on vehicle types, driver behaviours and many other factors such as road and traffic conditions in the measurement campaigns, a set of simulation tools and models have been developed. A GT-suite vehicle model is developed to simulate exhaust emissions. This "physical" model consists of engine performance map, gear number, gear ratio, and other vehicle parameters such as body dimensions and shape. The model is also able to take into account the effect road parameters, environment conditions on vehicle emissions and energy consumption. The results show that the vehicle model produces highly accurate emission estimations, and able to be used to simulate various driving behaviours and speed profiles. This enables the development of the mathematical model for exhaust emissions to be implemented in the MODALES user trails.

A Finite Element Analysis model has been developed to simulate the brake wear resulting from the contact behaviour on a microscope size scale. Calibrated and validated by the dyno bench tests carried out by the project partner BREMB, this "physical" model is able to produce brake wear for various brakes and under various driving conditions. The simulated results are then used to quantify the importance of Key Performance Indicators (KPIs) related to driving behaviour.

Similarly, a "physical" model was also developed for the simulation of the wear on the **left tyres**. The model is built in ABAQUS which provides a rich library of tyre and road surface parameters. This model is particularly useful given that real-world tyre wear is measured over a long interval (e.g. > 3 months) and the corresponding driving behaviour data is not available. Please note that the results reported later in this deliverable were based on the left tyres which take on more force than the right counterparts when the vehicle goes around right curves, especially sweeping turns. Likewise, the right tyres wear more than the left counterparts do when the vehicle goes around left curves.

Generally speaking, tyre wear is higher when driving on curves. So, it is important to reduce the vehicle speed to an appropriate level before entering a curve as lowering the speed when the vehicle is already on a curve may cause the car to skid. Driving advice could be something like:

"*Look for signs indicating curves and look ahead to identify the sharp turns ahead. Try to predict the length and approximate angle of the curve to know how to prepare yourself for a better and smoother manoeuvre*"[5].

A multi-objective optimisation methodology has been developed to simultaneously optimise several factors (e.g. driver's safety and comfort, fuel consumption as well as now low vehicle emissions from multiple sources). It is envisaged that the driver will be given consistent driving guidelines and recommendations to meet multiple criteria.

Finally, the modelling work is brought together by drawing a conclusion on the importance of behaviour-related Key Performance Indictors (KPIs). Quantitative results of the rankings of the behaviour-related KPIs have been produced, together with driving tips derived for the user trails later in the project.

8.1 Scientific publications

Whilst the results of Task 3.5 are described in this deliverable in detail, they are also presented in other formats of publication such as peer-reviewed scientific articles as listed in Table 8.1. These publications provide specific and thorough literature reviews, explanation of relevant studies and how the existing findings are used as well as where further work is needed.

Table 8.1: Publications led by the MODALES partners:

Title of Publication	Journal	DOI link or Status
Comparison of NOx and PN emissions between Euro 6 petrol and diesel passenger cars under real-world driving conditions	Science of The Total Environment	10.1016/j.scitotenv.2021.149789
Comparative analysis of non-exhaust airborne particles from electric and internal combustion engine vehicles	Journal of Hazardous Materials	10.1016/j.jhazmat.2021.126626
Driving behaviours analysis of truck drivers using motorway tests	IMechE, Part D: Journal of Automobile Engineering	10.1177/0954407020925568
Fuel economy and exhaust emissions of diesel vehicle under real traffic conditions	Energy Science & Engineering	10.1002/ese3.632
Analysis of significant contribution regions of NOx and PN emissions for passenger cars in the real-world driving	Environmental Science and Technology	Under review

It is also worthwhile mentioning that as a flagship project for international cooperation (InCo), MODALES has drawn great attention from international experts in various research fields such as engine technology, system control, and automotive engineering. Such collaboration enhances the

[5] https://driversed.com/driving-information/driving-conditions/driving-on-curves/

impact of the MODALES outcomes and helps explore the project's results. Some interesting topics for collaborative work are identified for example:

- *How do driving behaviour and traffic conditions affect the formation of air pollutants inside the engine?*
- *How will predictive cruise control be optimised for both fuel and emissions?*
- *How does low-emission driving (for non-exhaust emissions) help battery management of electric vehicles?*

Preliminary collaboration has so far led to several co-authored journal papers contributed by the MODALES partners in WP3 as shown in Table 8.2.

Table 8.2: Publications jointly contributed by the MODALES partners

Title of Publication	Journal	DOI link
Thermally induced variations in the nanostructure and reactivity of soot particles emitted from a diesel engine	Chemosphere	10.1016/j.chemosphere.2021.131712
Evaluation of the oxidative reactivity and electrical properties of soot particles	Carbon	10.1016/j.carbon.2021.02.086
An Enhanced Predictive Cruise Control System Design with Data-driven Traffic Prediction	IEEE-ITS	10.1109/TITS.2021.3076494
Driving Behavior Oriented Torque Demand Regulation for Electric Vehicles with Single Pedal Driving	Energy	10.1016/j.energy.2021.120568

9 References

Abaqus, Information about Abaqus available at: https://www.3ds.com/products-services/simulia/products/abaqus/.

Abaqus, Information of Abaqus ALE technique available at: http://abaqus.software.polimi.it/v6.14/books/usi/default.htm?startat=pt03ch14s06.html.

AbuBakar, A.R., Ouyang, H., 2008. Wear prediction of friction material and brake squeal using the finite element method. Wear 264(11), 1069-1076.

Afzal, A., Mujeebu, M.A., 2019. Thermo-mechanical and structural performances of automobile disc brakes: A review of numerical and experimental studies. Archives of Computational Methods in Engineering 26(5), 1489-1513.

Alam, M.S., McNabola, A., 2014. A critical review and assessment of Eco-Driving policy & technology: Benefits & limitations. Transp. Policy 35, 42-49.

Alemani, M., Nosko, O., Metinoz, I., Olofsson, U., 2016. A study on emission of airborne wear particles from car brake friction pairs. SAE International Journal of Materials and Manufacturing 9(1), 147-157.

Andrews, G.E., Ounzain, A.M., Li, H., Bell, M., Tate, J., Ropkins, K., 2007. The Use of a Water/Lube Oil Heat Exchanger and Enhanced Cooling Water Heating to Increase Water and Lube Oil Heating Rates in Passenger Cars for Reduced Fuel Consumption and CO2 Emissions During Cold Start. SAE Technical Paper.

Archard, J., 1953. Contact and rubbing of flat surfaces. Journal of applied physics 24(8), 981-988.

Awad, O.I., Ma, X., Kamil, M., Ali, O.M., Zhang, Z., Shuai, S., 2020. Particulate emissions from gasoline direct injection engines: A review of how current emission regulations are being met by automobile manufacturers. ScTEn 718, 137302.

Baek, S., Cho, J., Kim, K., Ahn, S., Myung, C.-L., Park, S., 2020. Effect of the Metal-Foam Gasoline Particulate Filter (GPF) on the Vehicle Performance in a Turbocharged Gasoline Direct Injection Vehicle over FTP-75. International Journal of Automotive Technology 21(5), 1139-1147.

Beatrice, C., Rispoli, N., di Blasio, G., Konstandopoulos, A. G., Papaioannou, E., & Imren, A., 2016. Impact of Emerging Engine and After-Treatment Technologies for Improved Fuel Efficiency and Emission Reduction for the Future Rail Diesel Engines. Emission Control Science and Technology, 2(2), 99–112.

Beddows, D.C.S., Harrison, R.M., 2021. PM10 and PM2.5 emission factors for non-exhaust particles from road vehicles: Dependence upon vehicle mass and implications for battery electric vehicles. Atmospheric Environment 244.

Beji, A., Deboudt, K., Khardi, S., Muresan, B., Lumière, L., 2020. Determinants of rear-of-wheel and tire-road wear particle emissions by light-duty vehicles using on-road and test track experiments. Atmospheric Pollution Research.

Bemporad, A., Munoz de la Pena, D., 2009. Multi-objective model predictive control. Automatica, vol. 45, pp. 2823–2830.

Bermúdez, V., Luján, J.M., Piqueras, P., Campos, D., 2014. Pollutants emission and particle behavior in a pre-turbo aftertreatment light-duty diesel engine. Energy 66, 509-522.

Böttcher, C.F., Müller, M., 2015. Drivers, practices and outcomes of low‐carbon operations: Approaches of German automotive suppliers to cutting carbon emissions. Business Strategy and the Environment 24(6), 477-498.

Cha, J., Lee, J., Chon, M.S., 2019. Evaluation of real driving emissions for Euro 6 light-duty diesel vehicles equipped with LNT and SCR on domestic sales in Korea. AtmEn 196, 133-142.

Chan, T.W., Saffaripour, M., Liu, F., Hendren, J., Thomson, K.A., Kubsh, J., Brezny, R., Rideout, G., 2016. Characterization of real-time particle emissions from a gasoline direct injection vehicle equipped with a catalyzed gasoline particulate filter during filter regeneration. Emission Control Science and Technology 2(2), 75-88.

Chasapidis, L., Grigoratos, T., Zygogianni, A., Tsakis, A., Konstandopoulos, A.G., 2018. Study of Brake Wear Particle Emissions of a Minivan on a Chassis Dynamometer. Emission Control Science and Technology 4(4), 271-278.

Chen, T., Guestrin, C., 2016. Xgboost: A scalable tree boosting system, Proceedings of the 22nd acm sigkdd international conference on knowledge discovery and data mining. pp. 785-794.

Cho, J., Ha, D., 2001. Averaging and finite-element discretization approaches in the numerical analysis of functionally graded materials. Materials Science and Engineering: A 302(2), 187-196.

Cho, J., Jung, B., 2007. Prediction of tread pattern wear by an explicit finite element model. Tire science and Technology 35(4), 276-299.

Cho, J., Shin, S., Yoo, W., 2005. Crown shape optimization for enhancing tire wear performance by ANN. Computers & Structures 83(12-13), 920-933.

Cho, J.R., Choi, J.H., Kim, Y.S., 2011. Abrasive wear amount estimate for 3D patterned tire utilizing frictional dynamic rolling analysis. Tribology International 44(7-8), 850-858.

Cho, J.R., Kim, K.W., Yoo, W.S., Hong, S.I., 2004. Mesh generation considering detailed tread blocks for reliable 3D tire analysis. Advances in Engineering Software 35(2), 105-113.

Cho, J.R., Shin, S.W., Yoo, W.S., 2005. Crown shape optimization for enhancing tire wear performance by ANN. Computers & Structures 83(12), 920-933.

Claffey, P.J., 1971. Running costs of motor vehicles as affected by road design and traffic. NCHRP Report(111).

Cristol-Bulthé, A.-L., Desplanques, Y., Degallaix, G., Berthier, Y., 2008. Mechanical and chemical investigation of the temperature influence on the tribological mechanisms occurring in OMC/cast iron friction contact. Wear 264(9-10), 815-825.

Di Blasio, G., Belgiorno, G., Beatrice, C., 2017. Effects on performances, emissions and particle size distributions of a dual fuel (methane-diesel) light-duty engine varying the compression ratio. ApEn 204, 726-740.

Dimaratos, A., Toumasatos, Z., Doulgeris, S., Triantafyllopoulos, G., Kontses, A., Samaras, Z., 2019. Assessment of CO2 and NOx emissions of one diesel and one bi-fuel gasoline/CNG Euro 6 vehicles during real-world driving and laboratory testing. Frontiers in Mechanical Engineering 5, 62.

Duarte, G., Gonçalves, G., Farias, T., 2016. Analysis of fuel consumption and pollutant emissions of regulated and alternative driving cycles based on real-world measurements. Transportation Research Part D: Transport and Environment 44, 43-54.

EEA, 2019a. Air Quality in Europe - 2019 Report. European Environment Agency.

Eriksson, M., Lord, J., Jacobson, S., 2001. Wear and contact conditions of brake pads: dynamical in situ studies of pad on glass. Wear 249(3-4), 272-278.

Fan, H., 2017. A Critical Review and Analysis of Construction Equipment Emission Factors. Procedia Engineering, 196, 351–358. https://doi.org/10.1016/j.proeng.2017.07.210

Forouzanfar, M.H., Afshin, A., Alexander, L.T., Anderson, H.R., Bhutta, Z.A., Biryukov, S., Brauer, M., Burnett, R., Cercy, K., Charlson, F.J., 2016. Global, regional, and national comparative risk assessment of 79 behavioural, environmental and occupational, and metabolic risks or clusters of risks, 1990–2015: a systematic analysis for the Global Burden of Disease Study 2015. The lancet 388(10053), 1659-1724.

Gao, J., Chen, H., Li, Y., Chen, J., Zhang, Y., Dave, K., Huang, Y., 2019a. Fuel consumption and exhaust emissions of diesel vehicles in worldwide harmonized light vehicles test cycles and their sensitivities to eco-driving factors. Energy Conversion & Management 196, 605-613.

Gao, J., Chen, H., Liu, Y., Ying, L., Li, T., Tu, R., Liang, B., Ma, C., 2021. The effect of after-treatment techniques on the correlations between driving behaviours and NOx emissions of a passenger cars. Journal of Cleaner Production 288, 125647.

Gao, J., Tian, G., Sorniotti, A., 2019b. On the emission reduction through the application of an electrically heated catalyst to a diesel vehicle. Energy Science & Engineering 7(6), 2383-2397.

Gao, J., Tian, G., Sorniotti, A., Karci, A.E., Di Palo, R., 2019c. Review of thermal management of catalytic converters to decrease engine emissions during cold start and warm up. Appl. Therm. Eng. 147, 177-187.

Garg, B.D., Cadle, S.H., Mulawa, P.A., Groblicki, P.J., Laroo, C., Parr, G.A., 2000. Brake wear particulate matter emissions. Environmental Science & Technology 34(21), 4463-4469.

Giakoumis, E.G., Zachiotis, A.T., 2017. Investigation of a diesel-engined vehicle’s performance and emissions during the WLTC driving cycle—comparison with the NEDC. Energies 10(2), 240.

Giechaskiel, B., Joshi, A., Ntziachristos, L., Dilara, P., 2019. European regulatory framework and particulate matter emissions of gasoline light-duty vehicles: A review. Catalysts 9(7), 586.

Goo, B.-C., 2018. A study on the contact pressure and thermo-elastic behavior of a brake disc-pad by infrared images and finite element analysis. Applied Sciences 8(9), 1639.

Grigoratos, T., Gustafsson, M., Eriksson, O., Martini, G., 2018. Experimental investigation of tread wear and particle emission from tyres with different treadwear marking. Atmospheric environment 182, 200-212.

Grigoratos, T., Martini, G., 2015. Brake wear particle emissions: a review. Environmental Science and Pollution Research 22(4), 2491-2504.

Guo, X., Wu, H., Chen, D., Ye, Z., Shen, Y., Liu, J., & Cheng, S., 2020. Estimation and prediction of pollutant emissions from agricultural and construction diesel machinery in the Beijing-Tianjin-Hebei (BTH) region, China. Environmental Pollution, 260, 113973. https://doi.org/10.1016/j.envpol.2020.113973.

Han, M.J., Lee, C.H., Park, T.W., Park, J.M., Son, S.M., 2017. Coupled thermo-mechanical analysis and shape optimization for reducing uneven wear of brake pads. International Journal of Automotive Technology 18(6), 1027-1035.

Hasan, M.A., Frame, D.J., Chapman, R., Archie, K.M., 2019. Emissions from the road transport sector of New Zealand: Key drivers and challenges. Environmental Science and Pollution Research 26(23), 23937-23957.

Hays, M.D., Preston, W., George, B.J., George, I.J., Snow, R., Faircloth, J., Long, T., Baldauf, R.W., McDonald, J., 2017. Temperature and driving cycle significantly affect carbonaceous gas and particle matter emissions from diesel trucks. Energy Fuels 31(10), 11034-11042.

Hoepfner, A., Roduner, C.A., 2013. PM sensor based on-board diagnosis of particulate filter efficiency. SAE Technical Paper.

Hooftman, N., Messagie, M., Van Mierlo, J., Coosemans, T., 2018. A review of the European passenger car regulations–Real driving emissions vs local air quality. Renewable Sustainable Energy Reviews 86, 1-21.

Huang, Y., Surawski, N.C., Organ, B., Zhou, J.L., Tang, O.H., Chan, E.F., 2019. Fuel consumption and emissions performance under real driving: Comparison between hybrid and conventional vehicles. ScTEn 659, 275-282.

Hussein, T., Johansson, C., Karlsson, H., Hansson, H.-C., 2008. Factors affecting non-tailpipe aerosol particle emissions from paved roads: On-road measurements in Stockholm, Sweden. Atmospheric Environment 42(4), 688-702.

Jang, J., Lee, J., Choi, Y., Park, S., 2018. Reduction of particle emissions from gasoline vehicles with direct fuel injection systems using a gasoline particulate filter. ScTEn 644, 1418-1428.

Jia, D., Chen, H., Zuduo Zheng, Z., Watling, D., Connors R., Gao, J., Li, Y., 2021. An Enhanced Predictive Cruise Control System Design With Data-Driven Traffic Prediction. IEEE Transactions on Intelligent Transportation Systems, doi: 10.1109/TITS.2021.3076494.

Kakad, S.R., More, R.M., Kamble, D.N., 2017. Mathematical Modeling & Analysis of Brake Pad for Wear Characteristics. Impact and Innovation in Mechanical Engineering 5(6), 1048-1056.

Kamal, M.A.S., Mukai, M., Murata, J., Kawabe, T., 2010. On board eco-driving system for varying road-traffic environments using model predictive control, 2010 IEEE International Conference on Control Applications. IEEE, pp. 1636-1641.

Kim, G., Lee, S., 2018. Characteristics of Tire Wear Particles Generated by a Tire Simulator under Various Driving Conditions. Environ Sci Technol 52(21), 12153-12161.

Knisley, S., 2002. A correlation between rolling tire contact friction energy and indoor tread wear. Tire science and Technology 30(2), 83-99.

Ko, J., Myung, C.-L., Park, S., 2019. Impacts of ambient temperature, DPF regeneration, and traffic congestion on NOx emissions from a Euro 6-compliant diesel vehicle equipped with an LNT under real-world driving conditions. AtmEn 200, 1-14.

Koishi, M., Shida, Z., 2006. Multi-objective design problem of tire wear and visualization of its Pareto solutions. Tire Science and Technology 34(3), 170-194.

Kontses, A., Triantafyllopoulos, G., Ntziachristos, L., Samaras, Z., 2020. Particle number (PN) emissions from gasoline, diesel, LPG, CNG and hybrid-electric light-duty vehicles under real-world driving conditions. AtmEn 222, 117126.

Kreider, M.L., Panko, J.M., McAtee, B.L., Sweet, L.I., Finley, B.L., 2010. Physical and chemical characterization of tire-related particles: Comparison of particles generated using different methodologies. Science of The Total Environment 408(3), 652-659.

Kukutschová, J., Moravec, P., Tomášek, V., Matějka, V., Smolík, J., Schwarz, J., Seidlerová, J., Šafářová, K., Filip, P., 2011. On airborne nano/micro-sized wear particles released from low-metallic automotive brakes. Environmental Pollution 159(4), 998-1006.

Kwak, J.-h., Kim, H., Lee, J., Lee, S., 2013. Characterization of non-exhaust coarse and fine particles from on-road driving and laboratory measurements. Science of the Total Environment 458, 273-282.

Le Maitre, O., Süssner, M., Zarak, C., 1998. Evaluation of tire wear performance. SAE Technical Paper.

Lee, H., Ju, M., Kim, Y., 2020. Estimation of emission of tire wear particles (TWPs) in Korea. Waste Manag 108, 154-159.

Lee, S., Kwak, J., Kim, H., Lee, J., 2013. Properties of roadway particles from interaction between the tire and road pavement. International Journal of Automotive Technology 14(1), 163-173.

Li, M., Chen, X., Wang, J., Xu, Y., 2013. Study on the PM2. 5 and ultra fine PM characteristics of diesel vehicle with DPF under the different driving conditions, Proceedings of the FISITA 2012 World Automotive Congress. Springer, pp. 779-788.

Lin, Q., Tay, K.L., Yu, W., Yang, W., Wang, Z., 2021. Effects of polyoxymethylene dimethyl ether 3 (PODE3) addition and injection pressure on combustion performance and particle size distributions in a diesel engine. Fuel 283, 119347.

Liu, Y., Chen, H., Gao, J., Li, Y., Dave, K., Chen, J., Federici, M., Perricone, G., 2021. Comparative analysis of non-exhaust airborne particles from electric and internal combustion engine vehicles. Journal of Hazardous Materials 420, 126626.

Liu, Z.G., Berg, D.R., Vasys, V.N., Dettmann, M.E., Zielinska, B., Schauer, J.J., 2010. Analysis of C1, C2, and C10 through C33 particle-phase and semi-volatile organic compound emissions from heavy-duty diesel engines. AtmEn 44(8), 1108-1115.

Luján, J.M., Bermúdez, V., Dolz, V., Monsalve-Serrano, J., 2018. An assessment of the real-world driving gaseous emissions from a Euro 6 light-duty diesel vehicle using a portable emissions measurement system (PEMS). AtmEn 174, 112-121.

Lupker, H., Cheli, F., Braghin, F., Gelosa, E., Keckman, A., 2004. Numerical Prediction of Car Tire Wear. Tire science and technology 32, 164-186.

Ma, H., Xie, H., Huang, D., Xiong, S., 2015. Effects of driving style on the fuel consumption of city buses under different road conditions and vehicle masses. Transportation Research Part D: Transport Environment 41, 205-216.

Mamakos, A., Arndt, M., Hesse, D., Augsburg, K., 2019. Physical Characterization of Brake-Wear Particles in a PM10 Dilution Tunnel. Atmosphere 10(11).

Manual, A.U.s., 2002. Version 6.3. 1, Hibbitt, Karlson and Sorensen. Inc., USA.

Mathissen, M., Evans, C., 2019. Lowbrasys brake wear cycle-3h LACT. Mendeley Data 1.

Mathissen, M., Grigoratos, T., Lahde, T., Vogt, R., 2019. Brake Wear Particle Emissions of a Passenger Car Measured on a Chassis Dynamometer. Atmosphere 10(9).

Mathissen, M., Grochowicz, J., Schmidt, C., Vogt, R., zum Hagen, F.H.F., Grabiec, T., Steven, H., Grigoratos, T., 2018. A novel real-world braking cycle for studying brake wear particle emissions. Wear 414, 219-226.

Mathissen, M., Scheer, V., Vogt, R., Benter, T., 2011. Investigation on the potential generation of ultrafine particles from the tire–road interface. Atmospheric Environment 45(34), 6172-6179.

McCaffery, C., Zhu, H., Li, C., Durbin, T.D., Johnson, K.C., Jung, H., Brezny, R., Geller, M., Karavalakis, G., 2020. On-road gaseous and particulate emissions from GDI vehicles with and without gasoline particulate filters (GPFs) using portable emissions measurement systems (PEMS). ScTEn 710, 136366.

Meloni, E., Palma, V., 2020. Most Recent Advances in Diesel Engine Catalytic Soot Abatement: Structured Catalysts and Alternative Approaches. Catalysts 10(7), 745.

Mendoza-Villafuerte, P., Suarez-Bertoa, R., Giechaskiel, B., Riccobono, F., Bulgheroni, C., Astorga, C., Perujo, A., 2017. NOx, NH3, N2O and PN real driving emissions from a Euro VI heavy-duty vehicle. Impact of regulatory on-road test conditions on emissions. ScTEn 609, 546-555.

Mera, Z., Fonseca, N., López, J.-M., Casanova, J., 2019. Analysis of the high instantaneous NOx emissions from Euro 6 diesel passenger cars under real driving conditions. ApEn 242, 1074-1089.

Merkisz, J., Bielaczyc, P., Pielecha, J., Woodburn, J., 2019. RDE testing of passenger cars: The effect of the cold start on the emissions results. SAE Technical Paper.

Myung, C.-L., Choi, K., Cho, J., Kim, K., Baek, S., Lim, Y., Park, S., 2020. Evaluation of regulated, particulate, and BTEX emissions inventories from a gasoline direct injection passenger car with various ethanol blended fuels under urban and rural driving cycles in Korea. Fuel 262, 116406.

Mitchell, R., Frank, E., 2017. Accelerating the XGBoost algorithm using GPU computing. PeerJ Computer Science 3, e127.

Muro, T., 1989. Wear rate characteristics of heavy dump truck tyres. Journal of Terramechanics 26(1), 11-23.

NAEI, 2018. Road transport emission factor from NAEI 2018. https://naei.beis.gov.uk/data/ef-transport.

Niemann, H., Winner, H., Asbach, C., Kaminski, H., Frentz, G., Milczarek, R., 2020. Influence of disc temperature on ultrafine, fine, and coarse particle emissions of passenger car disc brakes with organic and inorganic pad binder materials. Atmosphere 11(10), 1060.

Ntziachristos, L., Samaras, Z., 2000. Speed-dependent representative emission factors for catalyst passenger cars and influencing parameters. AtmEn 34(27), 4611-4619.

O'Driscoll, R., Stettler, M.E., Molden, N., Oxley, T., ApSimon, H.M., 2018. Real world CO 2 and NO x emissions from 149 Euro 5 and 6 diesel, gasoline and hybrid passenger cars. ScTEn 621, 282-290.

Ouyang, H., 2008. Wear prediction of friction material and brake squeal using the finite element method. Wear 264(11-12), 1069-1076.

Ozatay, E., et al., 2014. Cloud-Based Velocity Profile Optimization for Everyday Driving: A Dynamic-Programming-Based Solution. IEEE Transactions on Intelligent Transportation Systems, vol. 15, no. 6, pp. 2491-2505. doi: 10.1109/TITS.2014.2319812.

Pan, B., 2018. Application of XGBoost algorithm in hourly PM2. 5 concentration prediction, IOP conference series: Earth and environmental science. IOP publishing, p. 012127.

Perricone, G., Wahlström, J., Olofsson, U., 2016. Towards a test stand for standardized measurements of the brake emissions. Proceedings of the Institution of Mechanical Engineers, Part D: Journal of Automobile Engineering 230(11), 1521-1528.

Reijnders, J., Boot, M., de Goey, P., 2018. Particle nucleation-accumulation mode trade-off: A second diesel dilemma? JAerS 124, 95-111.

Riva, G., Valota, G., Perricone, G., Wahlström, J., 2019. An FEA approach to simulate disc brake wear and airborne particle emissions. Tribology International 138, 90-98.

Riva, G., Wahlström, J., Alemani, M., Olofsson, U., 2017. A CFD study of a pin-on-disc tribometer setup focusing on airborne particle sampling efficiency, ECOTRIB 2017, 6th European COnference on TRIBology 7–9 June 2017, Ljubljana, Slovenia.

Rutty, M., Matthews, L., Andrey, J., Del Matto, T., 2013. Eco-driver training within the City of Calgary’s municipal fleet: Monitoring the impact. Transportation research part D: transport environment 24, 44-51.

Schmidt, A.A., Schmidt, T., Grabherr, O., Bartel, D., 2018. Transient wear simulation based on three-dimensional finite element analysis for a dry running tilted shaft-bushing bearing. Wear 408, 171-179.

SCIENTIFIC, I., 2013. AIR POLLUTION AND CANCER.

Söderberg, A., Sellgren, U., Andersson, S., 2008. Using Finite Element Analysis to Predict the Brake Pressure Needed for Effective Rotor Cleaning in Disc Brakes. SAE Int 2008-01-2565.

Stalnaker, D., Turner, J., 2002. Vehicle and course characterization process for indoor tire wear simulation. Tire Science and Technology 30(2), 100-121.

Suarez-Bertoa, R., Valverde, V., Clairotte, M., Pavlovic, J., Giechaskiel, B., Franco, V., Kregar, Z., Astorga, C., 2019. On-road emissions of passenger cars beyond the boundary conditions of the real-driving emissions test. Environ. Res. 176, 108572.

Sun, Y., Guo, Y., Zhai, W., 2019. Prediction of rail non-uniform wear–Influence of track random irregularity. Wear 420, 235-244.

Theicct.org, 2021. https://theicct.org/sites/default/files/publications/review-china-diesel-jun2021.pdf

Timmers, V.R.J.H., Achten, P.A.J., 2016. Non-exhaust PM emissions from electric vehicles. Atmospheric Environment 134, 10-17.

Tirovic, M., Day, A., 1991. Disc brake interface pressure distributions. Proceedings of the Institution of Mechanical Engineers, Part D: Journal of Automobile Engineering 205(2), 137-146.

Triantafyllopoulos, G., Dimaratos, A., Ntziachristos, L., Bernard, Y., Dornoff, J., Samaras, Z., 2019. A study on the CO2 and NOx emissions performance of Euro 6 diesel vehicles under various chassis dynamometer and on-road conditions including latest regulatory provisions. ScTEn 666, 337-346.

Tutuianu, M., Bonnel, P., Ciuffo, B., Haniu, T., Ichikawa, N., Marotta, A., Pavlovic, J., Steven, H.J.T.r.p.D.t., environment, 2015. Development of the World-wide harmonized Light duty Test Cycle (WLTC) and a possible pathway for its introduction in the European legislation. Transportation research part D: transport environment 40, 61-75.

Valota, G., De Luca, S., Söderberg, A., 2017. Using a finite element analysis to simulate the wear in disc brakes during a dyno bench test cycle. Proceedings of the Eurobrake, Dresden, Germany, 2-4.

Valverde, V., Mora, B.A., Clairotte, M., Pavlovic, J., Suarez-Bertoa, R., Giechaskiel, B., Astorga-LLorens, C., Fontaras, G., 2019. Emission Factors Derived from 13 Euro 6b Light-Duty Vehicles Based on Laboratory and On-Road Measurements. Atmos 10(5), 243.

Virkar, D., Thombare, D., 2013. Parametric Study And Experimental Evaluation Of Vehicle Tire Performance. International Journal of Mechanical Engineering and Robotics Research 2(2), 221-231.

Vojtisek-Lom, M., Vaculik, M., Pechout, M., Hopan, F., Arul Raj, A.F., Penumarti, S., Horak, J.S., Popovicheva, O., Ondracek, J., Dousova, B., 2021. Effects of braking conditions on nanoparticle emissions from passenger car friction brakes. Sci Total Environ 788, 147779.

Wahlström, J., 2015. A comparison of measured and simulated friction, wear, and particle emission of disc brakes. Tribology International 92, 503-511.

Wahlström, J., Matejka, V., Lyu, Y., Söderberg, A., 2017. Contact Pressure and Sliding Velocity Maps of the Friction, Wear and Emission from a Low-Metallic/Cast-Iron Disc Brake Contact Pair. Tribology in Industry 39(4), 460-470.

Wahlström, J., Matějka, V., Lyu, Y., Söderberg, A., 2017. Contact Pressure and Sliding Velocity Maps of the Friction, Wear and Emission from a Low-Metallic/Cast-Iron Disc Brake Contact Pair. Tribology in Industry 39(4).

Wahlström, J., Söderberg, A., Olofsson, U., 2009. Simulation of airborne wear particles from disc brakes. SAE Technical Paper.

Wang, H., Ge, Y., Hao, L., Xu, X., Tan, J., Li, J., Wu, L., Yang, J., Yang, D., Peng, J., 2018. The real driving emission characteristics of light-duty diesel vehicle at various altitudes. AtmEn 191, 126-131.

Wang, S., Zhu, X., Somers, L., de Goey, L., 2017. Effects of exhaust gas recirculation at various loads on diesel engine performance and exhaust particle size distribution using four blends with a research octane number of 70 and diesel. Energy Convers. Manage. 149, 918-927.

Weber, C., Sundvor, I., Figenbaum, E., 2019. Comparison of regulated emission factors of Euro 6 LDV in Nordic temperatures and cold start conditions: Diesel-and gasoline direct-injection. AtmEn 206, 208-217.

Wihersaari, H., Pirjola, L., Karjalainen, P., Saukko, E., Kuuluvainen, H., Kulmala, K., Keskinen, J., Rönkkö, T., 2020. Particulate emissions of a modern diesel passenger car under laboratory and real-world transient driving conditions. Environ. Pollut. 265, 114948.

Will, F., Boretti, A.J.S.i.j.o.e., 2011. A new method to warm up lubricating oil to improve the fuel efficiency during cold start. 4(1), 175-187.

Williams, A., Evans, M., 1983. Influence of tread wear irregularity on wet friction performance of tires, Frictional Interaction of Tire and Pavement. ASTM International.

Woo, S.-H., Kim, Y., Lee, S., Choi, Y., Lee, S., 2021. Characteristics of brake wear particle (BWP) emissions under various test driving cycles. Wear 480-481.

Xu, W., 2014. The study of tire wear properties base on FEM. South China University of Technology, Master Dissertation.

Yang, J., Roth, P., Durbin, T.D., Johnson, K.C., Cocker III, D.R., Asa-Awuku, A., Brezny, R., Geller, M., Karavalakis, G., 2018. Gasoline particulate filters as an effective tool to reduce particulate and polycyclic aromatic hydrocarbon emissions from gasoline direct injection (GDI) vehicles: a case study with two GDI vehicles. Environ. Sci. Technol. 52(5), 3275-3284.

Yang, Z., Ge, Y., Thomas, D., Wang, X., Su, S., Li, H., He, H., 2019. Real driving particle number (PN) emissions from China-6 compliant PFI and GDI hybrid electrical vehicles. AtmEn 199, 70-79.

Yinhui, W., Rong, Z., Yanhong, Q., Jianfei, P., Mengren, L., Jianrong, L., Yusheng, W., Min, H., Shijin, S., 2016. The impact of fuel compositions on the particulate emissions of direct injection gasoline engine. Fuel 166, 543-552.

Young, L.H., Liou, Y.J., Cheng, M.T., Lu, J.H., Yang, H.H., Tsai, Y.I., Wang, L.C., Chen, C.B., Lai, J.S., 2012. Effects of biodiesel, engine load and diesel particulate filter on nonvolatile particle number size distributions in heavy-duty diesel engine exhaust. J. Hazard. Mater. 199(2), 282-289.

Zheng, D., 2003. Prediction of tire tread wear with FEM steady state rolling contact simulation. Tire Science and Technology 31(3), 189-202.

Zum Hagen, F.H.F., Mathissen, M., Grabiec, T., Hennicke, T., Rettig, M., Grochowicz, J., Vogt, R., Benter, T., 2019. Study of brake wear particle emissions: impact of braking and cruising conditions. Environmental science & technology 53(9), 5143-5150.

For more information:

MODALES Project Coordinator

ERTICO - ITS Europe

Avenue Louise 326

1050 Brussels, Belgium

info@modales-project.eu
www.modales-project.eu

Adapting driver behaviour
for lower emissions